Processing and Characterization of Sustainable Polymers: Recycling, Renewable Resources, and Reduction

By

Yottha Srithep

A dissertation submitted in partial fulfillment of
the requirements for the degree of

Doctor of Philosophy
(Mechanical Engineering)

at the

UNIVERSITY OF WISCONSIN-MADISON

2012

Date of final oral examination: 11/27/12

The dissertation is approved by the following members of the Final Oral Committee:

Dr. Lih-Sheng Turng, Professor, Mechanical Engineering
Dr. Craig Clemons, Adjunct Professor, Mechanical Engineering
Dr. Xiaochun Li, Professor, Material Science Program
Dr. Tim Osswald, Professor, Mechanical Engineering
Dr. Robert Rowlands, Professor, Mechanical Engineering

ACKNOWLEDGEMENTS

This dissertation is a milestone in my journey toward obtaining my Ph.D. I feel grateful not to travel alone on this journey, but to have the compassion and well wishes of numerous people. This journey would never have reached its final destination without the assistance and support of the kind people around me, only some of whom it is possible to mention here.

First and foremost, I must forever acknowledge and thank Prof. Lih-Sheng Turng who has been my advisor, mentor, and a source of inspiration and support throughout my years of graduate study. I could never have accomplished this without his patience, encouragement, and guidance. I would also like to thank the members of the USDA Forest Products Laboratory, specifically Prof. Craig Clemons for his assistance and support throughout my research and Dr. Ronald Sabo for contributing his time to give valuable input into my research, and for them allowing me to use their laboratory facilities. I would also like to thank my dissertation committee, including Professors Tim Osswald, Robert Rowlands, and Xiaochun Li, for providing their time and valuable suggestions. Additionally, I want to express my gratitude toward the USDA's National Institute of Food and Agriculture Award (No. 2011-67009-20056) and the Thai Ministry of Science for contributing the financial support for my study and research.

I would like to acknowledge Dr. Srikanth Pilla, Dr. Jungjoo Lee, Tom Ellingham, Jun Peng, Hiaoyang Mi, and my friends and colleagues at the Polymer Engineering Center (PEC) for their support, comments, and constructive discussions. Special thanks go to Chris Lacey in editing my publications and dissertation throughout these years.

Last but not least, I would like to thank my parents, my sister, and Dr. Suntaree Watcharadamrongkun for their continuous support, understanding, and patience during the course of my study.

I dedicate this dissertation to
My parents for their constant support and unconditional love.

TABLE OF CONTENTS

Page

LIST OF TABLES

Page

LIST OF FIGURES

Page

ABSTRACT

This Ph.D. study aims to advance the understanding and know-how of sustainable polymers and composites to reduce their environmental impact and enhance their utilization. This can be done through recycling post-consumer plastics, using biodegradable polymers made from renewable resources, and reducing material usage in final products through foaming or stronger polymer composites. To evaluate the performance of these polymers and composites, the mechanical, thermal, rheological, morphological properties, and other relevant properties have been characterized.

The first chapter deals with recycling poly(ethylene terephthalate) (RPET), a commonly used material for beverage bottles. Melt-compounding and injection molding of RPET with various additives were performed. The addition of chain extenders greatly enhanced the moldability and mechanical properties of RPET. While the RPET and thermoplastic elastomer blends showed improved mechanical properties, the improvement was less significant and the blends were often immiscible due to the difference in polarities between the RPET and the thermoplastic elastomer.

Replacing non-biodegradable polymers with renewable/biodegradable polymers, e.g., poly(lactic acid) (PLA), was studied and reported in the second chapter. The injection molded PLA, after annealing treatment, offered several benefits such as a higher glass transition temperature, better heat resistance, and greater storage modulus and tensile strength. This study pointed to a new post-molding treatment that could enhance the heat resistance, which is one of

the major weaknesses of PLA components. The degree of crystallinity after long annealing times resembled those observed at higher temperatures, suggesting a time–temperature superposition relationship.

The study reported in chapters three and four reduced material usage by developing polymer composites or employing foaming. Nanofibrillated cellulose (NFC) from newable resources was used as a filler in both hydrophilic polymer polyvinyl alcohol (PVOH), and hydrophobic polymer poly(3-hydroxybutyrate-co-3-hydroxyvalerate, PHBV). An NFC fiber suspension was stirred with PVOH in water, followed by casting. PHBV powders were mixed with an NFC fiber suspension in water, freeze-dried, and melt compounded. NFC had a reinforcing effect and served as a nucleating agent but led to greater thermal degradation for both polymers. The addition of NFC yielded finer foamed morphologies in PVOH films but inhibited foaming in PHBV.

CHAPTER 1

Processing and Characterization of Recycled Poly(ethylene terephthalate) (PET) Blends with Chain Extenders (CE), Thermoplastic Elastomer (TPE), and/or Poly(butylene adipate-co-terephthalate) (PBAT)

1.1 Introduction

Poly (ethylene terephthalate) (PET) is one of the most widely used thermoplastic polyesters. PET is extensively used in various applications, such as beverage bottles, fibers, moldings, and sheets due to its superior chemical, physical, mechanical, and (oxygen and carbon dioxide) barrier properties. The largest application of PET in the U.S. is the manufacturing of bottles [1], which has grown approximately 9% annually, from 1995 to 2007 [2]. Most of these beverage bottles are disposable, which inevitably raises environmental concerns over their waste. Thus, to lessen the environmental hazards and burdens created by disposing of PET in landfills, much of the post-consumer PET is recycled to be reused in certain applications. However, recycled PET (RPET) undergoes hydrolytic and thermal degradations which lead to a reduction in the molecular weight and intrinsic viscosity that, in turn, deteriorates the mechanical properties and moldability of the recycled material [3-8]. Hydrolytic reactions, which are caused by retained moisture and contaminants, result in chain scission with carboxylic acid and hydroxyl ester end groups (cf. Figure 1.1 (a)), whereas the thermal cleavage of the PET ester bond leads to the formation of carboxylic end groups and vinyl esters (cf. Figure 1.1(b)) [9].

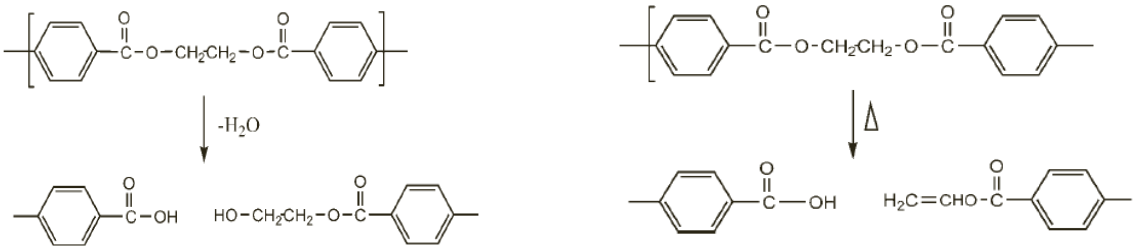

(a) (b)

Figure 1.1 (a) Hydrolytic and (b) thermal degradation reactions of PET.

The property deterioration of RPET may be compensated for by the addition of reinforcing fillers and toughening modifiers. For example, PET has been blended or compounded with several polymers, fillers, and nanoparticles to modify its physical properties. The addition of a second component to improve mechanical performance has been reported [10-13].

PET has also been blended with various elastomers such as ethylene propylene rubber (EPR), ethylene propylene diene monomer rubber (EPDM), nitrile butadiene rubber (NBR), and styrene-butadiene rubber (SBR) [14-21]. Due to the difference in their polarities, these blends are often immiscible resulting in unfavorable mechanical properties. On the other hand, adding certain chain extenders (CE) is an effective way to increase the molecular weight (and thus melt viscosity) of PET. Generally, chain extenders are low-molecular-weight, multifunctional compounds capable of a rapid reaction with the polymer end groups, leading to the coupling of macromolecules. Various organic substances, such as diepoxides, diisocyanates, dianhydrides, carbodiimides, and bisoxazolines, have been used to extend PET chains [8, 9, 22]. Combining RPET with other polymers, such as PBAT, can also improve properties such as toughness. This study investigates the effects of adding CE (chain extenders), TPE (thermoplastic elastomer), and

PBAT (poly(butylene adipate-co-terephthalate)), on the mechanical, morphological, rheological, and thermal properties of RPET. Various characterization techniques including tensile testing, dynamic mechanical analysis, impact testing, rheological analysis, scanning electron microscopy, and differential scanning calorimetry were employed. The effects of prior thermal history and an extra annealing step on the properties of the injection molded RPET blends will also be presented.

1.2 Experiments

1.2.1 Materials

Scraps and pelletized RPET (PET-H.S.3915.90 plastic flake from 2-liter soda bottles) were received from Merlin Plastics Alberta Inc. The melting temperature (T_m) was 245 °C and the measured melt flow index (MFI) is 30 g/10 min and 60 g/10 min (weight 2.16 kg) at 260 °C and 270 °C, respectively. Thermoplastic elastomer with a density of 0.93 g/cm^3 (TPE, Santoprene 8211-45) was purchased from ExxonMobil Chemical. The TPE, also called thermoplastic dynamic vulcanizate (TPV), is an alloy between ethylene propylene diene monomer (EPDM) rubber and polypropylene (PP) with the rubber particles dispersed in the PP phase. Chain extender (CE, CESA-Extend 9930C) was supplied by Clariant Masterbatches. The chain extender is an epoxy-functional styrene acrylic copolymer (oligomeric coupling agent) that has functional groups that may be added to degraded condensation polymers to re-link polymer chains broken by thermal, oxidative, or hydrolytic degradation. Poly(butylene adipate-co-terephthalate (PBAT), a commercialized aliphatic-*co*-aromatic biodegradable and flexible copolymer and toughening agent, was purchased from BASF Corporation under the commercial name Ecoflex®.

1.2.2 Processing

The RPET was combined with CE, TPE, and/or PBAT in a variety of formulations (Table 1.1). RPET was dried in an oven for 10 hours at 110 °C before processing. Prior to injection molding, materials were melt compounded using a thermokinetic mixer (K-mixer). They were compounded in 200 g batches and discharged when the temperature reached 260 °C. There was no external heating source for blends in the K-mixer besides frictional (viscous) heat and the compounding process was completed in less than two minutes. This short heating/mixing time reduces the potential for further thermal degradation. The K-mixer's rotor speed was 4000 rpm. After discharge, the molten blend was pressed into a flat sheet and subsequently granulated. Tensile bars (ASTM D638) were injection molded using a Boy 22S injection molding machine. Solid tensile bars were molded at the processing conditions shown in Table 1.2.

Table 1.1 Percent composition (by weight) of the materials compounded.

No.	**Sample**	**RPET (%)**	**CESA-Extend 9930C (%)**	**PBAT (%)**	**Thermoplastic Elastomer (TPE) (%)**
1	RPET + 1.3% CE	98.7	1.3	0	0
2	RPET + 25% PBAT + 1.3% CE	73.7	1.3	25	0
3	70% RPET + 30% TPE	70	0	0	30
4	50% RPET + 50% TPE	50	0	0	50
5	TPE	0	0	0	100

Table 1.2 Injection molding conditions used to mold the ASTM tensile bars.

Mold temperature (°C)	46
Nozzle temperature (°C)	260
Injection speed (cm^3/sec)	14
Packing pressure (bar)	90
Packing time (sec)	10
Screw (RPM)	35
Cooling time (sec)	20

1.2.3 Differential Scanning Calorimetry (DSC)

A differential scanning calorimeter (DSC 200 PC Phox®) was used to study the properties of the blended materials. Specimens of 4 to 5 mg were placed in aluminum sample pans and heated from 25 °C to 270 °C at a 10 °C/min heating rate and held for 5 min at 270 °C to erase any prior thermal history before cooling at 10 °C/min to 25 °C. The specimens were then reheated to 270 °C and cooled down to room temperature using the same heating and cooling rates of 10 °C/min. The crystallization temperature (T_c), melting temperature (T_m), apparent melting enthalpy (ΔH_f), and enthalpy of cold crystallization (ΔH_{cc}) were determined from DSC curves. Parameters T_m and ΔH_f were taken as the peak temperature and the area of the melting endotherm, respectively.

The absolute degree of crystallinity (χ_c) of the RPET phase was calculated by

$$\chi_c\,(\%) = \frac{\Delta H_f\,(RPET)}{\Delta H^{\circ}(RPET)} \times \frac{100}{w} \tag{1.1}$$

where ΔH°(RPET) is the enthalpy of melting per gram of 100% crystalline (perfect crystal) (120 J/g) and w is the weight fraction of RPET in the blend [9].

To determine the original crystallinity of the injection molded sample that was subjected to rapid cooling during the molding process, the extra heat released by the amorphous phase forming crystallites during heating (i.e., enthalpy of cold crystallization) was subtracted from the total endothermic heat flow due to the whole crystallites. Thus, the modified equation for the original crystallinity of the injection molded sample can be written as follows:

$$\chi_c\,(\%\ \text{Crystallinity}) = \frac{\Delta H_f\,(RPET) - \Delta H_{cc}\,(RPET)}{\Delta H^{\circ}(RPET)} \times \frac{100}{w} \tag{1.2}$$

1.2.4 Mechanical Testing

Tensile and notched Izod impact tests were performed on the injection molded samples following the ASTM-D-638-02 and ASTM-D-256-02 standards, respectively. The static tensile modulus, strength, and strain-at-break were measured at room temperature (~25 °C) and atmospheric conditions (relative humidity of ~50 ± 5%) on an MTS Sintech-10/GL mechanical testing instrument. Additional tensile tests were performed on the molded tensile bars after the specimens went through an annealing step in an oven. That is, the tensile bars were placed in an oven and slowly heated from 25 ºC to 185 ºC and then cooled to room temperature before the test. The tensile testing was performed on all specimens using an initial load of 0.5 N and a constant crosshead speed of 12.7 mm/min (0.5 in/min).

Prior to impact testing, rectangular specimens approximately 63.5 by 12.7 by 3.2 mm were cut from injection molded parts. The notched specimens were conditioned at ~25 °C and a relative humidity of 50 ± 5%. Five specimens of each sample group were tested and the average results were reported.

1.2.5 Dynamic Mechanical Analysis (DMA)

Dynamic mechanical analysis measurements were performed on an RSAIII DMA instrument in three-point bending mode. The dimensions of the rectangular specimen were about 17.6 by 12.7 by 3.2 mm, which were cut from injection-molded parts. During the DMA test, the specimens were heated at a rate of 3 °C/min from –45 ºC to 185 ºC with a frequency of 1 Hz and a strain of 0.01%, which is in the linear viscoelastic region, as determined by a strain sweep. Additional specimens were tested after first being subject to the same heating cycle without sinusoidal deformation in an oven. That is, the specimens were placed in an oven and heated

from –45ºC to 185ºC at 3°C/min, akin to the heating scan used in the DMA test, then cooled to room temperature before DMA testing. Similar to that in the tensile testing, the purpose of the extra heating cycle prior to the test is to find out the effect of annealing on the dynamic mechanical properties of the molded RPET blend specimens.

1.2.6 Rheological Properties

The shear viscosities of the polymer blends compounded in this study were measured over a range of shear rates using a TA Instruments ARES-LSII rheometer with a parallel plate geometry (plate radius = 25 mm; gap = 3.5 mm). Disks of proper sizes were cut from the tensile bars and then inserted between the plates and brought to the testing temperature and gap thickness. Steady shear tests were made at 260 °C under a nitrogen gas purge in order to avoid thermo-oxidative degradation.

1.2.7 Scanning Electron Microscopy (SEM)

The fracture surfaces obtained from the tensile tests were examined using an SEM (LEO 1530) operated at 3 kV. The samples were frozen in liquid nitrogen and then quickly impact-fractured. All specimens were sputter-coated with a thin layer of gold (~20 nm) prior to examination.

1.3 Results and Discussions

1.3.1 Thermal Properties

Thermal properties of RPET blends, including crystallization and melting behaviors, were investigated using DSC. The thermograms (solid curves) for the five material compositions listed in Table 1.1 and the numerical values of temperatures obtained from the first and second heating cycles are plotted in Figures 1.2 and 1.3. The cooling run is shown in Figure 1.4. The corresponding thermal data are listed in Table 1.3. The data obtained from the first heating cycle include the effect of the prior thermal history of the injection-molded samples, while the data obtained from the second heating cycle allow for a direct comparison of the crystallization behavior of different materials after erasing the thermal history through the first heating cycle.

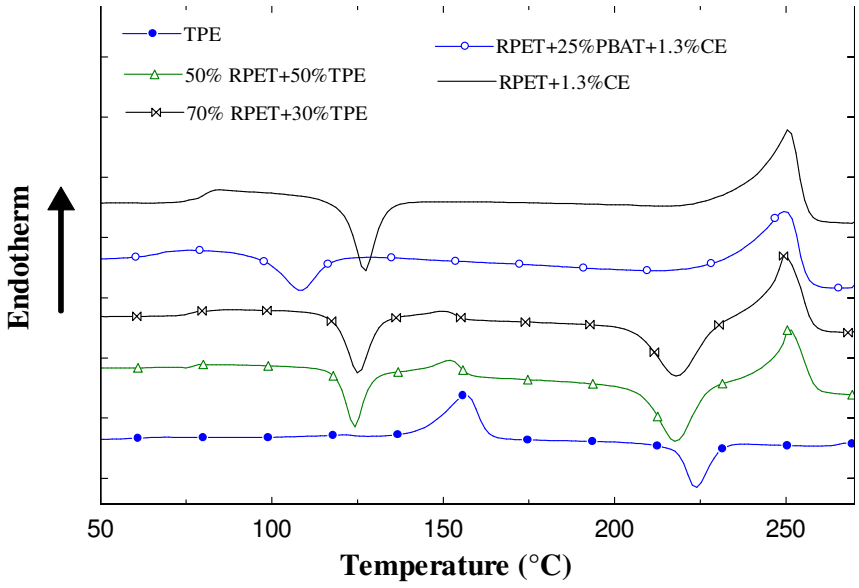

Figure 1.2 Melting curves of the PET blends. Data obtained from the first heating cycle.

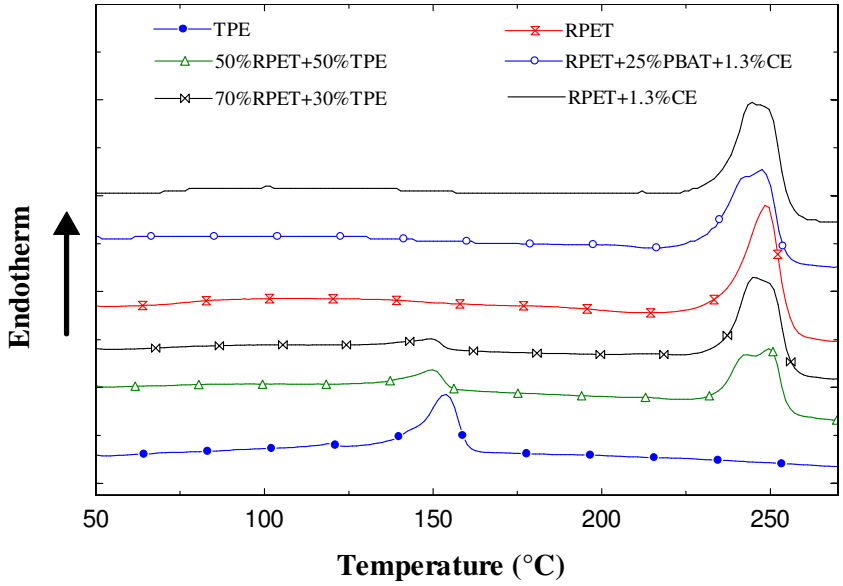

Figure 1.3 Melting curves of the RPET blends. Data obtained from the second heating cycle.

Table 1.3 Thermal characteristics of RPET blends.

Sample	RPET					TPE
	Cold Crystallization		Melting		Degree of crystallinity	Endothermic peak (ºC)
	Temp (ºC)	Enthalpy (J/g)	Temp (ºC)	Enthalpy (J/g)	χ_c (%)	
First heating						
RPET + 1.3% CE	126.75	–21.6	250.71	44	18.91	–
RPET + 25% PBAT + 1.3% CE	107.87	–14.57	248.66	43.01	32.15	–
70% RPET + 30% TPE	126.34	–18.64	250.71	30.86	14.33	149.74
50% RPET + 50% TPE	123.88	–13.31	251.53	21.21	13.16	150.56
TPE	–	–	–	–	–	155.9
Second heating						
RPET						
RPET + 1.3% CE	–	–	246.19	43.39	36.6	–
RPET + 25% PBAT + 1.3% CE	–	–	246.19	40.19	46.25	–
70% RPET + 30% TPE	–	–	246.6	34.74	28.95	149.74
50% RPET + 50% TPE	–	–	247	23.19	38.65	150.56
TPE	–	–	–	–	–	153.8

First Heating Cycle

As shown in Figure 1.2, TPE has one endothermic and one exothermic peak which occurred around 150 ºC and 220 ºC, respectively. Recall that the TPE used in this study is an alloy between EPDM rubber and PP with the rubber particles dispersed in the PP phase. An endothermic peak at a temperature around 150 ºC resulted from the melting of the crystalline polymer (PP) and the exothermic peak at a temperature around 220 ºC is the vulcanization process in residual, non-vulcanized rubber, hence the material gave off some heat.

Also, Figure 1.2 shows that two endothermic and two exothermic peaks were observed for RPET + TPE blends specimens (i.e., 70% RPET + 30% TPE and 50% RPET + 50% TPE). However, only one endothermic and one exothermic peak was shown for TPE, RPET + 1.3% CE and RPET + 25% PBAT + 1.3% CE specimens. The first exothermic peak for all RPET blend specimens (at a temperature range around 110 to 130 ºC) is referred to as the cold crystallization peak of RPET. The second exothermic peak (at a temperature of 220 ºC) corresponds to the vulcanization of TPE which occurred only with TPE blend specimens. Two exothermic peaks for RPET and TPE blends suggest that the two materials are immiscible. Recall that the specimens were taken from injection molded samples that underwent rapid cooling during the molding process, thereby impairing the crystallization process of the samples. Upon reheating during the DSC experiment, RPET molecules in the amorphous regions were able to rearrange and crystallize. With the addition of PBAT, the peak temperature of cold crystallization of RPET decreases. This indicates that the addition of PBAT promotes the onset of crystallization of the RPET material. The last peaks (at a temperature around 250 ºC) observed for all RPET blend specimens are the melting point of RPET. The shoulders around 60 to 80 ºC in the DSC thermograms in Figure 1.2 reveal the glass transition temperature of the RPET blends.

Table 1.3 shows the numerical values of temperatures and enthalpies from the first heating curve of the RPET blends. The enthalpies of crystallization and melting peaks of RPET decreased as the amount of TPE increased. However, the enthalpies of the melting peak of the RPET was still somewhat constant compared to RPET + 1.3% CE as PBAT was added, indicating that there was enhanced RPET crystallization during cooling during the injection molding process. As a result, there was higher crystallinity.

Second Heating Cycle

Figure 1.3 and Table 1.3 show the thermograms and numerically analyzed data of the RPET blends, respectively, from the second heating cycle. Unlike the first heating cycle, no exothermic peaks were observed because the prior thermal history of the injection-molded samples was erased in the first heating cycle. Figure 1.3 shows that double endothermic peaks (at temperatures around 150 ºC and 245 ºC) were obtained for the blends of RPET and TPE due to the differences in the endothermic temperatures of the two materials. Moreover, Figure 1.3 shows that there is only one melting peak at around the same temperature (around 245 ºC) for the RPET and the RPET + PBAT + CE blend but the melting peaks of RPET were wider for all the blends. This indicates that the addition of CE and PBAT does not affect the melting temperature of RPET. Also, as in the case of the first heating cycle, the addition of PBAT increased the crystallinity of RPET and the degree of crystallinity of all samples was found to be higher than that obtained during the first heating cycle.

Cooling Cycle

Also as shown in Figure 1.4, two exothermic peaks were observed for the RPET + TPE blend specimens (i.e., 70% RPET + 30% TPE and 50% RPET + 50% TPE). The first exothermic peak (at a temperature range around 95 to 105 ºC) corresponds to the crystallization of the PP phase in the TPE. The second endothermic peak (at a temperature of 190 to 220 ºC) is the

crystallization peak of RPET. However, only one exothermic peak was shown for TPE, RPET + 1.3% CE, and RPET + 25% PBAT + 1.3% CE specimens. The exothermic peak of the TPE is associated with the crystallization of the PP phase in the TPE whereas for the RPET + 1.3% CE and RPET + 25% PBAT + 1.3% CE specimens the peak is due to the crystallization of the RPET. The crystallization temperature of RPET alone was found to be lowest among all of the samples, suggesting that the presence of other materials (e.g., PBAT or CE) as additives facilitated the crystal nucleation process and resulted in a higher crystallization temperature. Two exothermic peaks for RPET and TPE indicate that the two materials are immiscible.

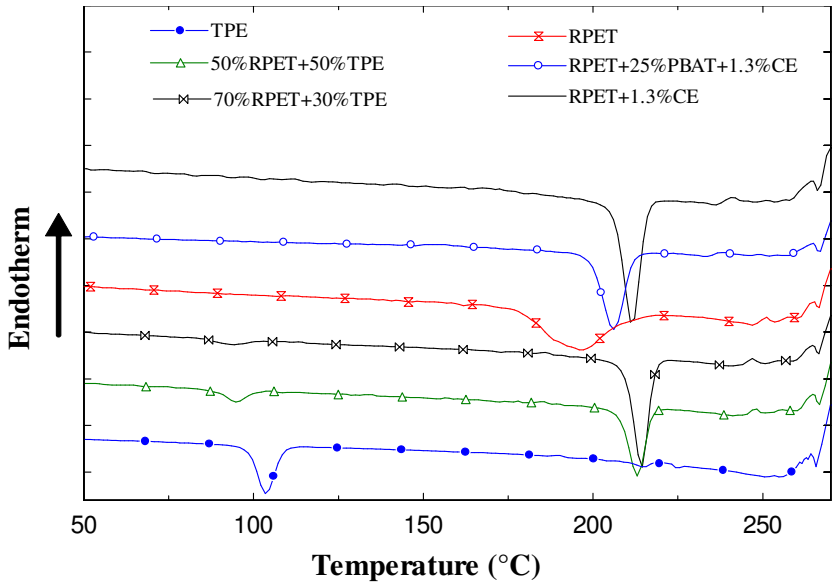

Figure 1.4 Melting curves of the RPET blends. Data obtained from the cooling cycle.

1.3.2 Tensile and Impact Properties

Tensile tests (according to ASTM-D-638-02) were performed on the injection molded specimens of the RPET blends. Properties such as tensile modulus, tensile strength, and strain at break were measured as shown in Table 1.4. The representative stress–strain curves are featured

in Figure 1.5. As can be seen in Table 1.4 and Figure 1.5, RPET + 1.3% CE and RPET + 25% PBAT + 1.3% CE specimens were not broken at the pre-set maximum strain. The strain-at-break of RPET blended with TPE became higher as the amount of TPE increased but their strength and modulus were lower than those of PET blended with CE and PBAT. The strain at break of 70% RPET + 30% TPE and 50% RPET + 50% TPE was found to be 0.1 and 0.115, respectively. The less than desired strain at break and mechanical properties of the RPET + TPE blends were probably due to the difference in the polarities between RPET and TPE.

As shown in Table 1.4 and Figure 1.5, the RPET with 1.3% CE had the highest value of ultimate tensile strength, which was 53.2 MPa. For the RPET + 25% PBAT + 1.3% CE with a 25% increase in the PBAT the ultimate tensile strength decreased to 39.4 MPa. The tensile strengths for 70% RPET + 30% TPE and 50% RPET + 50% TPE were found to be 18.9 MPa and 5.9 MPa, respectively. A similar trend was observed for the tensile modulus. The RPET with 1.3% CE had the highest value of ultimate tensile modulus following by RPET + 25% PBAT + 1.3% CE, 70% RPET + 30% TPE, and 50% RPET + 50% TPE.

Table 1.4 Mechanical properties of RPET blends.

Sample	**Ultimate Tensile Strength (MPa)**	**Tensile Modulus (MPa)**	**Strain at Break**	**Impact Strength (kJ/m^2)**
RPET + 1.3% CE	53.2±3.08	1450.3±105.05	NB[a]	3.89±0.028
RPET + 25% PBAT + 1.3% CE	39.4±0.78	1181.1±124.40	NB	5.17±0.025
70% RPET + 30% TPE	18.9±0.43	773.3±62.33	0.1±0.02	3.33±0.005
50% RPET + 50% TPE	5.9±0.39	264.7±35.60	0.115±0.07	1.83±0.005
TPE	1.26±0.02	2.83±0.26	NB	NB
Heat treated sample				
RPET + 1.3% CE	62.6±9.3	1746.7±1.57	0.05±0.01	–
RPET + 25% PBAT + 1.3% CE	47.8±0.01	1281.8±11.22	0.23±0.02	–
70% RPET + 30% TPE	21.63±0.3	884.8±24.6	0.0544±0.002	–
50% RPET + 50% TPE	1.44±0.1	309.7±0.1	0.02±.01	–

[a]NB = Not broken.

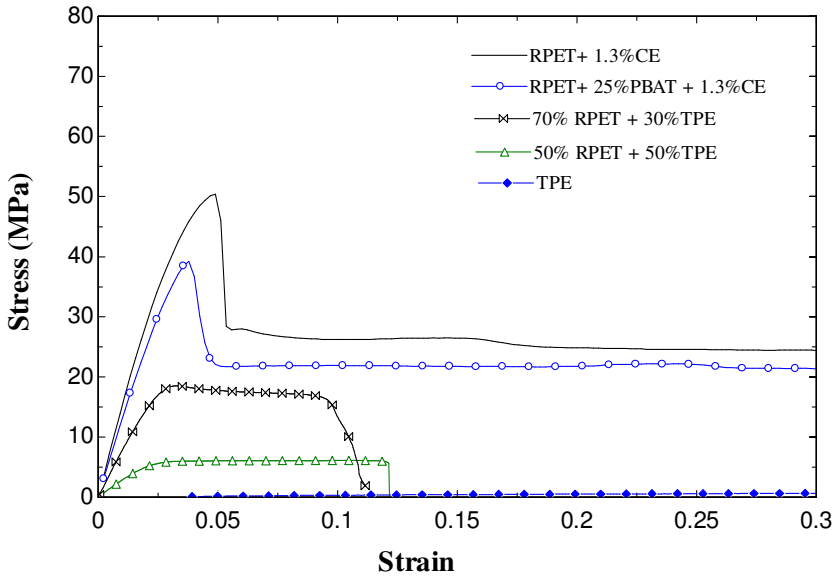

Figure 1.5 Tensile stress versus strain curves for the TPE and RPET blends.

Figure 1.6 represents the tensile test results of the RPET blends after subjecting them to an annealing step—slow heating from room temperature to 185 ºC, which is higher than the cold crystallization temperature of RPET, and then cooled to room temperature—before the test. Properties such as tensile modulus, tensile strength, and strain at break were also measured as shown in Table 1.4. As can be seen in Table 1.4 and Figure 1.6, the tensile modulus and tensile strength of the RPET blends were noticeably higher due to RPET recrystallization and became stronger and stiffer. RPET + 1.3% CE still had the highest value of ultimate tensile strength and tensile modulus, which was 62.6 MPa and 1746.7±1.57 MPa, respectively. However, both RPET + 1.3% CE and RPET + 25% PBAT + 1.3% CE samples were broken and all tensile bars were broken at a strain-at break lower than that of the untreated samples, which indicated that the ductility of the treated specimens was reduced. The strain-at-break of 50% RPET + 50% TPE was lowest at 0.02±.01.

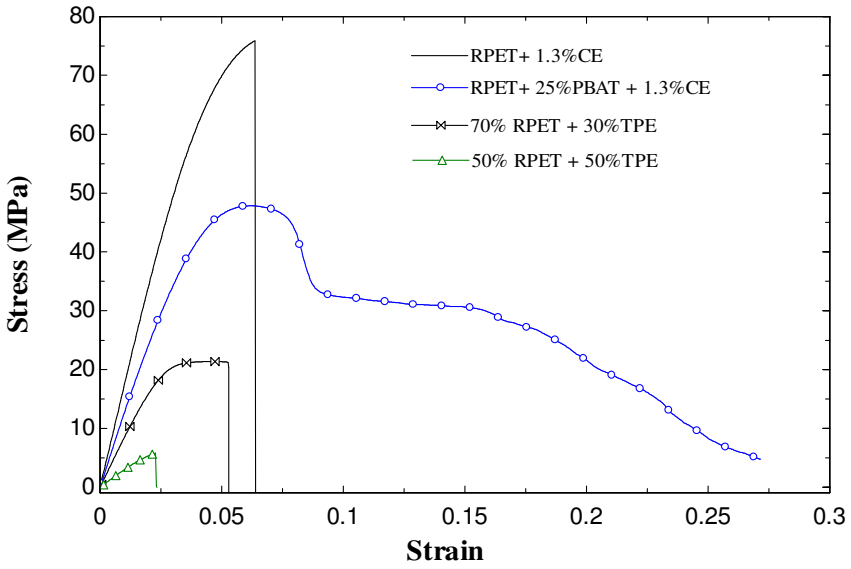

Figure 1.6 Tensile stress versus strain curves for the RPET blends after heat treatment.

The impact strengths of the four RPET blends and TPE are also shown in Table 1.4. As can be observed, the blend containing 50% RPET and 50% TPE exhibited the lowest impact strength among the RPET blends. Also shown in the Table is the addition of chain extenders (CE) that lead to a higher impact strength, which is about double the impact strength of the 50% RPET + 50% TPE. Nonetheless, all of these blends performed much better than the RPET alone, which is brittle and difficult to mold, let alone being tested for impact strength [23].

In general, RPET with chain extenders was found to have higher mechanical properties. This might be due to the fact that the chain extenders react and rejoin the broken chains of the hydroxyl (-OH) functional group or carboxyl (-COOH) end groups of PET during melt processing, thus leading to an increase in the blend's tensile strength and modulus [23], while RPET with TPE gave lower mechanical properties. The reason for the lower mechanical properties resulted from an incompatibility between the RPET and TPE [14]. Finally, after the

RPET blend specimens were reheated beyond the cold-crystallization temperature, they became stronger but had a lower strain-at-break.

1.3.3 Dynamic Mechanical Properties (DMA)

The viscoelastic properties of the RPET blends were studied using DMA. The resulting storage moduli and glass transition temperatures in terms of tan-δ of all of the RPET blends are shown in Figures 1.7 and 1.8, respectively. Note that the storage moduli of all of the specimens decreased rapidly between 60 and 80 ºC (Figure 1.7) due to the glass transition temperature of RPET [24] (cf. Figure 1.8). Between 90 and 110 ºC, their moduli started to increase, which corresponds to the range of the cold crystallization temperature of RPET (cf. Figure 1.2). The increase in crystallinity during cold crystallization increases the rigidity of the specimen. Since the RPET + 25% PBAT + 1.3% CE has the lowest cold crystallization temperature (cf. Figure 1.2), the transitions in storage modulus and glass transition temperature also occur at the lowest temperature. The storage modulus of 50% RPET + 50% TPE was the lowest and RPET + 1.3 %CE was the highest at high temperature. While the glass transition of the blends can be easily identified by the peaks in the tan- δ curves in Figure 1.8, one can also see a weak transition appeared at about 115 ºC, which is assigned to the cold crystallization temperatures of RPET [3]. Note that the T_g of the PET–PBAT blend is lower than that of the RPET–TPE and RPET–CE blends at around 73.6 ºC and the T_g of the RPET + 1.3% CE is highest at around 82.9 ºC. Table 1.5 tabulates the glass transition temperatures of the various RPET blends based on the tan-δ curves.

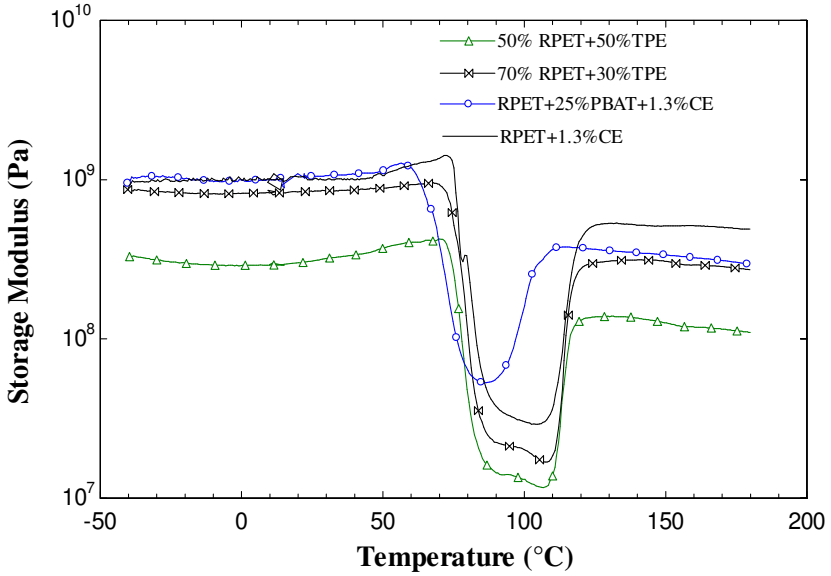

Figure 1.7 Storage moduli of the RPET blends for specimens cut directly from injection molded tensile test bars.

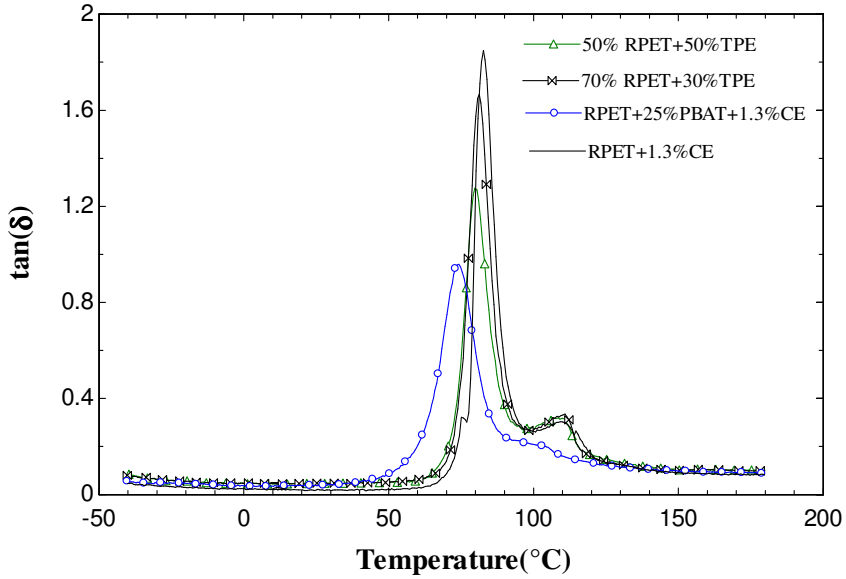

Figure 1.8 Tan-δ curves of the RPET blends.

Figure 1.8 presents the DMA results of the specimens with an additional heat treatment by subjecting them to the same DMA thermal history (i.e., heating at a rate of 3 °C/min from –45

ºC to 185 ºC) without loading. Interestingly, the substantial drop in the storage moduli previously shown in Figure 1.7 disappeared with the new test specimens. This suggests that the extra "annealing process" allowed the cold crystallization process to occur prior to DMA testing. For the new DMA tests, only a small declining trend was observed for the storage moduli of all specimens as the temperature increased with the most rapid reduction occurring at the glass transition region. In the glassy region (< 60 ºC), the storage modulus of the specimen is highest when PET was blended with 1.3% CE. The addition of 25% PBAT decreased the storage modulus but it was still higher than that of the RPET and TPE blends.

In the glass transition region, two crossovers were observed between the RPET + 1.3% CE, RPET + 25% PBAT + 1.3% CE, and 70% RPET + 30% TPE because of the glass transition of RPET. Above the glass transition region, the storage moduli of all specimens continued to decrease with increasing temperature.

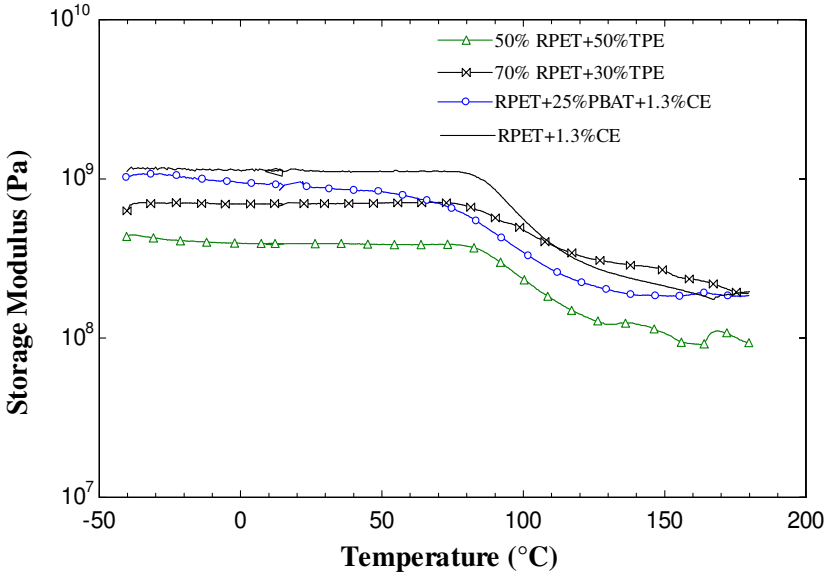

Figure 1.9 Storage moduli of the RPET blends after heat treatment.

The temperature dependence of the tangent (tan-δ) of the blends after the heat treatment is presented in Figure 1.10. The glass transition temperature (T_g) is obtained from the peaks of the tan-δ curves. Note that the glass transition temperatures increase slightly compared to those of the specimens without the heat treatment. In particular, the T_g of the RPET–PBAT blend is lower than that of the RPET–TPE and RPET–CE blends at around 93.6 ℃ and the T_g of 50% RPET + 50% TPE is highest at around 101.5 ℃ due to the fact that the material had the lowest amount of RPET. Table 1.5 tabulates the new glass transition temperatures of the various RPET blends based on the tan-δ curves.

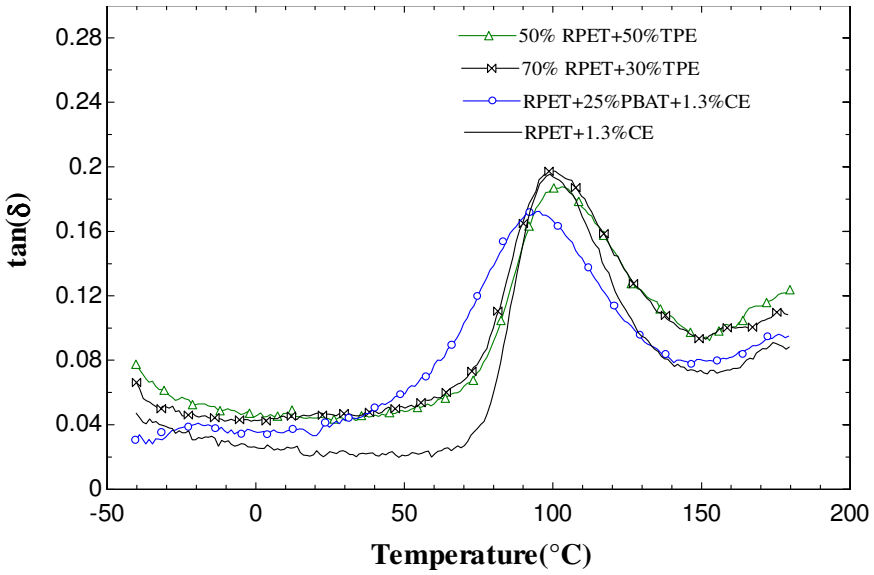

Figure 1.10 Tan-δ curves of the RPET blends after heat treatment.

Table 1.5 Glass transition temperatures of RPET blends.

No.	Sample	Glass Transition Temperature (°C)	Glass Transition Temperature (°C) (heat treated sample)
1	RPET + 1.3% CE	82.9	98.7
2	RPET + 25% PBAT + 1.3% CE	73.6	93.6
3	70% RPET + 30% TPE	81.6	99.7
4	50% RPET + 50% TPE	79.6	101.5

1.3.4 Rheological Properties

The modification of the molecular structure during processing is reflected in the rheological characteristics of the RPET samples. A significant increase in viscosity due to the addition of CE in RPET is evident from the log–log viscosity–shear rate curves reported in Figure 1.11. Furthermore, there is only a minor difference in the shear viscosity between the RPET + 1.3% CE and the RPET + 25% PBAT + 1.3% CE. This significant increase in viscosity suggests that the CE increased the molecular weight of the RPET; namely, the CE rejoins the broken chains of the hydroxyl or carboxyl end groups [23].

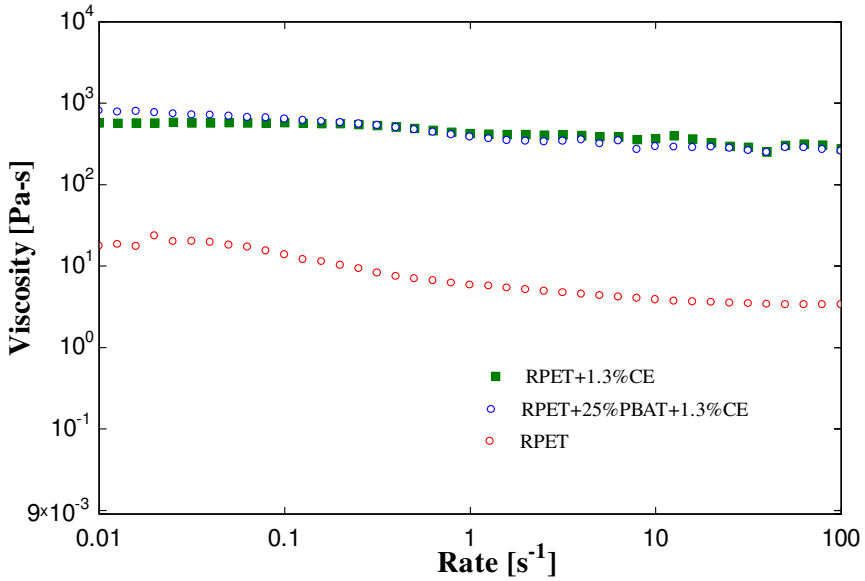

Figure 1.11 Viscosity curves for RPET–CE and PET–PBAT–CE blends (T = 260 °C).

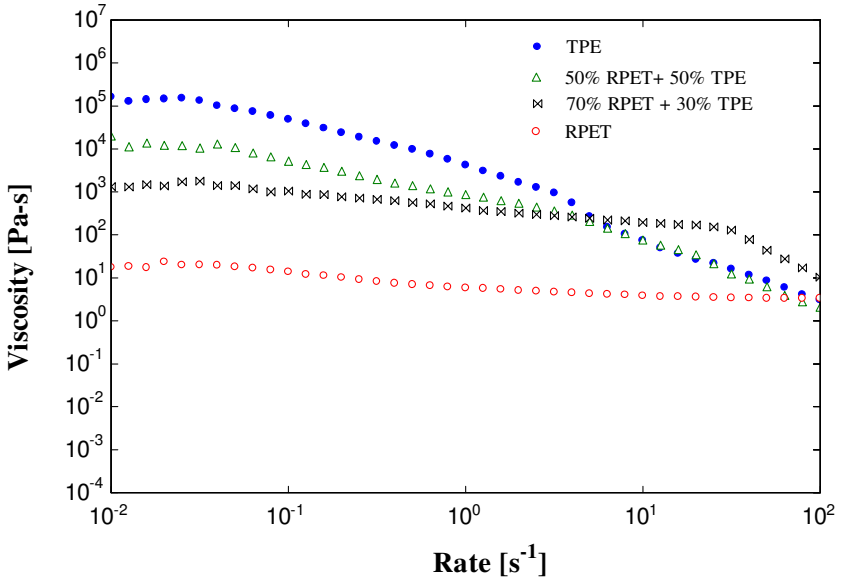

Figure 1.12 Viscosity of RPET, TPE, and RPET+TPE blends.

Figure 1.12 shows a plot of log–log shear viscosity for RPET blended with TPE as a function of shear rate. At low shear rates, the TPE's viscosity is about 10^5 Pa·s while RPET's viscosity is about 10^1 Pa·s. The shear viscosity of RPET shows only a very slight decrease with increasing shear rate initially and then almost behaves like a Newtonian fluid, suggesting a much reduced molecular weight resulting from the degradation. For the case of RPET + TPE, as the amount of TPE material is increases, the viscosity increases and becomes more like TPE. Shear thinning behavior can also be observed in these curves, especially with TPE and PET + TPE blends.

1.3.5 Fracture Surface Analysis via SEM

Figure 1.13 shows representative SEM images of RPET blends. All images were taken at the same magnification (scale bar: 100µm). These SEM images provide information on the

microstructure and the fracture behavior of the specimens. The fracture surfaces of the PET + CE and PET + PBAT + CE blends are rather smooth and suggest brittle fracture after cryogenic freezing, whereas the blends of RPET and TPE show some small cavities. The reason for the formation of these cavities in the blends is probably due to the volatile compounds released during vulcanization in the TPE phase that contribute to the weight reduction. The tensile bars of PET + 1.3% CE, RPET + 25% PBAT + 1.3% CE, 70% PET + 30% TPE, and 50% PET + 50% TPE weighed about 9.4, 9.2, 8.34, and 7.52 g, respectively.

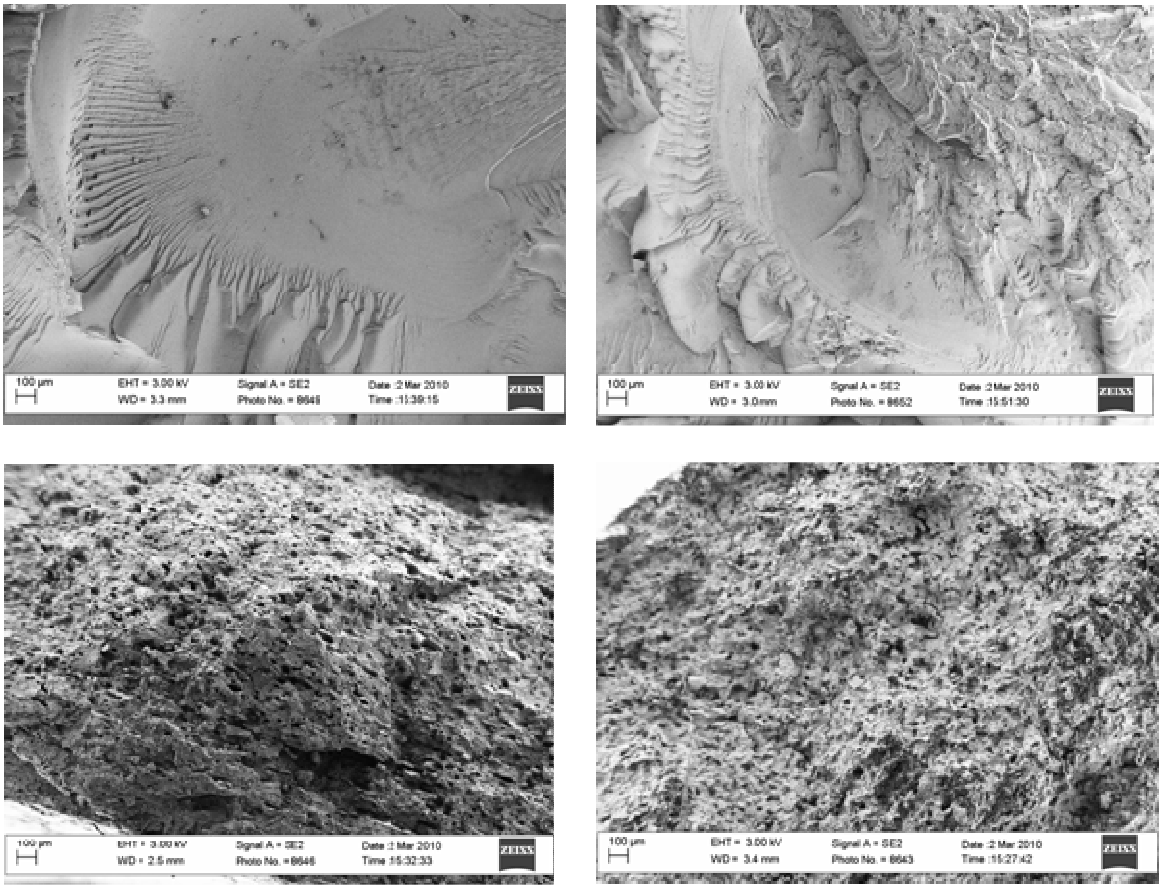

Figure 1.13 SEM images of (a) RPET + 1.3% CE, (b) RPET + 25% PBAT + 1.3% CE, (c) 70%RPET + 30% TPE, and (d) 50% RPET + 50% TPE.

1.4 Conclusions

The mechanical properties of RPET can be improved by the addition of chain extenders (CE), and poly(butylene adipate-co-terephthalate) (PBAT), or thermoplastic elastomer (TPE). The storage moduli of the injection molded RPET blends at elevated temperatures (i.e., above the glass transition temperature) can also be enhanced through an annealing process that increases the degree of crystallinity although the materials would have lower strain-at-break. More importantly, the enhanced moldability also allows them to be easily molded via injection molding, thereby enabling the recycling of PET for a host of applications. By adding chain extenders, the molecular weight of RPET increases, as does its viscosity and mechanical properties. Even though adding TPE enhances the moldability, RPET and TPE are immiscible, thus limiting the improvements in mechanical properties. Compatibilizers are needed to improve the mechanical properties of the blends.

1.5 References

1. Hernandez RJ, Selke SEM, Culter JD. Plastics packaging: properties, processing, applications, and regulations: Hanser Munich; 2000.
2. Kang D. An exploration into the use of stepwise regression analysis to determine post-consumer recycled PET content in PET sheet, MICHIGAN STATE UNIVERSITY; 2009.
3. Zhang Y, Guo W, Zhang H, Wu C. Influence of chain extension on the compatibilization and properties of recycled poly (ethylene terephthalate)/linear low density polyethylene blends. Polymer Degradation and Stability.94(7):1135-1141, 2009.
4. Buxbaum L. THE DEGRADATION OF POLY (ETHYLENE TEREPHTHALATE): Goodyear Tire and Rubber Co., Akron, Ohio;1968.

5. Schnabel W. Polymer degradation, principles and practical applications. W. Schnabel, Hahn-Meitner Institute, Berlin, ISBN 0-02-949640-3, 220, 1986.

6. Grassie N, Scott G. Polymer degradation and stabilisation: Cambridge University Press; 1988.

7. Cardi N, Po R, Giannotta G, Occhiello E, Garbassi F, Messina G. Chain extension of recycled poly (ethylene terephthalate) with 2, 2′-Bis (2-oxazoline). Journal of applied polymer science.50(9):1501-1509, 2003.

8. Torres N, Robin J, Boutevin B. Study of thermal and mechanical properties of virgin and recycled poly (ethylene terephthalate) before and after injection molding. European polymer journal.36(10):2075-2080, 2000.

9. Kiliaris P, Papaspyrides C, Pfaendner R. Reactive-extrusion route for the closed-loop recycling of poly (ethylene terephthalate). Journal of applied polymer science.104(3):1671-1678, 2007.

10. Canetti M, Bertini F. Supermolecular structure and thermal properties of poly (ethylene terephthalate)/lignin composites. Composites Science and Technology.67(15):3151-3157, 2007.

11. Friedrich K, Evstatiev M, Fakirov S, Evstatiev O, Ishii M, Harrass M. Microfibrillar reinforced composites from PET/PP blends: processing, morphology and mechanical properties. Composites Science and Technology.65(1):107-116, 2005.

12. Fuchs C, Bhattacharyya D, Fakirov S. Microfibril reinforced polymer-polymer composites: Application of Tsai-Hill equation to PP/PET composites. Composites Science and Technology.66(16):3161-3171, 2006.

13. Hernandez JJ, Garcia-Gutierrez MC, Nogales A, Rueda DR, Ezquerra TA. Small-angle X-ray scattering of single-wall carbon nanotubes dispersed in molten poly(ethylene terephthalate). Composites Science and Technology.66(15):2629-2632, 2006.

14. Phinyocheep P, Saelao I, Buzare JY. Mechanical properties, morphology and molecular characteristics of poly(ethylene terephthalate) toughened by natural rubber. Polymer.48(19):5702-5712, 2007.

15. Mouzakis D, Papke N, Wu J, Karger-Kocsis J. Fracture toughness assessment of poly (ethylene terephthalate) blends with glycidyl methacrylate modified polyolefin elastomer using essential work of fracture method. Journal of applied polymer science.79(5):842-852, 2001.

16. Papke N, Karger-Kocsis J. Thermoplastic elastomers based on compatibilized poly (ethylene terephthalate) blends: effect of rubber type and dynamic curing. Polymer.42(3):1109-1120, 2001.

17. Loyens W, Groeninckx G. Ultimate mechanical properties of rubber toughened semicrystalline PET at room temperature. Polymer.43(21):5679-5691, 2002.

18. Loyens W, Groeninckx G. Rubber toughened semicrystalline PET: influence of the matrix properties and test temperature. Polymer.44(1):123-136, 2003.

19. Al-Malaika S, Kong W. Reactive processing of polymers: effect of in situ compatibilisation on characteristics of blends of polyethylene terephthalate and ethylene-propylene rubber. Polymer.46(1):209-228, 2005.

20. Sánchez-Solís A, Calderas F, Manero O. Influence of maleic anhydride grafting on the rheological properties of polyethylene terephthalate–styrene butadiene blends. Polymer.42(17):7335-7342, 2001.

21. Fung K, Li RKY. A study on the fracture characteristics of rubber toughened poly (ethylene terephthalate) blends. Polymer testing.24(7):863-872, 2005.

22. Haralabakopoulos A, Tsiourvas D, Paleos C. Chain extension of poly (ethylene terephthalate) by reactive blending using diepoxides. Journal of applied polymer science.71(13):2121-2127, 1999.

23. Tang X, Guo W, Yin G, Li B, Wu C. Reactive extrusion of recycled poly (ethylene terephthalate) with polycarbonate by addition of chain extender. Journal of applied polymer science.104(4):2602-2607, 2007.

24. Zhang Y, Zhang H, Yu Y, Guo W, Wu C. Recycled poly (ethylene terephthalate)/linear low-density polyethylene blends through physical processing. Journal of applied polymer science.114(2):1187-1194, 2009.

CHAPTER 2

Effects of Annealing Time and Temperature on the Crystallinity and Dynamic Mechanical Behavior of Injection Molded Poly(lactic Acid) (PLA)

2.1 Introduction

Poly(lactic acid) or polylactide (PLA) is a biodegradable thermoplastic polyester obtained by synthesis of lactic acid (or lactide), which can be produced from renewable resources such as corn or sugarcane. Mass produced and commercially available PLA has been successfully introduced for products where biodegradability or sustainability is required or desired [1, 2]. PLA is an enantiomeric polyester including poly(L-lactic acid) (PLLA) and poly(D-lactic acid) (PDLA). Fully amorphous materials can be made by the inclusion of relatively high D content (>20%) whereas highly crystalline material is obtained when the D content is low (<2%) [3]. Obtaining a highly crystalline, injection-molded PLA part remains difficult due to PLA's slow crystallization rate [4]. The polymer's crystallinity plays a significant role in the material's performance. For example, an increase in overall crystallinity leads to improvements in stiffness, strength, heat deflection temperature, and chemical resistance [5, 6]. Various techniques for determining the crystallinity of polymers were discussed in [7], which include (1) x-ray diffraction, XRD, (2) Fourier transform infrared spectroscopy, FTIR, (3) differential scanning calorimetry, DSC, and (4) material density measurements. To maximize property enhancements with a high degree of crystallinity in the injection molded part, the cooling rate has to be slow (leading to a long cycle time), or alternatively, annealing of post-injection molded part is needed

[4, 8]. The latter approach can be done offline and in batches, thereby offering a cost-effective way to improve the performance of PLA parts without affecting the cycle time.

In this study, the degree of crystallinity in injection molded and annealed PLA specimens under different annealing times and temperatures was investigated. The relationship between annealing time and temperature was studied through time–temperature superposition following the WLF and Arrhenius equations. Furthermore, the heat resistance and mechanical performance of as molded and annealed specimens were assessed.

2.2 Experiments

2.2.1 Sample Preparation

The specimens used in this study were injection molded ASTM test bars of PLA (NatureWorks® 3001D). PLA has a high optical purity, containing mainly L-lactic acid with 1.4% ± 0.2% D-lactic acid and has a thermal conductivity of 0.13 W/m-K. Flexural specimens (nominal dimensions of 125.0 mm by 12.7 mm by 3.2 mm) and tensile bars (ASTM D638 Type V, 63.5 mm by 3.2 mm by 1.6 mm) were injection molded using a micro injection molding machine (DSM Xplore, Geleen, The Netherlands). The molding was done at 190 ºC with a mold temperature of 25 ºC, a cooling time of 15 seconds, and a holding pressure of 10 bar. Some of the molded bars underwent additional annealing treatments at 65, 70, 75, and 80 ºC, respectively, for varying lengths of time. Prior to annealing, injection molded PLA bars were kept at room temperature (25 ºC) before being placed in a hot oven at a temperature of 65, 70, 75 and 80 ºC for a period of time. The Biot number (Bi), which was calculated to examine the temperature uniformity within the sample, is defined as the ratio of surface heat convection to thermal conduction within the object

$$Bi = \frac{\bar{h}L}{k} \tag{2.1}$$

where $\bar{h}$ is the heat convection coefficient (15 W/m^2-K) [9], k is thermal conductivity, and L is the conduction length within the molded PLA (m). If Bi is small, it can be assumed that the temperature of the PLA bars is uniform at any given time [9]. It was found that Bi was less than 0.13, which suggests that the temperature gradient in the samples was small.

The as-molded specimens were transparent, an indication of an amorphous state, and changed to cloudy after annealing at the higher temperatures and longer annealing times, suggesting an increase in the degree of crystallinity.

2.2.2 Differential Scanning Calorimetry (DSC)

A differential scanning calorimeter (TA Q100) was used to study the degree of crystallinity of the PLA annealed at different times and temperatures. In this procedure, 4 to 5 mg specimens were cut from the center of the annealed bars and placed in aluminum pans. They were then heated from 25 to 200 °C at a 10 K/min heating rate**.** The melting temperature (T_m), apparent melting enthalpy (ΔH_f), and enthalpy of cold crystallization (ΔH_{cc}) were determined from DSC thermograms. Parameters T_m and ΔH_f were taken as the peak temperature and the area of the melting endotherm, respectively.

The absolute degree of crystallinity (χ_c) of the molded and annealed PLA phase was calculated by

$$\chi_c(\%) = \frac{\Delta H_f(PLA)}{\Delta H°(PLA)} \times 100 \tag{2.2}$$

where $\Delta H°(PLA)$ is the melting enthalpy per gram of 100% crystallinity (i.e., perfect crystalline structure) (93 J/g) [4].

To determine the original crystallinity of the injection molded and annealed specimens, the extra heat released during heating (i.e., enthalpy of cold crystallization) was subtracted from the total endothermic heat flow during melting of the whole crystallites[7]. Thus, the modified equation for the crystallinity of the injection molded and annealed specimens can be written as follows:

$$\chi_c(\%) = \frac{\Delta H_f(PLA) - \Delta H_{cc}(PLA)}{\Delta H°(PLA)} \times 100 \tag{2.3}$$

2.2.3 Wide-Angle X-ray Diffraction (XRD)

XRD has been traditionally accepted as a direct and universal technique for measuring the crystallinity of different semi-crystalline polymers [7]. The wide angle diffraction diagram of a semi-crystalline polymer is composed of the diffraction of the amorphous and crystalline regions. Whereas the crystal domains produce relatively distinct reflections, the amorphous phase produces a background, in the proximity of the most intense crystal reflections, possessing a broad maximum. This is known as an "amorphous halo" [10]. In this study, diffraction patterns were obtained on a Hi-Star 2-D diffractometer with a monochromatic CuK_α point source (0.8 mm) and a 1024 by1024 area detector. Molded and annealed bars at an annealing temperature of 75 ºC were analyzed. The spectra were resolved into amorphous halo phenomena and crystalline peaks. The degree of crystallinity was computed using the equation [10]:

$$\chi_c = A_c / (A_c + A_a) \tag{2.4}$$

where χ_c is the degree of crystallinity or % crystallinity, and A_c and A_a are the crystallized and amorphous areas on the X-ray diffractogram, respectively. The area (A_c) above the smooth curve was taken as the crystalline portion, while the lower area was taken as the amorphous portion.

The upper diffraction peak area and the total diffraction area were integrated over a diffraction angle of 10 to 30º.

2.2.4 Heat Resistance Analysis

To illustrate qualitatively how the heat resistance of as-molded and annealed PLA flexural bars is changed due to the annealing process, the straight specimens were first set in a fixture. Then, these specimens were placed into an oven at 65 ºC for 3 min to observe the deformation of the as-molded and annealed PLA specimens under their own weight.

2.2.5 Tensile Testing

Tensile test was performed on the injection molded (as-molded) and annealed PLA samples following the ASTM D638 standard [11]. The static tensile modulus, strength, and strain-at-break were measured at room temperature (25 °C) and atmospheric conditions (relative humidity of 50 ± 5%) on an Instron 5865 mechanical testing instrument. The tensile testing was performed on all specimens using an initial load of 0.5 N and a constant crosshead speed of 1 mm/min.

2.2.6 Dynamic Mechanical Analysis (DMA)

Dynamic mechanical analysis measurements were performed on a DMA Q800 (TA instrument) in single cantilever mode. The dimensions of the rectangular specimen were 17.6 mm by 12.7 mm by 3.2 mm, which were cut from injection molded and annealed parts. During the DMA test, the specimens were heated at a rate of 3 K/min from –30 to 120 ºC with a frequency of 1 Hz and a strain of 0.02%, which is in the linear viscoelastic region as determined by a strain sweep.

2.3 Results and Discussions

2.3.1 DSC Data

The DSC scans of the injection molded PLA specimens heat treated for varying amounts of time at annealing temperatures of 65, 70, 75, and 80 ºC are presented in Figures 2.1(a) through (d), respectively. The curves consisted of four thermal characteristics: (1) a glass transition temperature (T_g) near 60 ºC, (2) a cold crystallization peak ranging from 88 to 108 ºC, (3) a recrystallization peak around 152 ºC, and finally (4) an endothermic fusion peak (melting peak, T_m) with a maximum near 170 ºC. The annealing temperature varied from just above T_g (around 60 ºC) to the cold crystallization peak temperature [4, 8]. During injection molding, the crystallization process was partially hampered due to the high cooling rate. As a result, it is typical for injection molded parts to exhibit a cold crystallization peak during the DSC test when the specimens are re-heated and regain some mobility to re-crystallize.

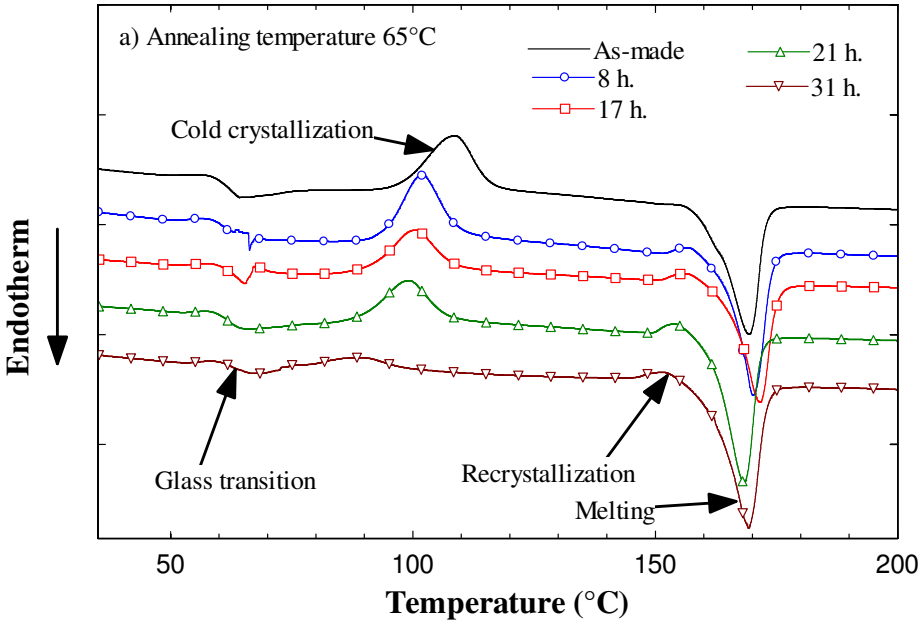
a) Annealing temperature 65°C
As-made
8 h.
17 h.
21 h.
31 h.
Cold crystallization
Endotherm
Glass transition
Recrystallization
Melting
50
100
150
200
Temperature (°C)

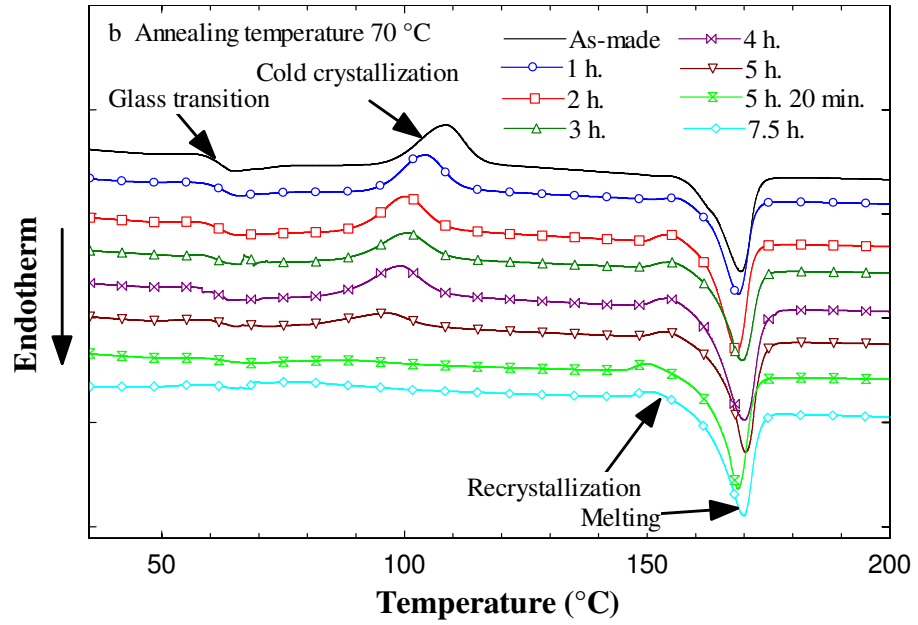
b Annealing temperature 70 °C
As-made
1 h.
2 h.
3 h.
4 h.
5 h.
5 h. 20 min.
7.5 h.
Cold crystallization
Glass transition
Endotherm
Recrystallization
Melting
50
100
150
200
Temperature (°C)

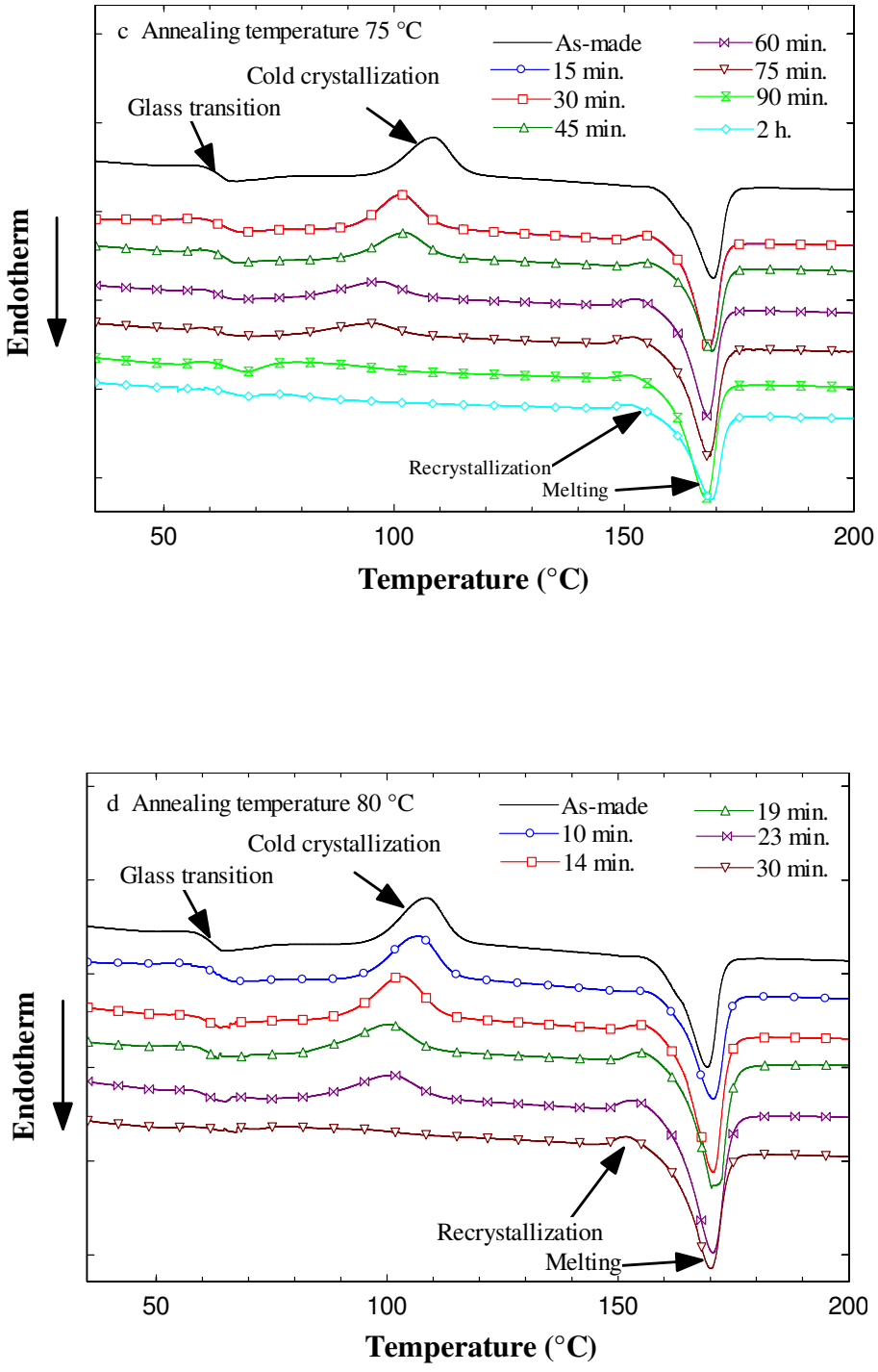

Figure 2.1 DSC heating scans showing the effect of annealing time at (a) 65 ºC, (b) 70 ºC, (c) 75 ºC, and (d) 80 ºC.

Table 2.1 Thermal characteristics and degree of crystallinity of PLA samples

Sample	Cold Crystallization		Recrystallization		Melting		χ_c (%)
	T_{cc} (°C)	ΔH_{cc} (J/g)	T (°C)	ΔH (J/g)	T_m (°C)	ΔH_f (J/g)	
PLA as-molded	108.6	27.00	-	-	169.2	41.8	15.86
Annealing temperature 65 °C							
• Annealing 8 h	101.6	27.88	156.8	1.45	170.0	43.92	15.69
• Annealing 17 h	100.2	21.50	156.3	1.60	171.5	40.92	19.16
• Annealing 21 h	99.1	20.88	154.3	2.18	168.3	47.34	26.10
• Annealing 31 h	89.6	4.03	151.7	1.37	169.1	46.01	43.67
Annealing temperature 70 °C							
• Annealing 1 h	104.2	22.93	155.9	0.45	168.7	37.95	15.66
• Annealing 2 h	100.3	21.70	154.5	2.03	168.5	43.36	21.10
• Annealing 3 h	100.3	20.34	154.8	1.55	169.5	42.09	21.72
• Annealing 4 h	99.4	18.12	154.3	1.90	170.0	46.09	28.03
• Annealing 5 h	97.0	9.58	153.8	1.13	170.1	44.29	36.10
• Annealing 5.3 h	-	-	150.0	2.07	168.6	48.52	49.9
• Annealing 7.5 h	-	-	150.6	1.10	169.7	45.26	47.48
Annealing temperature 75 °C							
• Annealing 15 min	103.9	25.25	156.0	0.70	168.8	39.87	14.96
• Annealing 30 min	101.7	25.63	154.9	1.50	168.4	46.45	20.77
• Annealing 45 min	102.2	23.39	155.2	1.10	169.0	43.17	20.08
• Annealing 60 min	97.1	14.58	152.6	2.36	167.9	50.14	35.70
• Annealing 75 min	95.5	12.23	152.1	2.11	168.0	50.52	38.90
• Annealing 90 min	79.8	4.28	151.4	0.89	167.6	48.77	46.88
• Annealing 2 h	-	-	151.3	1.17	168.8	45.67	47.84
Annealing temperature 80 °C							
• Annealing 10 min	106.8	24.10	155.4	0.16	170.6	39.50	16.39
• Annealing 14 min	103.3	21.01	155.4	0.96	170.4	41.45	20.95
• Annealing 19 min	100.4	16.18	155.1	1.37	164.0	40.45	24.62
• Annealing 23 min	101.1	13.68	153.5	1.97	170.5	45.78	32.40
• Annealing 30 min	-	-	152.0	1.88	170.0	47.97	49.56

Table 2.1 shows the numerical values of temperature and enthalpy from the first heating curve of annealing PLA specimens at different annealing times and temperatures. As noticed in Figure 2.1 and Table 2.1, the enthalpy of the cold crystallization peaks decreased with increasing annealing time. This indicates that there was enhanced PLA crystallization during the annealing process, thereby leading to a higher degree of crystallinity prior to the DSC test. Moreover, longer annealing times shifted the cold crystallization temperature to a lower value. The recrystallization peak which was observed just before the melting peak may be due to the restructuring of certain existing crystalline structures at high temperatures.

Figure 2.2 shows the evolution of crystallinity as a function of annealing time and temperature. The maximum crystallinity of all PLA samples was around 48 to 49%. At 65 ºC, PLA reached 43% crystallinity in 31 hours whereas at 80 ºC, PLA reached its maximum crystallinity of around 49% in 30 minutes.

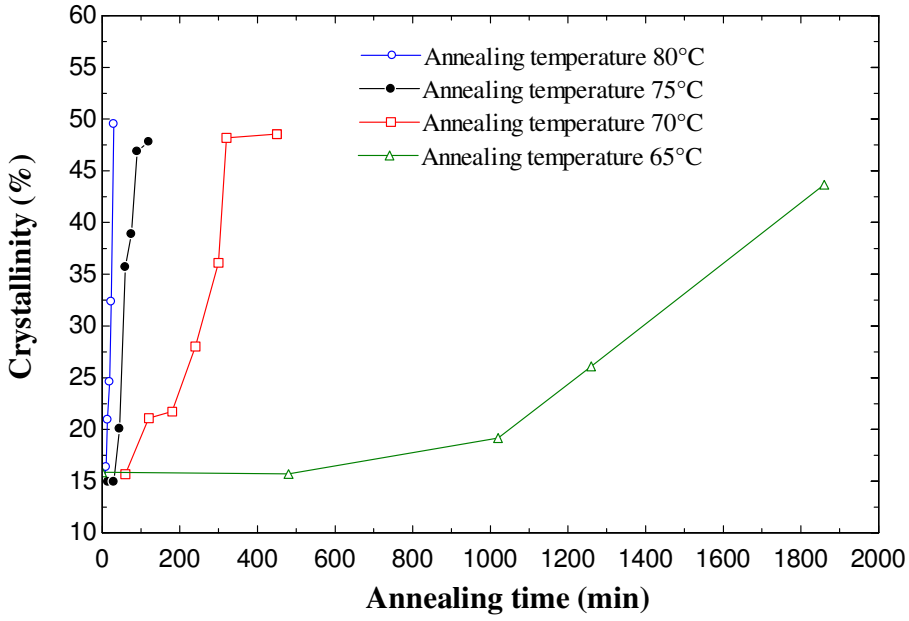

Figure 2.2 Degree of crystallinity versus annealing time at annealing temperatures of 65, 70, 75, and 80 ºC.

The log–log plot of the degree of crystallinity versus the annealing time at various temperatures from Figure 2.2 is shown in Figure 2.3. Note that the crystallinity vs. time plot shows the same slope at different annealing temperatures.

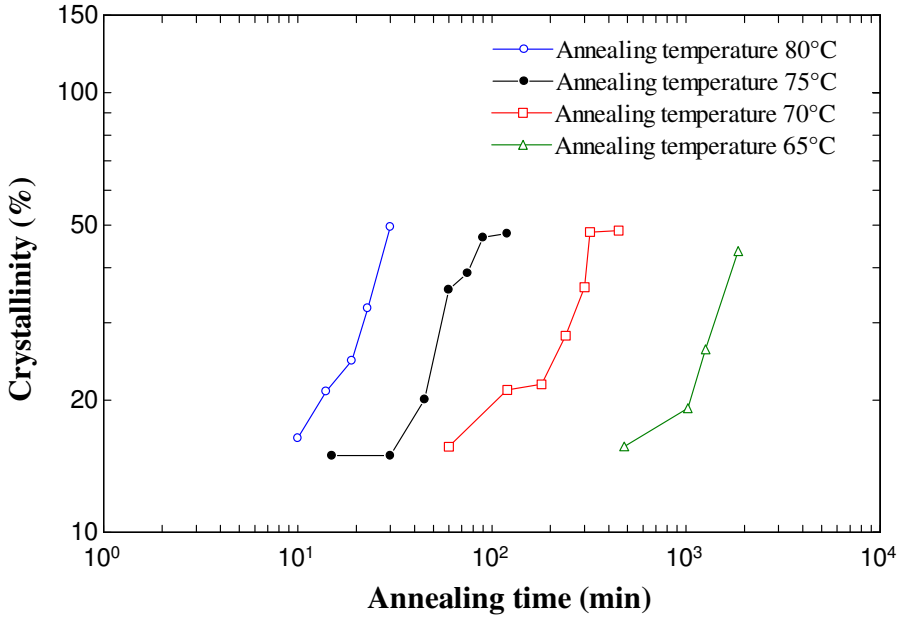

Figure 2.3 Log–log plot of the degree of crystallinity versus the annealing time at different annealing temperatures.

2.3.2 XRD Data

The XRD spectra of PLA molded and annealed specimens at 75 ºC for up to 2 hours are presented in Figure 2.4. At an annealing time of up to 45 minutes, the specimen data appeared mostly amorphous and only one broad halo with a maximum at 2θ ≈16º was observed with no presence of crystallinity peak(s) [10]. At an annealing time of 60 minutes, crystalline bands started to develop. As the annealing time increased, their intensities also increased and two bands at 2θ of around 16.2° and 18.6° were observed indicating a crystalline PLA matrix [1, 12]. These can be seen from the curves of annealing times at 60, 75, 90, and 120 minutes.

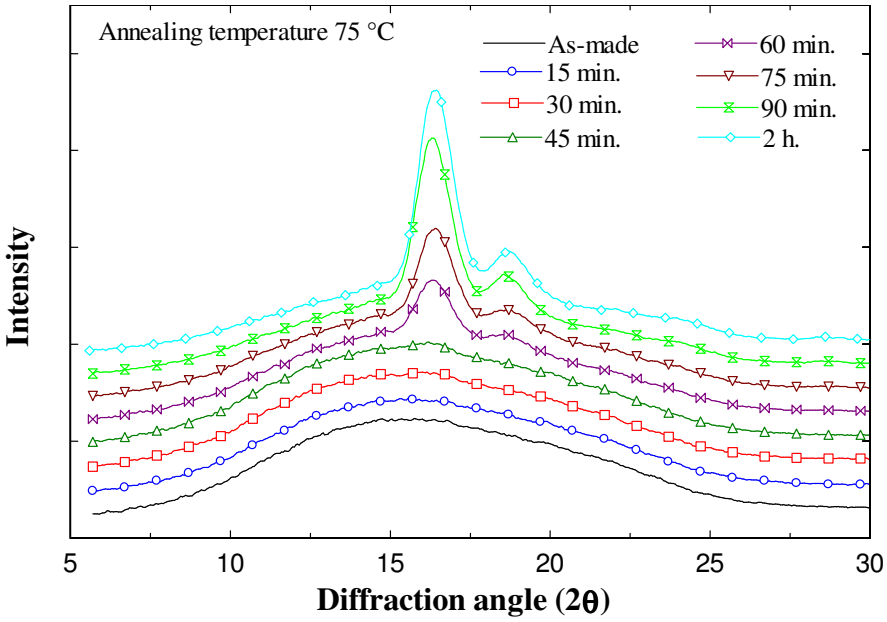

Figure 2.4 XRD spectra of annealed PLA specimens at different annealing times.

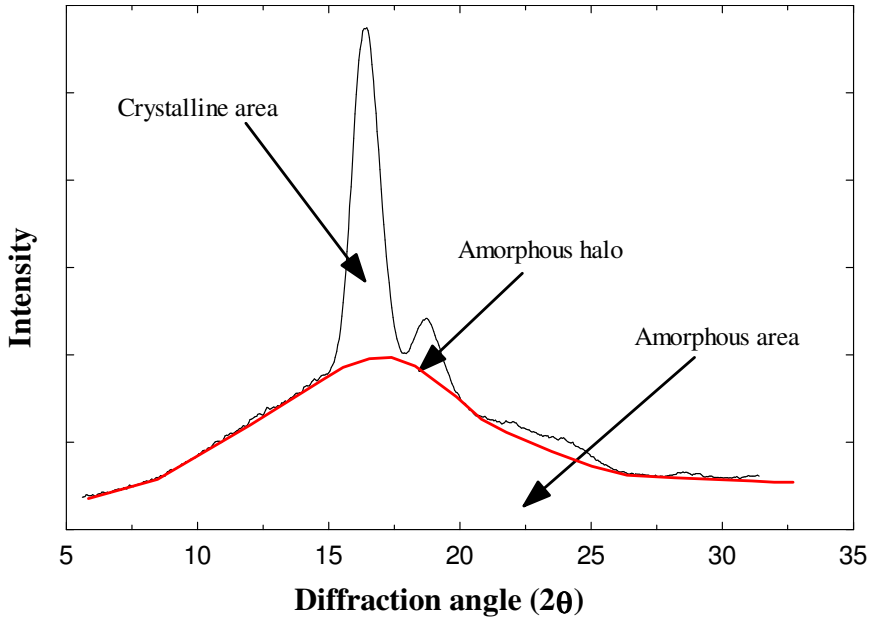

Figure 2.5 Intensity versus 2θ of XRD analyses of PLA at 75 ºC for 2 h.

To determine the crystallinity, it is critical to separate the crystalline peaks from the amorphous scattering region as illustrated in Figure 2.5. Powderx software was used to eliminate the amorphous background and smooth the curve [3]. The upper diffraction peak area and the total diffraction area over the 2θ diffraction angle between 10º and 30º were integrated. The degree of crystallinity was calculated directly using Eq. (2.3).

2.3.3 Crystallinity Results

The results in Figure 2.6 show the XRD and DSC measurements of crystallinity for PLA. It can be seen that the degree of crystallinity derived from the XRD was smaller than the values obtained by calorimetry. Note that the XRD reported a 0% degree of crystallinity for very short annealing times, while the DSC reported a value in excess of 14% for the same annealing times. This discrepancy might be due to the thermal approach of the DSC, which introduces heating (and thus potential crystallization) to the specimens as they are being tested [10]. Also, it can be difficult to resolve the cold crystallization and second endothermic peaks based on the DSC curve. On the other hand, XRD has been traditionally accepted as the direct technique for crystallinity measurement [6]. However, the crystallinity estimated XRD data relies on a deconvolution of the XRD spectra into an amorphous halo and the sum of the crystalline components, which can be very cumbersome [8]. Therefore, for the sole purpose of comparison, only DSC results for all specimens are presented. Nonetheless, both methods gave similar trends in terms of crystallinity.

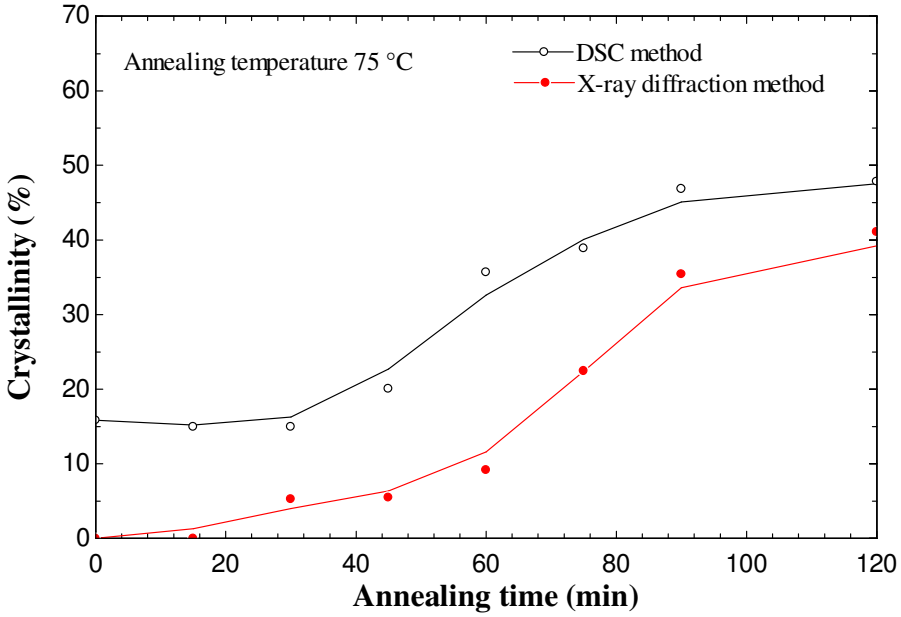

Figure 2.6 DSC and XRD data in terms of degree of crystallinity versus annealing time at an annealing temperature of 75 ºC.

2.3.4 Time–Temperature Superposition (TTS)

Given the respective effects of annealing time and temperature on the crystallinity of PLA and the fact that each curve in Figure 2.3 resembles each other, the time–temperature superposition technique was employed to construct the master curve. Namely, curves of the degree of crystallinity versus the log of the annealing time at a given temperature were shifted horizontally by a shift factor (a_T) to overlap with an adjacent curve at a reference annealing temperature. In this study, all curves at temperature higher than 65 ºC were shifted to the curve at 65 ºC, which serves as the reference annealing temperature since this annealing temperature was closest to the glass transition temperature (i.e., Figure 2.1). The time-temperature shift factor a_T is defined as:

$$a_T = \frac{t}{t'} \tag{2.5}$$

where *t* is the experimental time data, and *t'* is the reduced time. Figure 2.7 showed the master curve relative to curves at 65 ℃. The shift factor in this experiment was calculated and listed in Table 2.2.

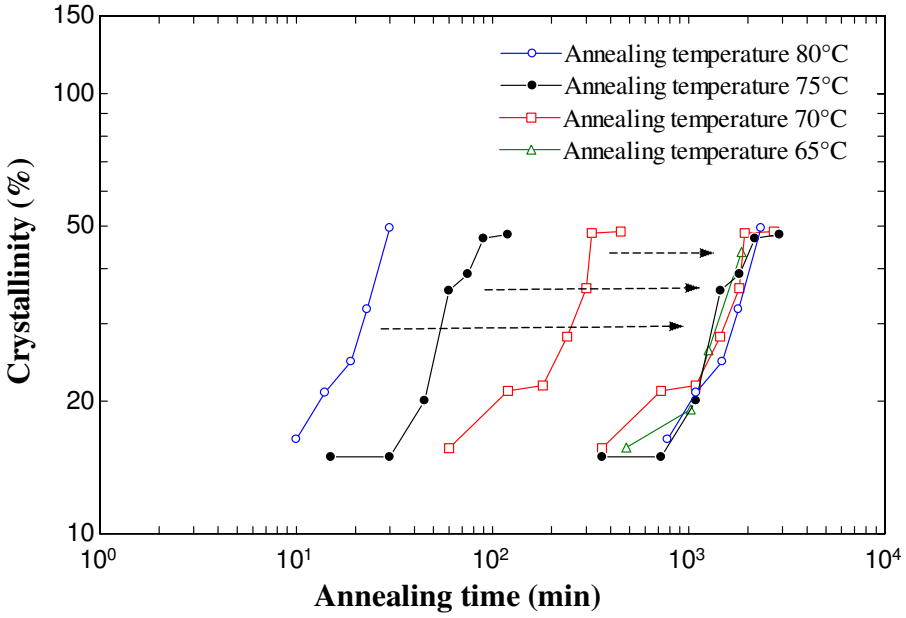

Figure 2.7 The master curve with respect to the 65 ℃ curve.

Table 2.2: Shift factor a_T and $\ln(a_T)$ for annealed PLA.

Temperature ℃ (K)	$\mathbf{a_T}$	**ln** ($\mathbf{a_T}$)
65 (338)	1	0
70 (343)	0.1661	-1.795
75 (348)	0.0413	-3.187
80 (353)	0.0128	-4.358

The empirical relationship between the time and temperature effects can be formulated via a mathematical relationship known as the Williams–Landel–Ferry Equation (WLF) equation [14-16]. This shifting equation is very useful if information is available for only one temperature

and information for other temperatures needs to be computed. The WLF equation, enunciated by William et al. [16-18] is given by

$$\log(a_T) = \frac{-c_1(T - T_{ref})}{c_2 + (T - T_{ref})} \tag{2.6}$$

where a_T is the horizontal shift factor for the corresponding temperature, T (K); T_{ref} is the reference temperature (K); and c_1 and c_2 are the empirical constants. In this study, T_g was chosen as the reference temperature.

The shift factor data, fitted to the WLF model by the least square fit method (nonlinear regression, MATLAB), yields the solid line curve in Figure 2.8. The estimated values of c_1 and c_2 are also indicated in the figure. The data closely follows the fitted curve and shows a curvature in accordance with the WLF equation. Note the excellent fit of the data (standard error 0.05).

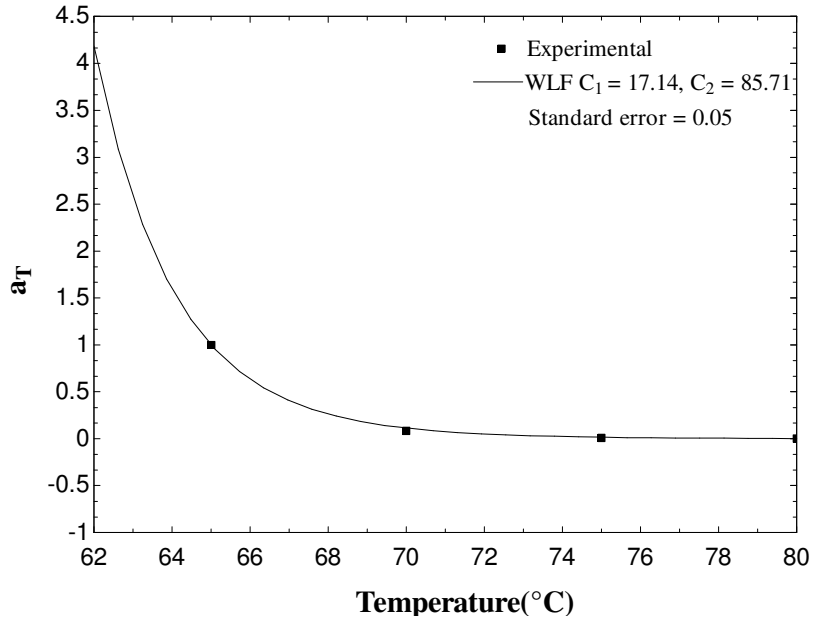

Figure 2.8 Shift parameter, a_T, versus temperature, T_{ref} = 65 ºC.

Additionally, by looking at the data in Table 2.2 it can be noted that a_T decreases rapidly with increasing temperature. This temperature dependence for annealing PLA suggested an exponential decrease of a_T with increasing temperature. Data from Table 2.2 are shown on an $\ln(a_T)$ versus 1/T plot and the result is illustrated in Figure 2.9. This figure shows a linear relationship between $\ln(a_T)$ and 1/T using linear regression through data point, with the square of sample correlation coefficient R^2 satisfying $R^2 > 0.98$.

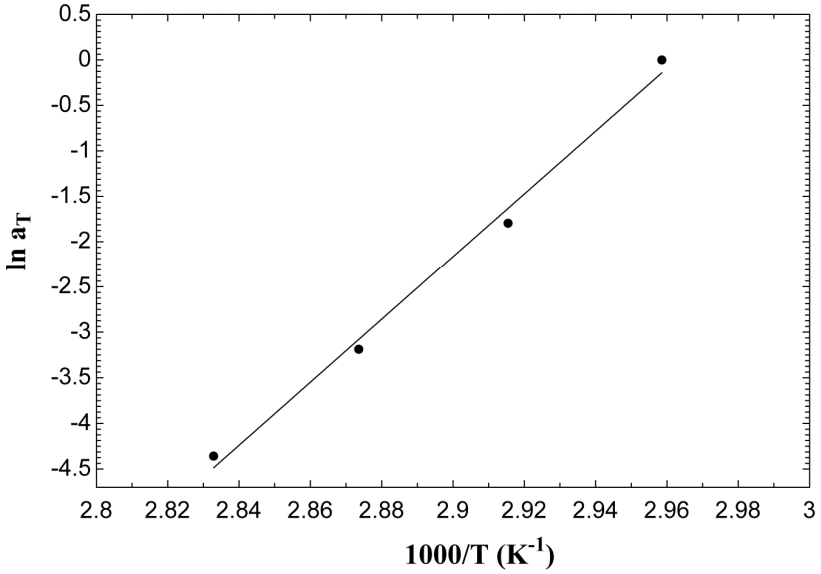

Figure 2.9 The dependence of logarithm of shift factor (a_T) on reciprocal temperature for annealed PLA. Linear fit through data points are given by the solid line.

The apparent linear dependence of $\ln a_T$ versus 1/T implies that shift factor (a_T) also satisfies the Arrhenius equation [19, 20], namely,

$$\ln(a_T) = \frac{E_a}{RT} - \ln A \qquad (2.7)$$

where A is the constant and E_a is the activation energy. This indicates the applicability of the Arrhenius equation to annealing PLA. The empirical constants A and E_a in Equation (7) were

then deduced from the slope and intercept of the best fitting line to the experimental data, with gas constant R = 0.001987 kcal K^{-1} mol^{-1}. The ln A and E_a thus determined are 102.3 and 0.06865 kcal mol^{-1}.

2.3.5 Heat Resistance Properties

Injection-molded and annealed parts were set as shown in Figure 2.10(a) and place in the oven at the temperature of 65 ℃ to observed the heat resistance and deformation of the specimens. Figure 2.10(b) shows that the as-molded PLA specimen (the first specimen), which had lowest degree of crystallinity, exhibited the maximum deformation at 65 ℃. Other annealed specimens showed very little or no deformation at all, suggesting a better heat resistant behavior resulting from the annealing treatment.

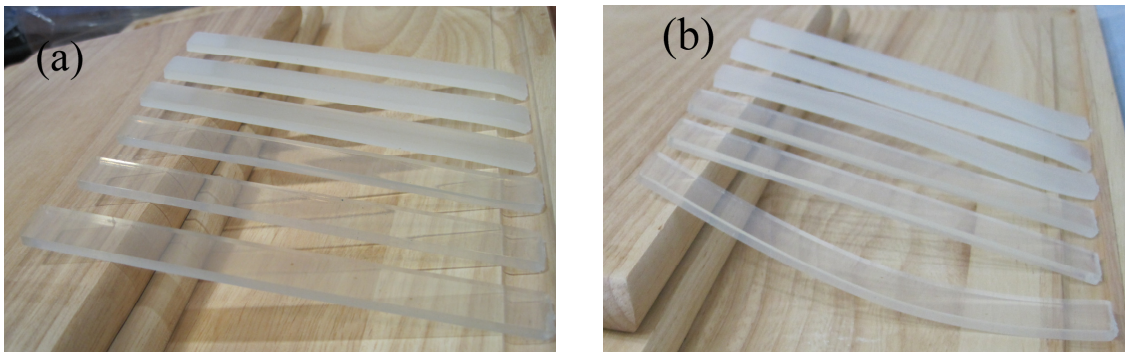

Figure 2.10 Heat resistance of as-made and annealed PLA. a) as-made and annealed PLA of different annealing times at an annealing temperature of 80 ℃, b) as-made and annealed PLA after placing them in an oven at 65 ℃ for 3 min.

2.3.6 Tensile Properties

Tensile tests (according to ASTM D638) were performed on as-molded and annealed PLA tensile bar specimens. Properties such as tensile modulus and tensile strength were measured as shown in Table 2.3; the representative stress–strain curves are depicted in Figures 2.11. Since the tensile properties at annealing temperatures of 70 and 75 ºC had the same trend to those annealing at 65 and 80 ºC, only two sets of data corresponding to 65 and 80 ºC are shown. As can be seen in Table 2.3 and Figure 2.11, the tensile strength of the annealed PLA blends was noticeably higher compared to that of as-molded specimens. At an annealing temperature of 80 ºC, the tensile strength for the as-molded PLA specimen and three annealed PLA specimens with 14, 23, and 30 min annealing times were found to be around 65.3, 71.7, 73.5, and 76.0 MPa, respectively, which account for a maximum 17% increase. The tensile modulus of fully annealed PLA specimen increased by a maximum of 6.4%. The same kind of trend was found for specimens annealed at 65 ºC for a much longer time. The tensile strength and modulus of fully annealed PLA specimen at an annealing temperature of 65 ºC were found to increase by around 26 and 13%, respectively. The different degrees of improvement might be due to the difference in crystalline morphology [21]; e.g., the size and density of the spherulites, which was confirmed by the morphology results shown in Figure 2.12 (discussed below). However, there was no significant difference in the strain-at-break, which was around 0.1 (10%).

Table 2.3 Mechanical properties of annealed PLA.

	Ultimate Tensile Strength (MPa)	Tensile Modulus (MPa)
PLA as-molded	65.3 ± 3.1	383.3 ± 12.2
Annealing temperature 65 ºC		
• Annealing 8 h	74.9 ± 4.1	411.5 ± 13.5
• Annealing 17 h	79.0 ± 3.3	413.6 ± 14.7
• Annealing 31 h	82.1 ± 4.7	433.8 ± 13.8
Annealing temperature 80 ºC		
• Annealing 10 min	71.7 ± 3.2	386.5 ± 13.0
• Annealing 23 min	73.5 ± 4.5	404.3 ± 13.2
• Annealing 30 min	76.0 ± 3.8	408.3 ± 14.4

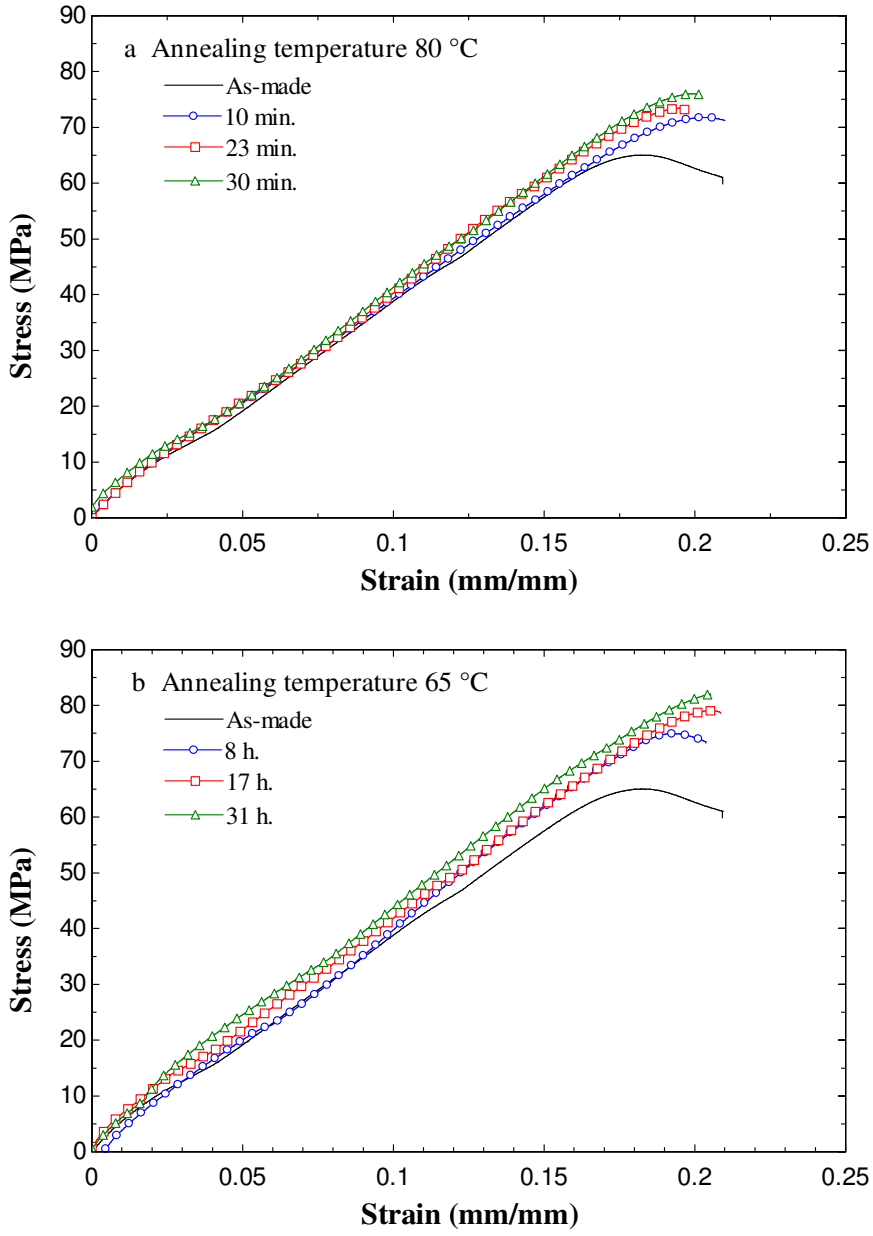

Figure 2.11 Tensile stress versus strain curve of the as-molded and annealed PLA. (a) annealing temperature 80 ºC. (b) annealing temperature 65 ºC.

The morphology of the annealed samples was investigated by polarized light microscopy (POM) as changes in thermal conditions can lead to changes in the morphology and the spherulite shape [22]. Fully annealed PLA tensile bars at annealing temperatures of 65 and 80°C

were microtomed from the center and the skin of the bars. Optical micrographs at annealing temperatures of 65 and 80 °C are shown in Figures 2.12 (a) and (b), respectively. The increase in spherulite size is clearly observed when the annealing temperature is raised from 65 to 80 ºC. Specimens with smaller spherulites are expected to exhibit a higher yield stress [21]. However, no difference in the morphology from the surface to the core was observed. This might be due to the small temperature gradient in the annealed samples.

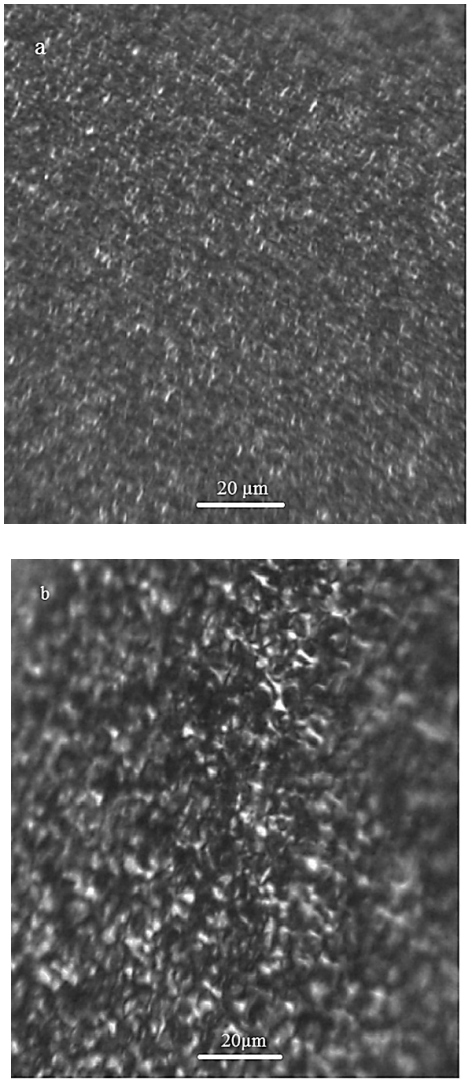

Figure 2.12 Optical micrographs of annealed injection molded PLA (a) sample was annealed at 65 ºC for 31 hr. (b) sample was annealed at 80 ºC for 30 min.

2.3.7 DMA Properties

DMA was used to study the viscoelastic properties of the as-molded and annealed PLA specimens. The effect of temperature on the storage modulus and glass transition temperatures in terms of tan δ of different annealing times at an annealing temperature of 80 ºC are depicted in Figures 2.13 and 2.14, respectively. Note that a similar trend was observed at different annealing temperatures (i.e., 65, 70, and 75 ºC). Figure 2.13 demonstrates that the PLA exhibited glassy state, glass-transition, and cold crystallization as the test temperature increased. The increase in annealing time (and thus the crystallinity) resulted in an increased storage modulus in the glassy state (–30 to 60 ºC). The storage moduli of all of the specimens later decreased between 60 and 80 ºC (cf. Figure 2.13) due to the glass transition temperature of the PLA [2, 23]. The decrease in modulus became more significant as the degree of crystallinity decreased. Furthermore, between 90 and 110 ºC, their moduli started to increase, which corresponded to the range of the cold crystallization temperature of the PLA (cf. Figure 2.1(d)). The increase in crystallinity during cold crystallization increased the rigidity of the specimen. In addition, the amorphous specimens had higher increases in crystallinity and modulus than their annealed, crystalline counterparts. Since the as-molded (mostly amorphous) PLA had the maximum cold crystallization temperature (cf. Figure 2.1(d)), the transitions in storage modulus also occurred at the highest temperature.

Figure 2.14 displays the tan δ curves. The area underneath the tan δ peak represents the damping ability of the material; that is, the material's ability to absorb and dissipate energy [24, 25]. As can be seen in Figure 2.14, the area underneath the tan δ peak of the PLA specimens decreased with an increasing degree of crystallinity. This indicates that the highly crystalline PLA specimens have less energy absorbing and damping ability than the amorphous specimens.

While the glass transition temperatures of the blends can be easily identified by the peaks in the tan δ curves in Figure 2.13, one can notice that the glass transition temperature from the DMA experiment was higher than that from the DSC experiment due to a slower heating rate. Furthermore, it can be observed from the figure that with the addition of annealing time (and thus the degree of crystallinity), the glass transition temperature (T_g) shifted to a slightly higher temperature, which can be attributed to the limitation of chain mobility within the polymer matrix [6].

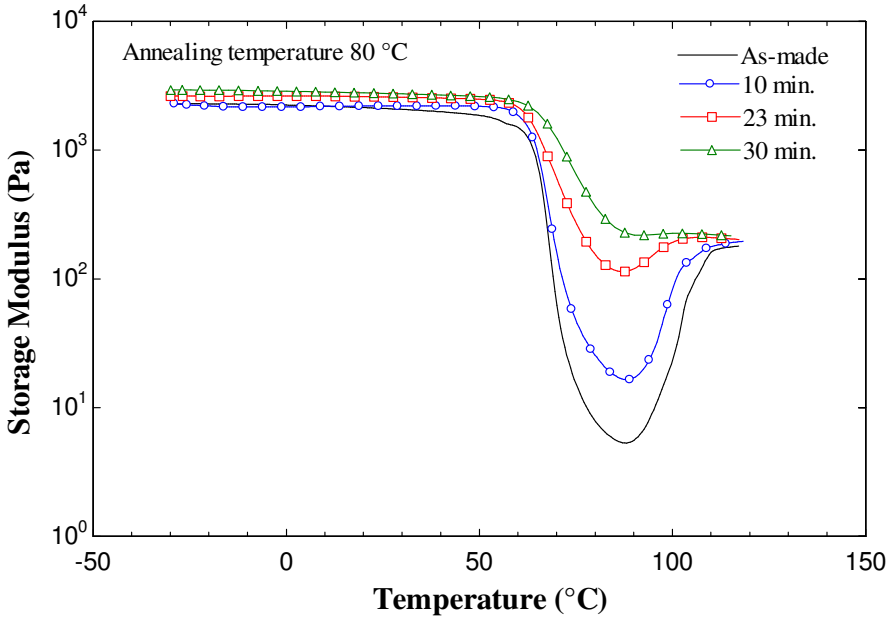

Figure 2.13 Storage moduli of the as-molded and annealed injection molded PLA as a function of temperature.

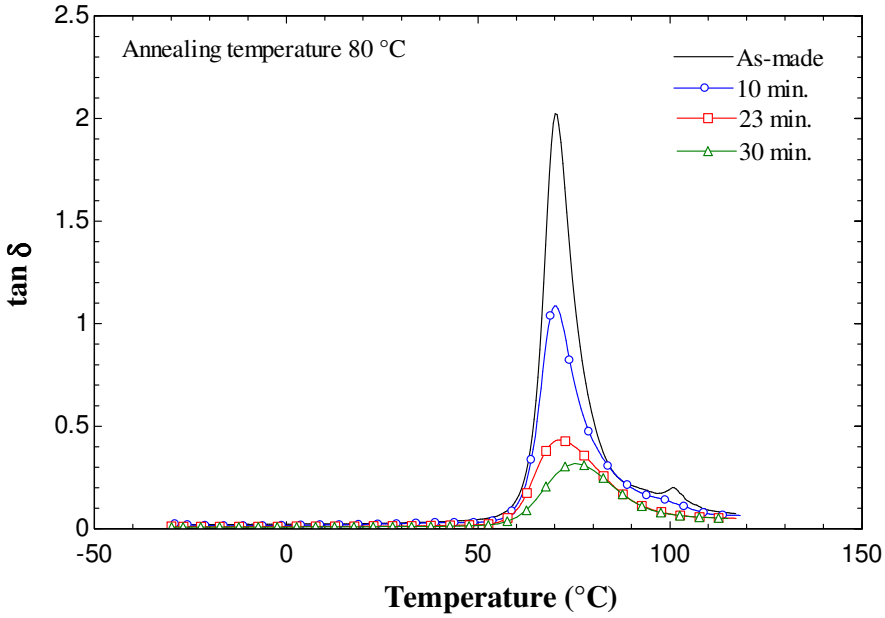

Figure 2.14 Tan δ curves of the as-molded and annealed injection molded PLA.

2.4 Conclusions

The effect of annealing time and temperature on the crystallinity and mechanical performance of injection molded PLA parts was studied. The degree of crystallinity depended upon time and temperature and was measured using XRD and DSC methods. The DSC method consistently gave a higher degree of crystallinity due to its inherent heating approach. The WLF and Arrhenius relationships between crystallinity as a function of annealing time and temperature were confirmed by this study, which provide useful guideline for heat treating molded PLA parts. Moreover, improvements in the mechanical performance and heat resistance of PLA were achieved by increasing the overall crystallinity.

2.5 References

1. Mathew AP, Oksman K, Sain M. The effect of morphology and chemical characteristics of cellulose reinforcements on the crystallinity of polylactic acid. Journal of Applied Polymer Science.101(1):300-310, 2006.
2. Yang S, Wu ZH, Yang W, Yang MB. Thermal and mechanical properties of chemical crosslinked polylactide (PLA). Polymer Testing.27(8):957-963, 2008.
3. Gupta B, Revagade N, Hilborn J. Poly (lactic acid) fiber: An overview. Progress in polymer science.32(4):455-482, 2007.
4. Harris AM, Lee EC. Improving mechanical performance of injection molded PLA by controlling crystallinity. Journal of Applied Polymer Science.107(4):2246-2255, 2008.
5. Osswald TA. International plastics handbook: the resource for plastics engineers: Hanser Verlag; 2006.
6. Srithep Y, Javadi A, Pilla S, et al. Processing and characterization of recycled poly (ethylene terephthalate) blends with chain extenders, thermoplastic elastomer, and/or poly (butylene adipate-co-terephthalate). Polymer Engineering & Science.51(6):1023-1032, 2011.
7. Gruver V, Showers, D., Kao, M. Y., & Klebanov, K. L. The determination of PET crystallinity by different analytical techniques. ANTEC : Conference proceedings.46, 2000.
8. Goto K, Nakano S, Kuriyama T. The effects of annealing on deformation and fracture behavior of injection molded PLA. Strength. Fract. Complex.4(3):185-188, 2006.
9. Nellis G, Klein S. Heat Transfer: Cambridge University Press; 2008.

10. Lee T, Boey F, Khor K. X ray diffraction analysis technique for determining the polymer crystallinity in a polyphenylene sulfide composite. Polymer composites.16(6):481-488, 1995.

11. D638-10 A. Standard test method for tensile properties of plastics: ASTM International, West Conshohocken, PA; 2010.

12. Wu TM, Wu CY. Biodegradable poly (lactic acid)/chitosan-modified montmorillonite nanocomposites: Preparation and characterization. Polymer degradation and stability.91(9):2198-2204, 2006.

13. Dong C. PowderX: Windows-95-based program for powder X-ray diffraction data processing. Journal of Applied Crystallography.32(4):838-838, 1999.

14. Vaidyanathan TK, Vaidyanathan J, Cherian Z. Extended creep behavior of dental composites using time-temperature superposition principle* 1. Dental Materials.19(1):46-53, 2003.

15. Deng M, Latour RA, Ogale AA, Shalaby SW. Study of creep behavior of ultra-high-molecular-weight polyethylene systems. Journal of Biomedical Materials Research.40(2):214-223, 1998.

16. Matsumoto D. Time temperature superposition and physical aging in amorphous polymers. Polymer Engineering & Science.28(20):1313-1317, 1988.

17. Tamrakar S, Lopez-Anido RA, Kiziltas A, Gardner DJ. Time and temperature dependent response of a wood-polypropylene composite. Composites Part A: Applied Science and Manufacturing. 2011.

18. Tajvidi M, Falk RH, Hermanson JC. Time–temperature superposition principle applied to a kenaf-fiber/high-density polyethylene composite. Journal of Applied Polymer Science.97(5):1995-2004, 2005.

19. Ferry JD. Viscoelastic properties of polymers: John Wiley & Sons Inc; 1980.

20. Djoković V, Kostoski D, Dramićanin M. Viscoelastic behavior of semicrystalline polymers at elevated temperatures on the basis of a two-process model for stress relaxation. J. Polym. Sci. Pol. Phys.38(24):3239-3246, 2000.

21. Kamal MR, Kalyon D, Dealy J. An integrated experimental study of the injection molding behavior of some polyethylene resins. Polymer Engineering & Science.20(17):1117-1125, 1980.

22. Degirmenbasi N, Ozkan S, Kalyon DM, Yu X. Surface patterning of poly (L-lactide) upon melt processing: In vitro culturing of fibroblasts and osteoblasts on surfaces ranging from highly crystalline with spherulitic protrusions to amorphous with nanoscale indentations. Journal of Biomedical Materials Research.88(1):94-104, 2009.

23. Pilla S, Gong S, O'Neill E, Rowell RM, Krzysik AM. Polylactide pine wood flour composites. Polymer Engineering & Science.48(3):578-587, 2008.

24. Javadi A, Srithep Y, Lee J, et al. Processing and characterization of solid and microcellular PHBV/PBAT blend and its RWF/nanoclay composites. Composites Part A: Applied Science and Manufacturing.41(8):982-990, 2010.

25. Srithep Y, Turng LS, Sabo R, Clemons C. Nanofibrillated cellulose (NFC) reinforced polyvinyl alcohol (PVOH) nanocomposites: properties, solubility of carbon dioxide, and foaming. Cellulose.1-15, 2012.

CHAPTER 3

Nanofibrillated Cellulose (NFC) Reinforced Polyvinyl Alcohol (PVOH) Nanocomposites: Properties, Solubility of Carbon Dioxide, and Foaming

3.1 Introduction

In recent years, environmental concerns have led to an increased interest in natural fibers and biodegradable polymers. At the same time, new technologies originating from the fields of nanotechnology and nanocomposites have led to opportunities in many areas, including materials from forest products [1]. Cellulose microfibrils (MFs), which are ordered uniquely in each of the cell wall layers of wood, are tightly bound by multiple hydrogen bonds. Mechanical homogenization or shearing of aqueous suspensions of cellulose has been used to break many of the bonds, often after chemical or enzymatic pretreatment, resulting in microfibrillated and even nanofibrillated cellulose (NFC) if sufficient energy is applied [2-5].

NFC is gaining attention as a reinforcing filler in thermoplastic matrices due to its numerous advantages, which include low density, renewability, high specific properties, biodegradability, gas barrier properties, and unlimited availability [6-8]. Despite these attractive properties, the processing temperature of these composites is restricted to about 200 °C due to NFC degradation beyond this temperature, thus restricting the type of matrix that can be used. For instance, polycarbonate (PC) and polyamide (PA) are typically processed at above 240°C [9,10].

In this study, polyvinyl alcohol (PVOH), a biodegradable, water-soluble polymer, was chosen as a matrix for cellulose-reinforced nanocomposites since NFC production usually yields an aqueous gel. Moreover, both PVOH and NFC are known for their good gas barrier properties [11-14]. Low polarity gas molecules, such as oxygen and carbon dioxide, exhibit only weak interactions with the highly polar hydroxyl groups in PVOH, resulting in its superior gas barrier properties [15]. When there are no pores to allow for gas flow through a material, gas permeability will depend on the dissolution of the gas and its rate of diffusion in the particular material [11]. However, no study has investigated the sorption of CO_2 in PVOH and PVOH/NFC nanocomposites. Therefore, we measured the solubility of CO_2 in PVOH and PVOH/NFC nanocomposites, as well as its foaming behavior.

Polymeric foams find application as materials for thermal and acoustic insulation, energy dissipation, shock protection, packing, etc. [16]. Due to their small cell size and high cell density, polymeric foams are light weight and offer better thermal insulation compared to solid materials. This study also carried out batch foaming experiments to investigate the influence of NFC on cell size and cell density using CO_2 and/or water as the physical foaming agents.

3.2 Experiments

3.2.1 Materials

NFC was prepared at the U.S. Forest Service, Forest Products Laboratory (Madison, WI) according to a procedure described by Saito and Isogai [17]. In particular, fully bleached Kraft eucalyptus fibers were oxidized with sodium hypochlorite using tetramethylpiperidine-1-oxy radical (TEMPO) sodium bromide as a catalyst. The TEMPO-mediated oxidation was carried out

at a pH of 10 at 25 °C for 3 hours. The fibers were then thoroughly washed and refined in a disk refiner with a gap of approximately 200 μm. The coarse fibers were separated by centrifuging at a force of 12,000 G, and the nanofiber dispersion was concentrated to 1% using ultrafiltration. A final clarification step was performed in which the nanofiber dispersion was passed once through an M-110EH-30 microfluidizer (Microfluidics, Newton, MA) with 200 μm and 87 μm chambers in series.

Partially hydrolyzed (87 to 89%) PVOH, Celvol 502®, was purchased from Celanese Chemicals, Ltd (Dallas, TX). It had a weight-average molecular weight (M_w) in the range of 13,000 to 23,000 and a degree of polymerization of 150 to 300.

3.2.2 Processing

The NFC gel was diluted with deionized (DI) water. After the NFC was thoroughly dispersed by magnetic stirring for 30 minutes, water-soluble PVOH was added, and stirring continued for 2 hours on a hotplate at 60 ºC to dissolve the PVOH, thus enabling the polymer to mix with the cellulose. PVOH solutions of 0, 2.5, 5, and 10 wt% NFC content were prepared and the resultant solutions appeared to be fully transparent. Then, the mixtures were cast in Petri dishes with a diameter of 90 mm and dried at room temperature (about 25 °C) and atmospheric conditions for seven days. Final film thicknesses were approximately 0.8 mm. Films were then stored at 90% humidity and 80 °C to equilibrate the moisture content in all films. Prior to mechanical and thermal testing, some of the specimens underwent additional conditioning to remove any extra moisture.

A transmission electron microscope (TEM, LEO 912) was used to characterize the dispersion of NFC. For dilute NFC–PVOH solutions, a drop was deposited on a carbon-coated TEM grid and

allowed to dry prior to imaging. For TEM imaging of nanocomposites, PVOH specimens containing 10% NFC were cut into 50 to 70 nm slices via an ultra-microtome at room temperature. Before the sections became clustered, a tweezers was used to separate them and TEM grids were placed on the slices for imaging. The TEM was operated at 120 kV at room temperature.

3.2.3 Tensile Testing

Type V tensile specimens (ASTM D638 [18]) were punched from films conditioned at 90% humidity using a cutting die. Prior to testing, samples were stored for 4 days in the tensile testing room, which was conditioned at 50% humidity at 25 ºC. The static tensile modulus, strength, and strain-at-break were measured on an Instron 5865. Tensile testing was performed on all specimens using an initial load of 2 N and a constant crosshead speed of 10 mm/min.

The experimental data obtained were compared with three theoretical models to predict the Young's modulus of the composite materials. The first model used the classical Rule of Mixtures approach where the Young's Modulus was calculated according to Eq. (1). The other models were the Mean Field approach of Halpin–Kardos (modified rule of mixture), as shown in Eqn. (2), and the Percolation approach, as shown in Eqn. (3) [19,20].

$$E = E_r X_r + E_m X_m \tag{3.1}$$

$$E^n = E_r^n X_r + E_r^n X_m \tag{3.2}$$

Davies suggested that the constant, *n,* be set to 1/5 based on theoretical analyses [19,21,22],

$$E = \frac{(1-2\psi + X_r)E_m E_r + (1-X_r)\psi E_r^2}{(1-X_r)E_r + (X_r - \psi)E_m} \tag{3.3}$$

where E is the nanocomposite modulus, E_r is the reinforcement modulus (which was assumed to be the same as that of a dried NFC film prepared by evaporating water from the NFC suspension), E_m is the matrix modulus, X_r is the fiber volume fraction, and X_m is the matrix volume fraction. The percolation volume fraction, ψ , is given by

$$\psi = \left(\frac{X_r - X_c}{1 - X_c} \right)^b \tag{3.4}$$

where X_c is a percolation threshold (in this work it was assumed to be 5% based on the results of Bulota et al. [19]) and b is the critical percolation exponent which is equal to 0.4 for a three-dimensional system [6].

3.2.4 Differential Scanning Calorimetry (DSC)

Differential scanning calorimetry (DSC) was performed on a DSC Q20 (TA Instruments). The specimens used for DSC characterization were taken from the 90% humidity room to a 30% humidity room for 4 days prior to DSC testing to reduce the moisture content in the samples. Specimens of 6 to 8 mg were placed in aluminum sample pans and heated from 30 to 205 °C at a 10 °C/min heating rate and held at 205 °C for 2 min to eliminate any prior thermal history yet minimize degradation. Specimens were then cooled at 10 °C/min to 30 °C. The specimens were then reheated to 205 °C and cooled down to room temperature using the same temperature, holding time, and cooling rates. The crystallization temperature (T_c) was determined from the DSC cooling curves.

3.2.5 Thermogravimetric Analysis (TGA)

Samples used for thermogravimetric analysis (TGA) were dried at 90 °C for 2 days. TGA was performed using a TGA Q50 (TA Instruments) from 25 to 600 °C at a heating rate of 10 °C/min. Approximately 10 mg of neat PVOH, neat NFC, or nanocomposites of various NFC contents, were used for each test. The loss of weight was recorded and normalized against the initial weight.

3.2.6 Dynamic Mechanical Analysis (DMA)

Dynamic mechanical analysis (DMA) measurements were performed on a DMA Q800 (TA Instruments) in single cantilever mode. The specimens from the 90% humidity room were cut to approximately 35.2 by 12.7 by 0.8 mm and then kept in the testing room (50% humidity at 25 ºC) for 4 days before the test. During the DMA test, the specimens were heated at a rate of 3 °C/min from –20 ºC to 150 ºC with a frequency of 1 Hz and an amplitude of 50 µm. To study the effect of moisture content on the dynamic mechanical properties, additional specimens were dried in an oven at 90 ºC for 2 days prior to DMA testing for comparison with the equilibrated specimens. The DMA testing took around one hour. The weight gain due to moisture of the dried samples in 50% humidity at room temperature was around 0.02%, which was insignificant.

3.2.7 Sorption Measurement

The main purpose of the sorption experiments was to establish the amount of CO_2 absorbed in the PVOH and PVOH/NFC nanocomposites. The original weights of these samples were measured using a digital balance readable to 0.0001 g. Sorption of CO_2 was facilitated by placing the specimens in a high-pressure vessel under a CO_2 gas pressure of 5.52 MPa (800 psi)

at room temperature for one day. No further weight gain was detected in samples placed in the pressure vessel for more than one day, suggesting that it had reached steady state. Afterward, the vessel was depressurized and the CO_2-absorbed samples were removed from the pressure vessel and placed on a balance to record the CO_2 sorption in the pressure chamber and its desorption over time at atmospheric pressure. The process of depressurization and removing the samples from the pressure chamber and weighing them took around 40 s. Samples were kept in an oil bath on the scale to reduce weight gain or loss in the sample due to moisture.

3.2.8 Foam Preparation

To study the foaming behavior and the effect of moisture on foaming (i.e., using the absorbed water as the plasticizer and/or physical blowing agent), neat PVOH and its nanocomposites with different moisture contents were foamed in a batch process. The samples were either: (1) pre-conditioned at 90% humidity for two days, or (2) dried in an oven at 90 ºC for two days.

In the batch foaming process used in this study, ASTM D638 Type V tensile test bars made of neat resin and nanocomposites were punched from the films and then placed in a pressure vessel filled with CO_2 at 5.52 MPa (800 psi) for one day, allowing ample time for CO_2 to diffuse into the samples. When the specimens were removed from the pressure vessel and brought to atmospheric pressure, supersaturated specimens—which were thermodynamically unstable due to the excessive gas dissolved in the polymer—were produced. This resulted in the nucleation and growth of gas microcells. After two hours at room temperature, the specimens were placed into a hot oil bath at 135 ºC for 10 s to vaporize the moisture inside of the specimens. If cells were not first allowed to nucleate and begin to grow for this two-hour time

period, placement into a hot oil bath caused severe cracking of the matrix due to the amount of vapor formed.

3.2.9 Scanning Electron Microscopy (SEM)

The cryogenically fractured surfaces were examined using an SEM (LEO 1530) operated at 3 kV. The samples were frozen in liquid nitrogen and then fractured using two small pliers. All specimens were sputter-coated with a thin layer of gold (~20 nm) prior to examination.

3.2.10 Characterization of Foams

The densities of the samples were measured by a toluene displacement technique (ASTM D792 [23]). The density of toluene at 20 ºC is 868 g/cm^3 [24]. The weights of unfoamed and foamed samples were measured in air (M_a) and toluene (M_T), and the density was determined by:

$$\text{Density} = 868\left(\frac{M_a}{M_T}\right) \tag{3.5}$$

The reported density is the average of five replicates.

The average cell size and cell density of the PVOH nanocomposites was quantitatively analyzed using an image analysis tool (UTHSCSA ImageTool). The cell density was calculated using the following formula [25],

$$\text{Cell density} = \left(\frac{N}{L^2}\right)^{3/2} M \tag{3.6}$$

where N is the number of cells, L is the linear length of the area, and M is the unit conversion factor resulting in the number of cells per cm^3. For cells of irregular shape, the cell size was taken to be the largest opening dimension.

3.3 Results and Discussions

3.3.1 Dispersion of NFC in PVOH

Figures 3.1 (a) and (b) show TEM images of a dilute NFC–PVOH solution dried on carbon-coated grids and the ultra-microtomed specimens, respectively. The TEM images illustrate that NFC is an interconnected web with fibrils having a diameter in the range of 10 to 50 nm. When dispersed in water, NFC forms a very stable suspension due to the interfibrillar repulsive forces created during the TEMPO pre-treatment. Based on the TEM images, it was concluded that NFC dispersed well in a PVOH water solution. Further evidence for the uniformity of the dispersion was the full transparency of the resulting films as shown in Figure 3.2 [26].

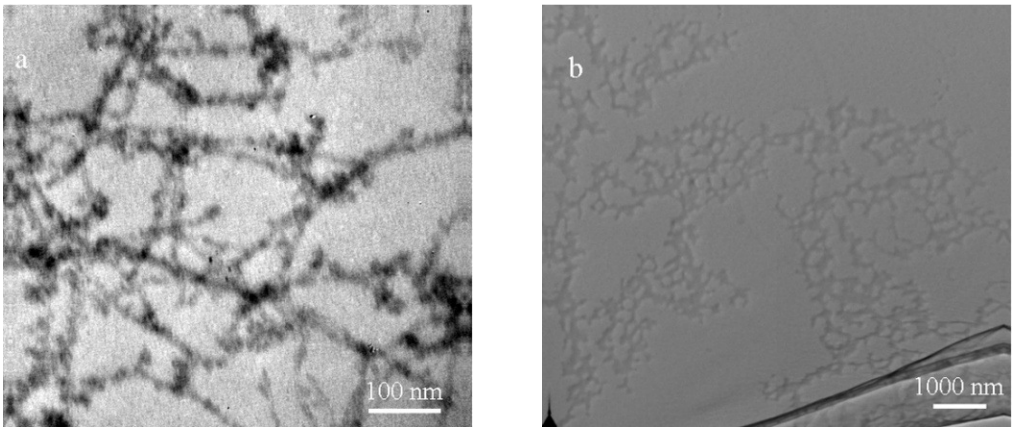

Figure 3.1 TEM images for nanocomposites. (a) Sample was obtained by evaporating an NFC and PVOH water solution on a carbon-coated grid. (b) Sample was obtained by cutting via ultra-microtome. Scale bars are 100 nm and 1,000 nm for (a) and (b), respectively

Figure 3.2 Transparency (from left to right) of neat PVOH and PVOH/NFC nanocomposites with 2.5%, 5%, and 10% NFC, respectively.

3.3.2 Tensile Properties

Tensile tests were performed on specimens punched from the cast films. Representative stress–strain curves are featured in Figure 3.3. The addition of NFC yielded stronger and stiffer composites but toughness (measured as work of fracture) was reduced in comparison to neat PVOH samples. The strain at break for PVOH reinforced with 0%, 2.5%, 5%, and 10% NFC were found to be 4.4, 3.2, 2.6, and 0.6, respectively. The lower strain at break of PVOH/NFC nanocomposites was probably due to the PVOH itself reaching its maximum tensile strength. Neat PVOH had the lowest value of ultimate tensile strength and tensile modulus, which were 16.1 and 25.5 MPa, respectively. As the amount of NFC increased, the ultimate tensile strength and tensile modulus increased.

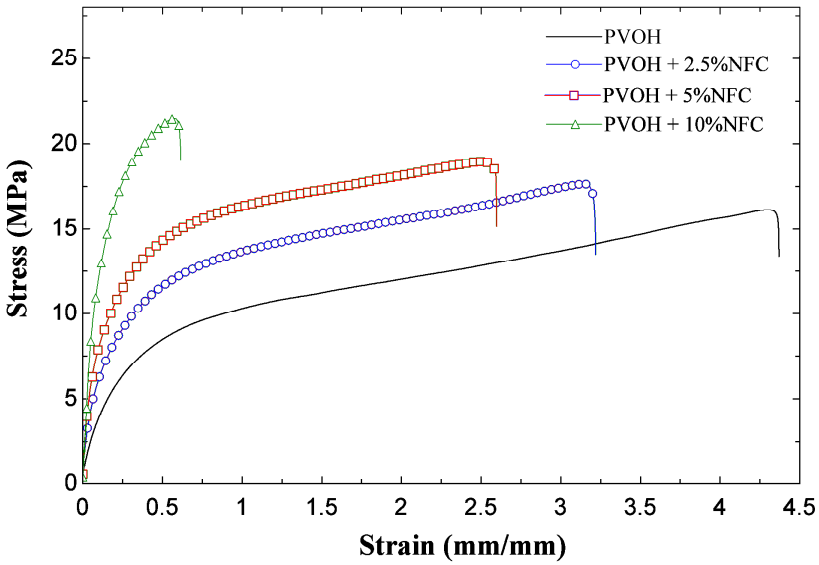

Figure 3.3 Tensile stress versus strain curve for the NFC and PVOH nanocomposites.

Experimental data in this work were compared with theoretical models. For modeling mechanical properties of the composites, the tensile modulus of 100% NFC was assumed to be that of a dried NFC film prepared by evaporating water from an NFC suspension. The NFC film was also punched out and tested using the same tensile testing conditions as the PVOH/NFC nanocomposites. The strain at break, tensile modulus, and ultimate tensile strength of dried NFC were 0.06, 3730 MPa, and 141.5 MPa, respectively. A comparison of tensile moduli is presented in Figure 3.4. Theoretical modeling based on the modified rule of mixtures and percolation theory was in good agreement with experimental data. The rule of mixtures seemed to overestimate reinforcement phenomena. This could be due to the fact that the models assumed unidirectional and uniform fiber orientation and distribution in addition to a perfect bond between the matrix and the fiber [19,27].

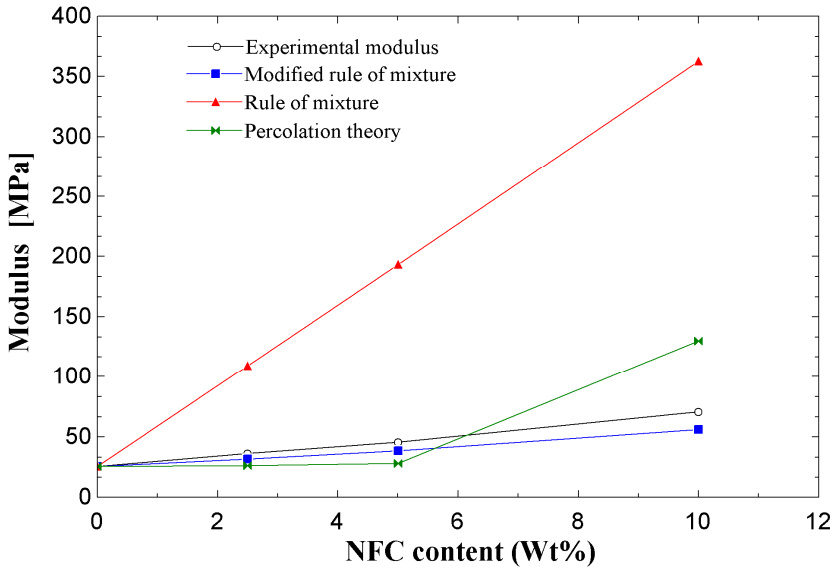

Figure 3.4 Comparison of experimental data to models.

3.3.3 Thermal Properties

PVOH is a semicrystalline polymer in which high physical inter-chain and intra-chain interactions exist due to hydrogen bonding between hydroxyl groups. The introduction of nanosized cellulose fibers with hydroxyl groups alters the intra-molecular and inter-molecular interactions of the PVOH chains. This may affect both the crystallization behavior and the physical structure of PVOH, resulting in variations in properties of nanocomposite samples [28,29].

Because the PVOH degrades near its melting temperature [8,11], three heating and two cooling cycles were performed so that useful comparisons could be made. Results from the initial heating cycle in DSC experiments were discarded because they included the latent heat from the water absorption in the samples.

Degradation

Figures 3.5 and 3.6 show the second and third heating cycles, as well as the first and second cooling cycles, of PVOH and PVOH/NFC nanocomposites. As shown in Figure 3.5, the endothermic peak, which occurred between 190 ºC and 200 ºC, is referred to as the melting peak of PVOH. An exothermic peak, which occurred between 160 to 180 ºC, was observed in all specimens and corresponds to the crystallization of PVOH (cf. Figure 3.6). Note that the additional thermal scanning cycles caused a decrease in the melting and crystallization temperatures as well as the heat, suggesting sample degradation [28,30] . The magnitude of the shift increased with increasing NFC concentration, indicating that NFC might cause degradation of the polymer, likely through residual moisture in NFC. This degradation was further confirmed by TGA results.

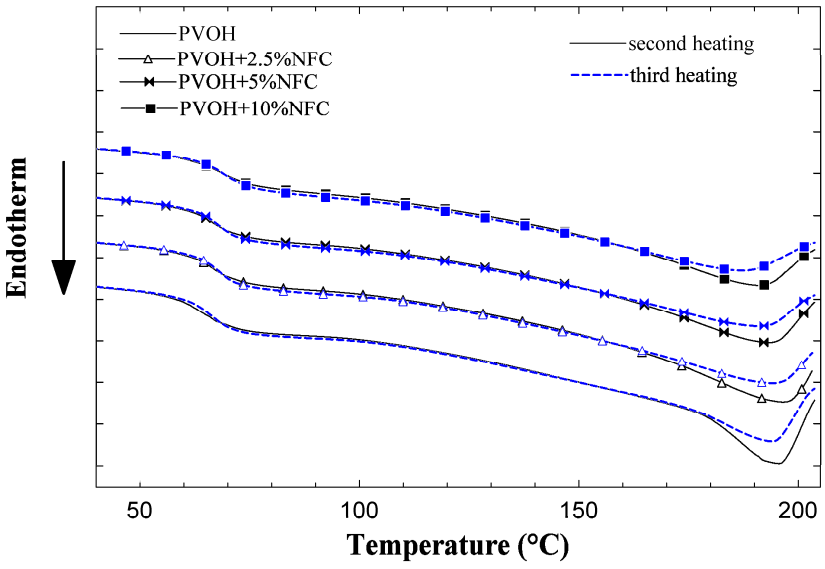

Figure 3.5 Comparison of the melting endotherms during the second (solid line) and third (dashed line) heating scans of PVOH and its nanocomposites with NFC.

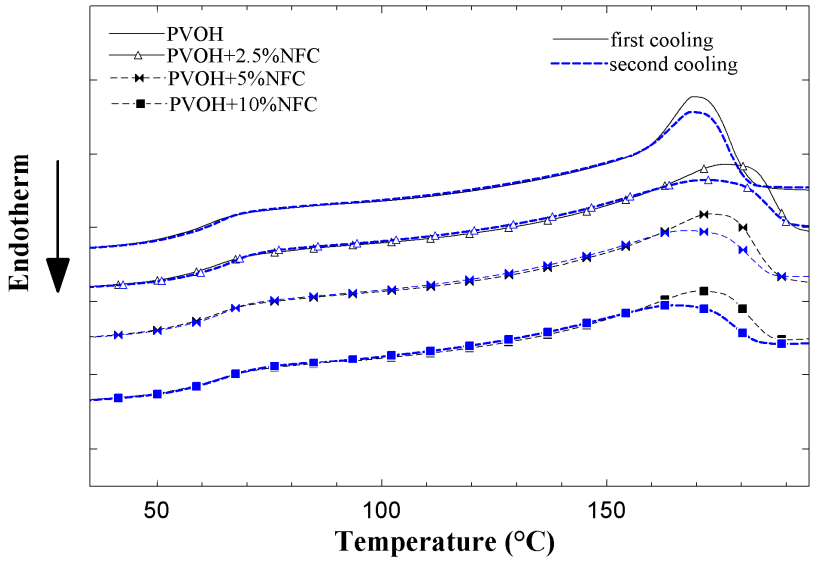

Figure 3.6 Comparison of the crystallization exotherms during the first (solid line) and second (dashed line) cooling scans of PVOH and its nanocomposites with NFC.

Nucleating Effect

Table 3.1 provides clear evidence that NFC also serves as a nucleating agent as the crystallization temperature (T_c) is higher with the addition of NFC. With the addition of 2.5% NFC, the crystallization peak of PVOH is roughly 5 °C higher. Furthermore, the crystallization regime was prolonged as compared to neat PVOH. With further addition of NFC, however, the crystallization peak temperature decreased. The initial increase and then decrease of crystallization temperatures with increasing NFC content could be the result of several competing factors, including enhanced nucleation for crystallization, material degradation due to residual moisture in NFC, and/or physical interactions between the polymer and reinforcements that restrict the segmental mobility of the polymer chains. Similar effects by other nanosized materials on the crystallization and degradation of PVOH have been reported previously [28,29].

Table 3.1 DSC results based on the second heating and first cooling scan.

Samples	T_g (ºC)	T_m (ºC)	ΔH (J/g)	X_c (%)	T_c (ºC)
PVOH	66.2	195.4	12.0	8.0	168.1
PVOH+2.5%NFC	66.3	196.8	12.1	8.2	174.8
PVOH+5%NFC	66.6	193.1	11.2	7.8	171.2
PVOH+10%NFC	68.8	190.9	10.5	7.7	168.2

Furthermore, the enthalpy (ΔH), percent crystallinity (χ_c), and melting temperatures (T_m) calculated from the second cooling scan are shown in Table 3.1. The degree of crystallinity of PVOH was calculated based on the following equation,

$$\chi_c = \frac{\Delta H_m}{w \Delta H_m^o} \tag{3.7}$$

where w is the weight fraction of PVOH in the composites, ΔH_m is the measured heat of fusion, and ΔH_m^o is the heat of fusion of a 100% crystalline PVOH which has a value of 150 J/g [31]. As shown in Table 3.1, and similar to the change in crystallization temperature, the degree of crystallinity of PVOH increased slightly with a small addition of NFC, and then decreased. This increase in crystallinity is possibly due to the nucleating effect of the nanosized NFC fibers. The same phenomena were observed for tunicin whisker-reinforced plasticized starch [32] and carbon nanotube-reinforced PVOH composites [33]. In addition, the shoulders in the DSC thermograms in Figure 3.5 indicate that the glass transition temperatures of PVOH and PVOH/NFC nanocomposite samples were between 50 and 80 ºC.

3.3.4 Thermal Stability

The thermal stability of the neat PVOH and PVOH/NFC nanocomposite samples were examined using TGA. TGA results shown in Figure 3.7 confirm that adding NFC leads to increased degradation. The onset degradation temperatures of the PVOH/NFC nanocomposites decreased with the addition of NFC.

As shown in Figure 3.7, there was an initial and slow weight loss of NFC until around 200 ºC, which might be attributed to both the loss of residual moisture in the NFC as well as the slow degradation of NFC. The most pronounced degradation began at approximately 200 ºC, which was lower than the maximum temperature of 205 ºC used in the heating scans during the DSC analysis. This supports the findings that the material might have degraded at the end of the first DSC heating scan (cf. Figure 3.5). There was an approximate 30% char yield at temperatures above 500 ºC.

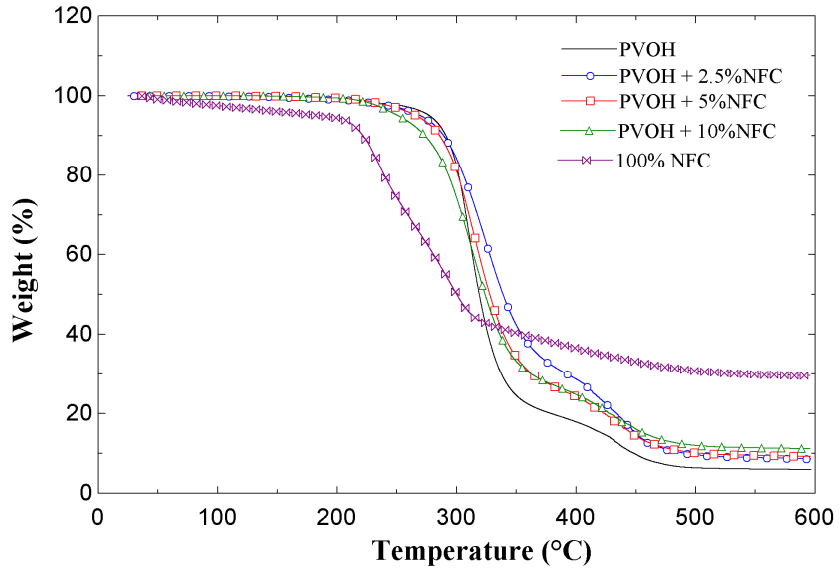

Figure 3.7 TGA curves for the PVOH/NFC nanocomposite samples.

3.3.5 Dynamic Mechanical Properties (DMA)

Since PVOH is a hydrophilic polymer, its properties were strongly affected by the presence of moisture in the samples [19,34]. For the study on the effects of moisture content in PVOH and NFC on the mechanical properties, two sets of specimens were prepared. The first set was removed from the 90% humidity room and reconditioned for 4 days at 50% humidity and 25 ºC prior to testing. To further reduce the moisture content within the specimens, the other set of samples was dried at 90 ºC for 2 days prior to the DMA test. Figure 3.8 shows the weight of PVOH/NFC nanocomposites, which were dried at 90 ºC, from the 90% humidity room as a function of time. The actual moisture contents of the samples from the 90% and 50% humidity rooms were found to be around 21% and 7.5%, respectively.

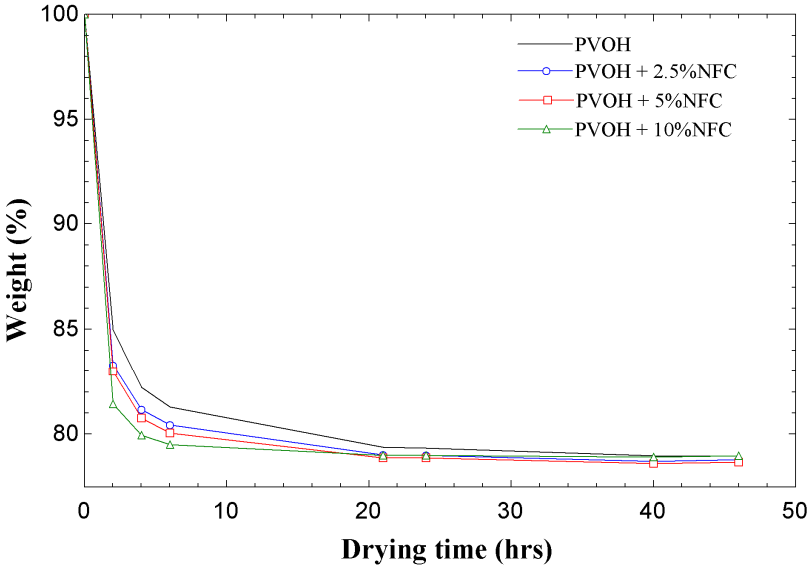

Figure 3.8 Weight of PVOH/NFC nanocomposites in a 90% humidity room as a function of time as they were dried at 90 ºC.

The logarithm of the storage modulus for PVOH nanocomposites prepared at the two moisture contents as a function of temperature are shown in Figure 3.9. At low temperatures (–25 to 0 ºC), it was difficult to observe any change in the storage modulus between the two moisture contents. In the glassy state, the tensile storage modulus, *E,* slightly decreased with temperature. Then, the modulus dropped at a temperature (around 25 or 50 ºC) that depended on moisture conditioning. The modulus dropped earlier for samples that were conditioned at 50% humidity and 25 ºC. At 25 ºC, high moisture content samples were soft and pliable but low moisture content samples led to a hard material [35]. Interestingly, for samples containing a lot of moisture and little or no NFC (Figure 3.9 (a)), the rubbery modulus was found to increase with temperature in the range of about 70 to 110 ˚C. This behavior might be caused by the loss of moisture during the DMA test. On the other hand, for dried samples (cf. Figure 3.9 (b)) at higher temperatures, the modulus dropped consistently. Regardless of the moisture content, the addition of NFC increased the rubbery modulus of the PVOH/NFC nanocomposites. Similar results have been reported in other studies [34,36].

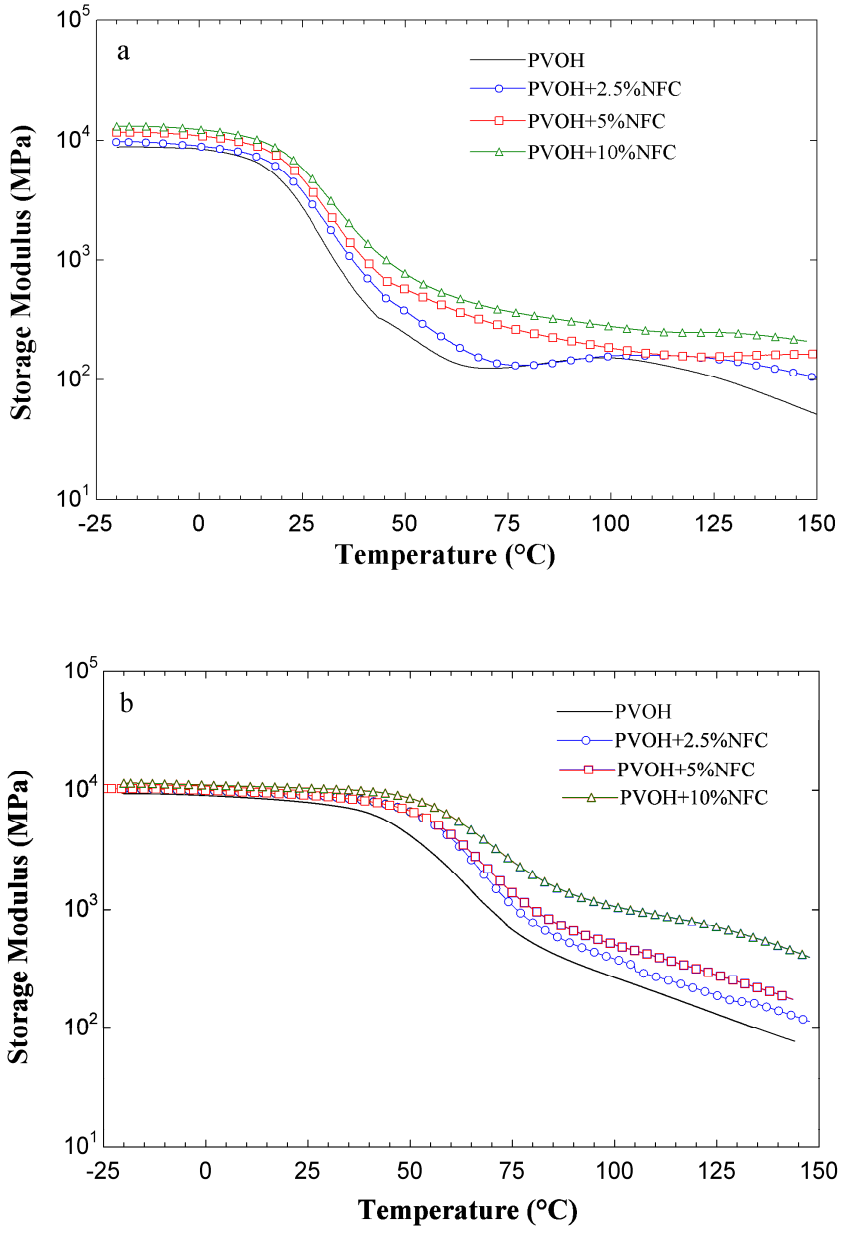

Figure 3.9 Storage moduli of the PVOH/NFC composite samples. (a) Samples were conditioned at 50% humidity at 25 ºC. (b) Samples were dried at 90 ºC for 2 days.

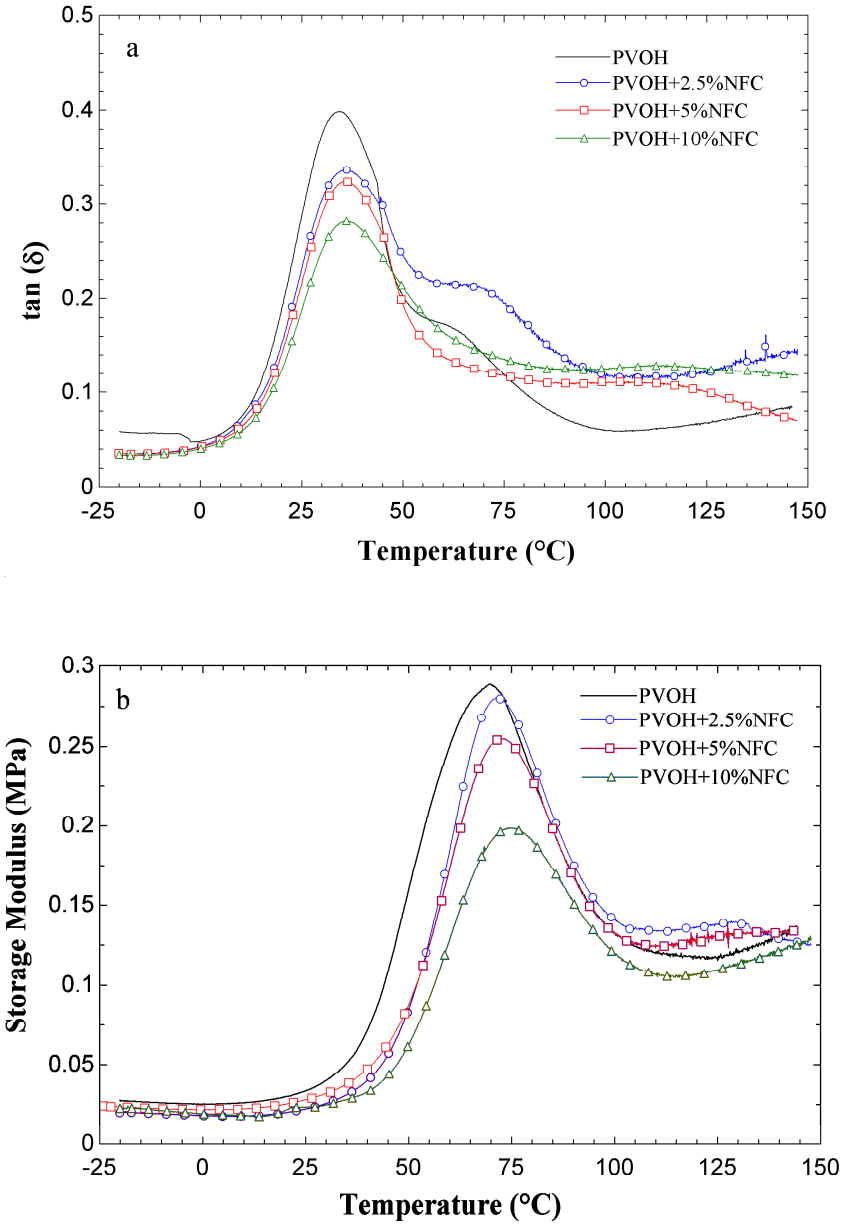

Figure 3.10 Tan-δ curves of the PVOH/NFC composite samples. (a) Samples were conditioned at 50% humidity. (b) Samples were dried at 90 ºC for 2 days.

The differences in mechanical properties can be attributed to the change in the glass transition temperature (T_g), which can be obtained from the peaks of the tan-δ curves in Figure

3.10. T_g shifted to a lower temperature as the moisture content increased and plasticized the PVOH [34]. Moreover, a slight shift of the peak position was observed upon the addition of NFC, regardless of the moisture content. For samples conditioned at 50% humidity, the peak position for PVOH was at 34.10 ºC and increased to 36.05 ºC for composites with 10% NFC. Also, the magnitude of the relaxation process strongly decreased with increasing NFC content (Figure 3.10). This indicates that fewer polymer chains participated in the transition. The increase in modulus, together with the positive shift in the tan-δ peak position, can be attributed to a physical interaction between the polymer and reinforcements that restricted the segmental mobility of the polymer chains in the vicinity of the nano-reinforcements [37].

3.3.6 Sorption Behavior of CO_2 in PVOH Nanocomposites

Cast PVOH and PVOH/NFC nanocomposite samples at two different moisture contents were originally weighed and then placed in a pressure vessel filled with CO_2 for one day. After depressurization, they were again placed on the scale to determine the amount of CO_2 absorbed and weight loss as a function of time. Samples with low moisture content absorbed little CO_2 and lost little weight as a function of time. Samples dried at 90 ºC for 2 days did not gain any weight and the amount of CO_2 absorbed could not be detected. However, PVOH and PVOH/NFC nanocomposite samples with high moisture content (i.e., those from the 90% humidity room) absorbed much more CO_2 due to the increased permeability of PVOH to CO_2 with moisture. This same observation was reported in other studies [38,39]. For the sake of brevity, only samples conditioned at 90% humidity are presented.

Figure 3.11 shows a plot of the measured solubility of CO_2 (%) in PVOH and PVOH/NFC nanocomposites. Note that the solubility of CO_2 in the specimens decreased as the

NFC content increased because NFC, which has high crystallinity, does not absorb CO_2 as reported by number of studies [35,40,41]. Neat PVOH was found to have around 3% CO_2 solubility. With the addition of 10% NFC, the apparent solubility of CO_2 decreased by as much as 33%, which was much higher than the 10% that might be expected. The additional reduction in weight gain might be because of faster gas loss while depressurizing the chamber and transferring the specimens to the scale. Accelerated weight loss with the addition of NFC was confirmed by desorption measurements.

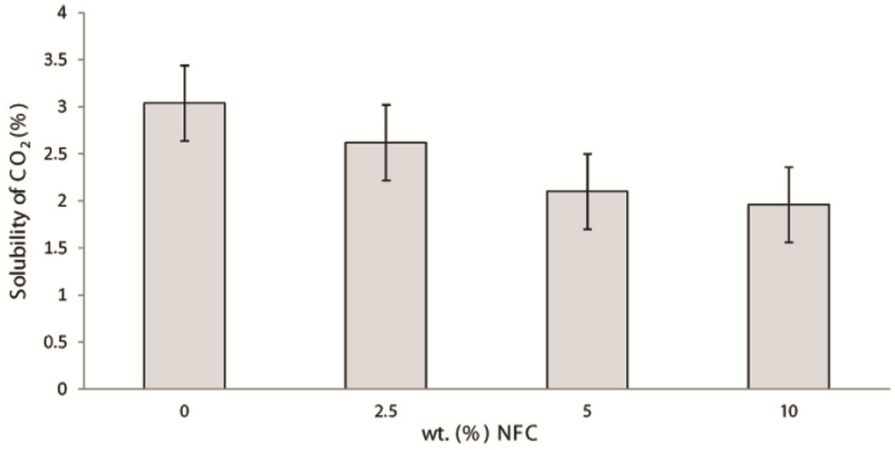

Figure 3.11 Solubility of CO_2 in PVOH and their nanocomposites with 2.5, 5, and 10 wt% NFC.

The desorption curves for CO_2 in the neat PVOH and PVOH/NFC nanocomposite samples around one to two hours are illustrated in Figure 3.12. There is around 40 second delay after depressurizing and before weighing. The weight loss during this short period of time can be estimated by extrapolating the relatively flat mass loss curves at time equals zero. The additional mass losses for all of the samples were found to be less than 2.5% of the total mass uptake. Note that, 40 seconds after depressurization the samples were kept in an oil bath on the scale. CO_2 gas that left the samples would pass through the oil which might cause some lag time of the weight

change. Thereafter, the slope became steeper as the NFC content increased, especially for the PVOH + 10% NFC specimen. Hence, the desorption diffusivity became higher as the amount of NFC increased. The increase in desorption diffusivity with increasing fiber content might be due to the interface between the fibers and the matrix which could provide a channel through which gas can quickly escape from the composites as reported in [35,40].

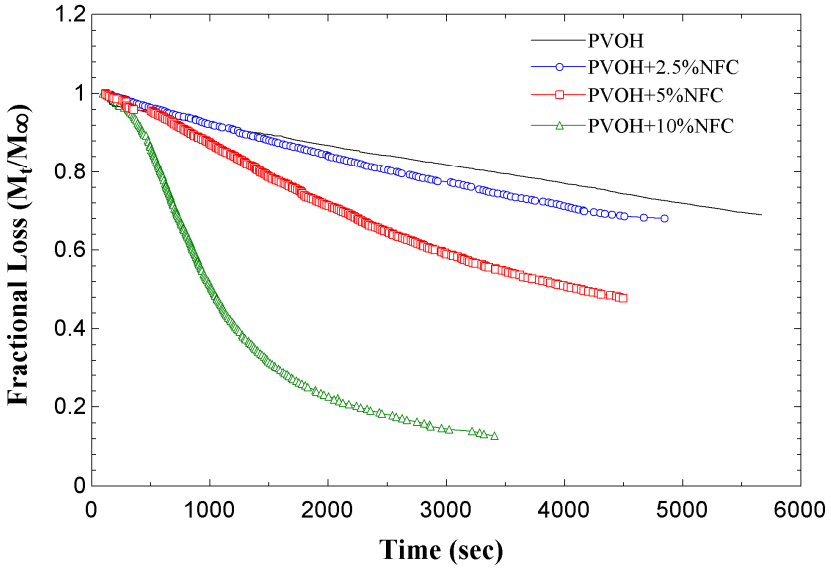

Figure 3.12 Desorption curves for CO_2 in PVOH and PVOH/NFC nanocomposites during the first hour; M_t is the amount of gas lost at time t and M_∞ is the mass uptake at infinite time.

3.3.7 Foamed PVOH/NFC Nanocomposites

To investigate their foaming behavior, specimens were placed in hot oil after removal from the CO_2 pressure vessel. Both specimens that were conditioned at 90% humidity or dried prior to placement in the pressure vessel were investigated. Dried PVOH nanocomposite samples did not appear to foam at the conditions used (Figure 3.13). On the other hand, at a high moisture content, some small cells can be clearly seen in the neat PVOH (Figure 3.14 (a)). These cells are

believed to be caused by CO_2 with moisture plasticizing the films, which can lower the resistance to gas cell growth [42,43]. Note that there were no visible cells found in the PVOH/NFC nanocomposites. This is probably because the nanocomposites had a higher strength at room temperature (Figure 3.9 (a)), which could hinder cell growth and reduce cell size [44].

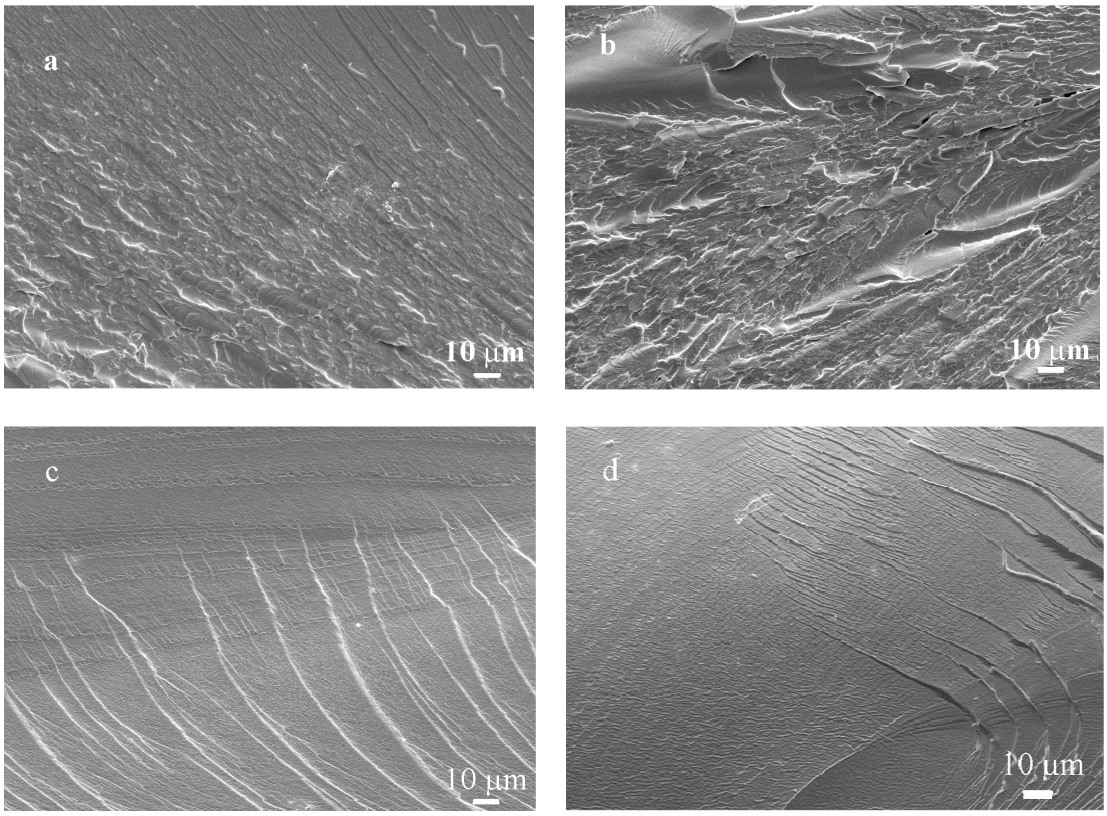

Figure 3.13 SEM images of dried PVOH and PVOH/NFC nanocomposites after they were placed into a CO_2 pressure vessel and subjected to a rapid pressure drop and hot oil treatment: (a) PVOH, (b) PVOH + 2.5% NFC, (c) PVOH + 5% NFC, and (d) PVOH + 10% NFC. No visible foaming was observed.

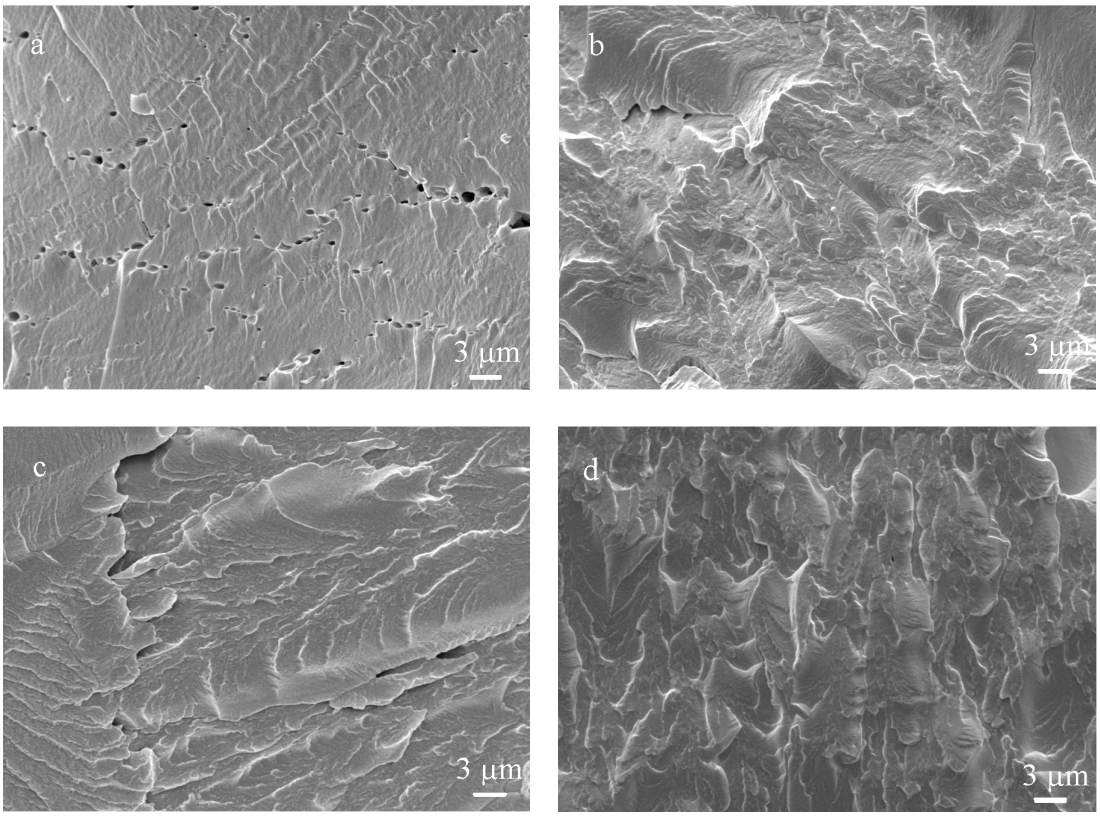

Figure 3.14 SEM images of high moisture content PVOH and PVOH/NFC nanocomposites after they were placed into a CO_2 pressure vessel and subjected to a rapid pressure drop at room temperature: (a) PVOH, (b) PVOH + 2.5% NFC, (c) PVOH + 5% NFC, and (d) PVOH + 10% NFC.

Figure 3.15 shows the SEM micrographs from the center portion of the cross-section of the tensile bars after foaming in a hot oil bath at 135 °C for 10 s. The cell size found in the neat PVOH in Figure 3.14 (a) increased with the hot oil treatment. This was due to the moisture vapor that was generated at the oil bath temperature and diffused into the cells, enlarging them. Furthermore, a greater number of cells formed in the PVOH/NFC nanocomposites. The reasons for the formation of these cavities in the PVOH/NFC nanocomposites is probably due to very

small cells that were created after depressurization but that could not be seen at the magnification in Figure 3.14 (b-d); the evaporation of moisture in the samples could enlarge these cells. In general, placing samples into the CO_2 pressure vessel for one day prior to depressurization helped to pre-condition the samples and generate small cells as nuclei. Subsequently, placing them into a hot oil bath allowed the moisture in the samples to evaporate and expand the pre-existing cell nuclei into a system of dense cells. Without CO_2 pre-conditioning, the moisturized sample exhibited severe cracking in the hot oil bath.

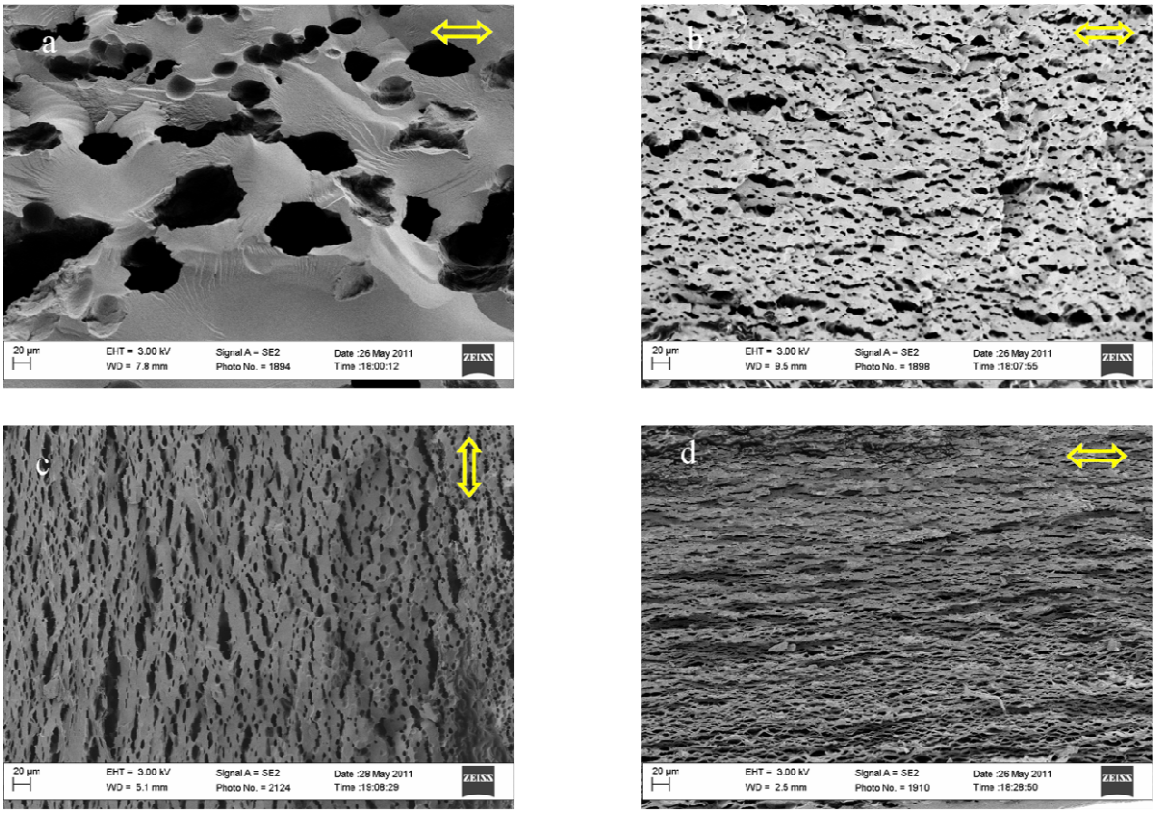

Figure 3.15 SEM images of high moisture content PVOH and PVOH nanocomposites foamed after hot oil treatment: (a) PVOH, (b) PVOH + 2.5% NFC, (c) PVOH + 5% NFC, and (d) PVOH + 10% NFC. Arrows indicate the planar direction (transverse to the long axis) of the sample.

The average cell size of the neat foamed PVOH was 32.6 μm and the cell morphology seemed more isotropic (Figure 3.16). For PVOH/NFC nanocomposites, the cells became less uniform and more extended in the planar directions (the long axis and width directions of the sample). This was probably due to the preferable orientation of NFC fibers parallel to the film surface that hampered gas diffusion and cell growth in the thickness direction. In addition, cell size in the PVOH/NFC nanocomposites generally decreased with increasing NFC content and the cell density increased, suggesting that NFC nucleates cells. These results agree with findings from the literature on other types of nanocomposites [45-47]. It should be pointed out that a few larger cells observed in the PVOH/NFC nanocomposites were likely formed by evaporated vapor from the NFC instead of CO_2, thus resulting in a large error bar. The densities of the solid neat PVOH and PVOH/NFC nanocomposites were all around 1310 kg/m^3, and that of the foamed samples were 1082, 1102, 1050, and 1120 kg/m^3 for PVOH, PVOH + 2.5% NFC, PVOH + 5% NFC, and PVOH + 10% NFC, respectively.

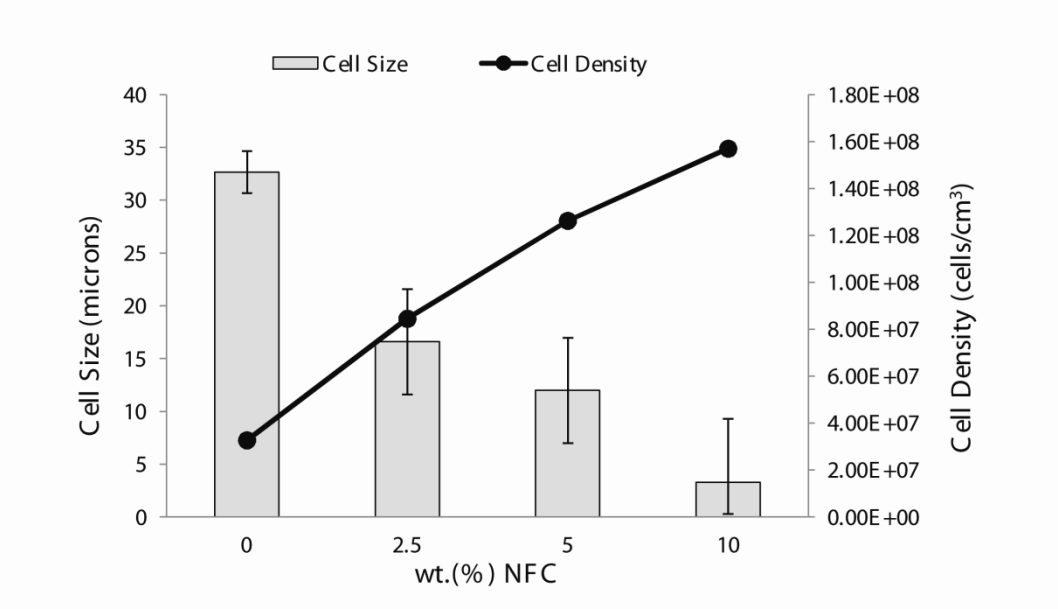

Figure 3.16 The average cell size and cell density of foamed PVOH nanocomposites.

3.3.8 Tensile Properties of Foamed PVOH Nanocomposites

Tensile tests were performed on the foamed specimens of the PVOH/NFC nanocomposites (cf. Figure 3.17). The specific Young's modulus was obtained by dividing the modulus by the density.

As shown in Figure 3.17 (a), the addition of NFC increased the specific Young's modulus of both solid and foamed samples significantly. The specific Young's modulus of the foamed specimens was generally higher than that of their solid counterparts but there was no significant difference in the specific strength (Figure 3.17 (b)). However, the strain-at-break (Figure 3.17 (c)) of the foamed specimens was lower. This can be attributed to the presence of large cells that served as stress concentrators in the foamed samples [48].

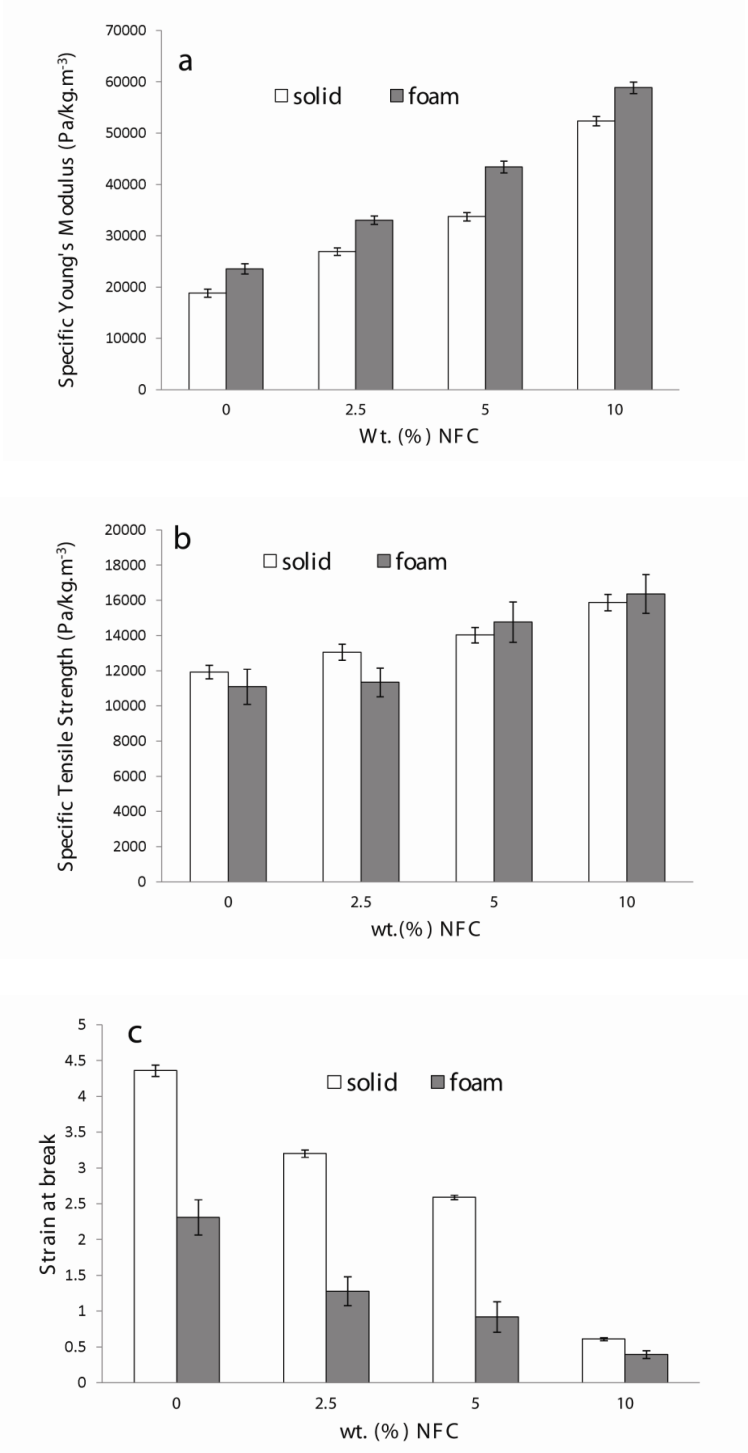

Figure 3.17 Specific mechanical properties of solid and foamed PVOH/NFC nanocomposites: (a) specific Young's modulus (Pa/kg m^3), (b) specific tensile strength (Pa/kg.m^{-3}), and (c) strain at break.

3.4 Conclusions

NFC dispersed well in PVOH by blending a suspension of NFC with a solution of PVOH. PVOH/NFC nanocomposite films were then formed by a casting/evaporation technique. NFC had a reinforcing effect on PVOH, as observed via both DMA and tensile tests. However, toughness decreased as the amount of NFC increased. The addition of NFC to PVOH was shown to increase the crystallization and glass transition temperatures, but it also caused thermal degradation of the polymer, likely due to an increase in moisture. The sorption degree of CO_2 in the nanocomposites was dependent on the moisture content in the samples as solubility increased with higher moisture contents. The solubility was around 3% in neat PVOH conditioned at 90% humidity and decreased as the amount of NFC increased. Moreover, the desorption diffusivity increased as more NFC was added. The moisture in the neat PVOH and PVOH/NFC nanocomposites acted as a plasticizer and enabled foaming by a batch foaming process. In addition, vapor that came from the evaporation of moisture in the samples also acted as a physical blowing agent by diffusing into the cells and enlarging them. Finally, the addition of NFC increased cell density and decreased cell size in moisture-enabled foamed PVOH/NFC nanocomposites.

3.5 References

1. Ahola S. Properties and interfacial behaviour of cellulose nanofibrils [Article Dissertation]. Faculty of Chemistry and Material Sciences: Department of Forest Products Technology, Helsinki University of Technology; 2008.

2. Nakagaito A, Yano H. The effect of morphological changes from pulp fiber towards nano-scale fibrillated cellulose on the mechanical properties of high-strength plant fiber based composites. Applied Physics A: Materials Science & Processing.78(4):547-552, 2004.

3. Andresen M, Johansson LS, Tanem BS, Stenius P. Properties and characterization of hydrophobized microfibrillated cellulose. Cellulose.13(6):665-677, 2006.

4. Iwamoto S, Nakagaito A, Yano H. Nano-fibrillation of pulp fibers for the processing of transparent nanocomposites. Applied Physics A: Materials Science & Processing.89(2):461-466, 2007.

5. Alemdar A, Sain M. Isolation and characterization of nanofibers from agricultural residues-Wheat straw and soy hulls. Bioresource technology.99(6):1664-1671, 2008.

6. Siqueira G, Bras J, Dufresne A. Cellulosic Bionanocomposites: A Review of Preparation, Properties and Applications. Polymers.2(4):728-765, 2010.

7. Dufresne A, Cavaillé JY, Vignon MR. Mechanical behavior of sheets prepared from sugar beet cellulose microfibrils. Journal of applied polymer science.64(6):1185-1194, 1997.

8. Jonoobi M, Harun J, Mathew AP, Oksman K. Mechanical properties of cellulose nanofiber (CNF) reinforced polylactic acid (PLA) prepared by twin screw extrusion. Composites science and technology.70(12):1742-1747, 2010.

9. Samir MASA, Alloin F, Dufresne A. Review of recent research into cellulosic whiskers, their properties and their application in nanocomposite field. Biomacromolecules.6(2):612-626, 2005.

10. Osswald TA. International plastics handbook: the resource for plastics engineers: Hanser Verlag; 2006.

11. Syverud K, Stenius P. Strength and barrier properties of MFC films. Cellulose.16(1):75-85, 2009.

12. Sanchez-Garcia MD, Lagaron JM. On the use of plant cellulose nanowhiskers to enhance the barrier properties of polylactic acid. Cellulose.17(5):987-1004, 2010.

13. Tang X, Alavi S. Recent advances in starch, polyvinyl alcohol based polymer blends, nanocomposites and their biodegradability. Carbohydrate polymers. 2011.

14. Labuschagne PW, Germishuizen WA, C Verryn SM, Moolman FS. Improved oxygen barrier performance of poly (vinyl alcohol) films through hydrogen bond complex with poly (methyl vinyl ether-co-maleic acid). European Polymer Journal.44(7):2146-2152, 2008.

15. Stern S, Shah V, Hardy B. Structure-permeability relationships in silicone polymers. Journal of Polymer Science Part B: Polymer Physics.25(6):1263-1298, 1987.

16. Avella M, Cocca M, Errico M, Gentile G. Biodegradable PVOH-based foams for packaging applications. Journal of Cellular Plastics.47(3):271, 2011.

17. Saito T, Okita Y, Nge T, Sugiyama J, Isogai A. TEMPO-mediated oxidation of native cellulose: Microscopic analysis of fibrous fractions in the oxidized products. Carbohydrate polymers.65(4):435-440, 2006.

18. Standard test method for tensile properties of plastics. *ASTM D638-10*: ASTM International.

19. Bulota M, Jääskeläinen A, Paltakari J, Hughes M. Properties of biocomposites: influence of preparation method, testing environment and a comparison with theoretical models. Journal of materials science.1-12, 2011.

20. Davies W. The elastic constants of a two-phase composite material. Journal of Physics D: Applied Physics.4:1176, 1971.

21. Davies W. The theory of composite dielectrics. Journal of Physics D: Applied Physics.4:318, 1971.

22. Allen G, Bowden M, Todd S, Blundell D, Jeffs G, Davies W. Composites formed by interstitial polymerization of vinyl monomers in polyurethane elastomers: 5. Variation of modulus with composition. Polymer.15(1):28-32, 1974.

23. Standard test methods for density and specific gravity (relative density) of plastics *ASTM D792-08*: ASTM International.

24. Poling BE, Thomson GH, Friend DG, Rowley RL, Wilding WV. Perry's Chemical Engineer's Handbook2008.

25. Naguib HE, Park CB, Panzer U, Reichelt N. Strategies for achieving ultra low density polypropylene foams. Polymer Engineering & Science.42(7):1481-1492, 2002.

26. Siró I, Plackett D. Microfibrillated cellulose and new nanocomposite materials: a review. Cellulose.17(3):459-494, 2010.

27. Sharma S. Economics of Composites and Reinforcements. Composite Materials,, 1st Ed., Narosa Publishing House: New Delhi.20-25, 2002.

28. Probst O, Moore EM, Resasco DE, Grady BP. Nucleation of polyvinyl alcohol crystallization by single-walled carbon nanotubes. Polymer.45(13):4437-4443, 2004.

29. Liu M, Guo B, Du M, Jia D. Drying induced aggregation of halloysite nanotubes in polyvinyl alcohol/halloysite nanotubes solution and its effect on properties of composite film. Applied Physics A: Materials Science & Processing.88(2):391-395, 2007.

30. Holland B, Hay J. The thermal degradation of poly (vinyl alcohol). Polymer.42(16):6775-6783, 2001.

31. Finch CA. Polyvinyl alcohol: properties and applications. Vol 339: Wiley New York; 1973.

32. Mathew AP, Thielemans W, Dufresne A. Mechanical properties of nanocomposites from sorbitol plasticized starch and tunicin whiskers. Journal of applied polymer science.109(6):4065-4074, 2008.

33. Coleman JN, Cadek M, Blake R, et al. High performance nanotube-reinforced plastics: understanding the mechanism of strength increase. Advanced Functional Materials.14(8):791-798, 2004.

34. Roohani M, Habibi Y, Belgacem NM, Ebrahim G, Karimi AN, Dufresne A. Cellulose whiskers reinforced polyvinyl alcohol copolymers nanocomposites. European Polymer Journal.44(8):2489-2498, 2008.

35. Doroudiani S, Chaffey CE, Kortschot MT. Sorption and diffusion of carbon dioxide in wood-fiber/polystyrene composites. Journal of Polymer Science Part B: Polymer Physics.40(8):723-735, 2002.

36. Lu J, Wang T, Drzal LT. Preparation and properties of microfibrillated cellulose polyvinyl alcohol composite materials. Composites Part A: Applied Science and Manufacturing.39(5):738-746, 2008.

37. Javadi A, Srithep Y, Lee J, et al. Processing and characterization of solid and microcellular PHBV/PBAT blend and its RWF/nanoclay composites. Composites Part A: Applied Science and Manufacturing.41(8):982-990, 2010.

38. Piringer OG, Baner AL. Plastic packaging materials for food: barrier function, mass transport, quality assurance, and legislation: LibreDigital; 2000.

39. Marten FL. Vinyl alcohol polymers. Encyclopedia Of Polymer Science and Technology. 1989.

40. Rachtanapun P, Selke S, Matuana L. Microcellular foam of polymer blends of HDPE/PP and their composites with wood fiber. Journal of applied polymer science.88(12):2842-2850, 2003.

41. Matuana LM, Park CB, Balatinecz JJ. Cell morphology and property relationships of microcellular foamed pvc/wood-fiber composites. Polymer Engineering & Science.38(11):1862-1872, 1998.

42. Zhu B, Zha W, Yang J, Zhang C, Lee LJ. Layered-silicate based polystyrene nanocomposite microcellular foam using supercritical carbon dioxide as blowing agent. Polymer.51(10):2177-2184, 2010.

43. Kumar V, Nadella KV. Microcellular Foams. In: Eaves D, ed. *Handbook of polymer foams*. Shropshire, UK: Smithers Rapra Press; 2004:243-268.

44. Lee LJ, Zeng C, Cao X, Han X, Shen J, Xu G. Polymer nanocomposite foams. Composites science and technology.65(15-16):2344-2363, 2005.

45. Chandra A, Gong S, Yuan M, Turng LS, Gramann P, Cordes H. Microstructure and crystallography in microcellular injection molded polyamide 6 nanocomposite and neat resin. Polymer Engineering & Science.45(1):52-61, 2005.

46. Yuan M, Winardi A, Gong S, Turng LS. Effects of nano and micro fillers and processing parameters on injection molded microcellular composites. Polymer Engineering & Science.45(6):773-788, 2005.

47. Gong S, Yuan M, Chandra A, Kharbas H, Osorio A, Turng L. Microcellular injection molding. International Polymer Processing.20(2):202-214, 2005.

48. Kramschuster A, Gong S, Turng LS, Li T. Injection-molded solid and microcellular polylactide and polylactide nanocomposites. Journal of Biobased Materials and Bioenergy.1(1):37-45, 2007.

CHAPTER 4

Melt Compounding of Poly (3-hydroxybutyrate-co-3-hydroxyvalerate) (PHBV) / Nanofibrillated Cellulose (NFC) Nanocomposites: Properties, Solubility of Carbon Dioxide, and Foaming

4.1 Introduction

The development of commercially viable biodegradable plastics is an important effort in preserving and revitalizing our global environment and economy. Polyhydroxyalkanoates (PHAs) have attracted much attention over the last two decades mainly due to increasing environmental concerns and the realization that our petroleum resources are finite [1,2]. PHAs have received a great deal of research interest because their mechanical performance is similar to petroleum-based polymers such as polypropylene (PP) [3]. PHAs, which also include poly(3-hydroxybutyrate) (PHB) and copolymer poly(3-hydroxybutyrate-co-3-hydroxyvalerate) (PHB/HV), are a family of polyesters that are synthesized and intracellularly accumulated as a carbon and energy storage material in various microorganisms, [4]. Generally, PHB/HV (or PHBV) is less crystalline and more flexible than the highly crystalline and relatively brittle and hydrophobic PHB [5].

Reinforcing fibers of various sizes and forms—e.g., natural plant fibers (cellulose fibers), glass fibers, carbon fibers, carbon nanotubes, etc. —have been effectively used in polymer composites as reinforcing agents [3]. Nanofillers, however, are found to be preferable in many applications due to their high surface area-to-volume ratios, lower concentrations needed to

achieve reinforcing effects, and the ability to potentially improve toughness along with strength and stiffness. Nanofibrillated cellulose (NFC), a biologically derived nanofiber reinforcement suitable for polymeric materials, is an interconnected web with fibrils having a diameter in the range of 10 to 50 nm [6]. Although NFC has numerous advantages, which include low density, renewability, high specific properties, biodegradability, gas barrier properties, and derivation from abundant natural resources, the processing temperatures for these materials are restricted to about 200 °C due to degradation beyond this temperature [7-9]. Another drawback of using NFC is the difficulty in dispersing them uniformly in a non-polar medium because of their polar surface [10]. Therefore, the use of NFC in nanocomposites has mainly been limited to aqueous or polar environments and the processing techniques have been limited to the laboratory scale. Thus, it will be important to develop new processing techniques which can be scaled up and used industrially.

It is well known that when a low molecular weight compound, such as carbon dioxide, comes into contact with a polymer, sorption of the low molecular weight specie by the polymer occurs. Carbon dioxide at high pressure can be dissolved in a polymeric matrix [11]. The use of CO_2 as a solvent or physical blowing agent offers the possibility to develop new “clean and environmental friendly” techniques for polymer processing and foams. It is therefore of interest in this study to measure the solubility of CO_2 in PHBV and PHBV/NFC nanocomposites.

Polymeric foams find application as materials for thermal and acoustic insulation, energy dissipation, shock protection, packaging, etc. [12]. Polymeric foams are light weight and offer better thermal insulation compared to solid materials. This study also carried out batch foaming experiments using CO_2 as a physical blowing agent to investigate the influence of NFC on the foaming behavior of PHBV/NFC nanocomposites.

It is hoped that the resulting biobased and biodegradable PHBV/NFC nanocomposites may find many potential applications in the fields of structural components, packaging, and biomedical devices [13,14]. Various characterization techniques analyzing mechanical, morphological, and thermal properties were employed to characterize the PHBV/NFC nanocomposites. Moreover, the solubility of carbon dioxide was measured and the foaming properties of PHBV and PHBV/NFC nanocomposites were evaluated.

4.2 Experiments

4.2.1 Materials

The materials used in this study were PHBV powder and NFC. PHBV powder under the trade name Y1000 was purchased from Ningbo Tianan Biologic Material Co. Ltd. (Tinan-ENMAT, China). The percentage of HV in the PHBV copolymer (Y1000) was 3%.

NFC was prepared according to a procedure described by Saito and Isogai [14]. In particular, fully bleached Kraft eucalyptus fibers were oxidized with sodium hypochlorite using tetramethylpiperidine-1-oxy radical (TEMPO) sodium bromide as a catalyst. The TEMPO-mediated oxidation was carried out at a pH of 10 at 25 °C for 3 hours. The fibers were then thoroughly washed and refined in a disk refiner with a gap of approximately 200 μm. The coarse fibers were separated by centrifuging at a force of 12,000 G, and the nanofiber dispersion was concentrated to 1% using ultrafiltration. A final clarification step was performed in which the nanofiber dispersion was passed once through an M-110EH-30 microfluidizer (Microfluidics, Newton, MA) with 200 μm and 87 μm chambers in series. An aqueous suspension of NFC fibers at 0.4 wt% was obtained and used in this study.

4.2.2 Sample Preparation

Composites were prepared using a two-step process. Masterbatch preparations using a freeze drier were followed by melt compounding, as described below.

Preparation of the Masterbatch

PHBV powder was first dispersed in distilled water, stirred for 1 hour, and then mixed with an aqueous suspension of NFC to reach a dry weight ratio between PHBV and NFC of 85:15 (15% NFC). The mixture was then stirred overnight using a magnetic stirrer. To prepare the composites, the water medium had to be removed from the corresponding aqueous suspension of NFC while the NFC fibers remained fully dispersed. Hence, the suspension was quickly frozen by liquid nitrogen to prevent the PHBV powder from settling. In addition, rapid freezing might avoid NFC aggregation during freeze drying, as report by Pääkkö et al. [15]. The frozen mixture was then freeze dried using a 4.5 L Labconco FreeZone freeze drier to remove the water thoroughly. The dried PHBV + 15% NFC masterbatch was later diluted to 2.5, 5, and 10 wt% NFC content by melt compounding, as described below.

Melt Compounding and Preparation of Specimens

PHBV composites with 0, 2.5, 5, and 10 wt% NFC content were prepared by melt compounding of the PHBV powders and the NFC masterbatch. PHBV was dried in an oven for 2 hours at 90 °C before processing and melt compounding was done using a thermokinetic mixer (K-mixer). The nanocomposites were then compounded in 50 g batches and discharged when the temperature reached 180 °C. There was no external heating source in the K-mixer besides frictional (viscous) heating and the compounding process was completed in less than two

minutes. This short heating/mixing time reduced the potential for thermal degradation. The K-mixer's rotor speed was set at 6000 rpm. After discharge, the molten nanocomposite was subsequently granulated. Tensile bars (ASTM D638 Type V, 63.5 mm by 3.2 mm by 1.6 mm), flexural specimens (nominal dimensions of 125.0 mm by 12.7 mm by 3.2 mm), and rectangular specimens (nominal dimensions of 25 mm by 25 mm by 1.2 mm) were injection molded using a micro injection molding machine (DSM Xplore, Geleen, The Netherlands). The molding was done at 180 ºC with a mold temperature of 25 ºC, a cooling time of 15 seconds, and a holding pressure of 7 bars.

4.2.3 Tensile Testing

Tensile tests were performed on the injection molded tensile specimens following the ASTM D638 standard [16]. The static tensile modulus, strength, and strain-at-break were measured at room temperature (25 °C) and atmospheric conditions (relative humidity of 50 ± 5%) on an Instron 5865 mechanical testing instrument. The tensile tests were performed on all specimens using an initial load of 0.5 N and a constant crosshead speed of 1 mm/min. Five specimens of each sample group were tested and the average results were reported.

4.2.4 Scanning Electron Microscopy (SEM)

SEM images were examined using an SEM (JEOL Neoscope Benchtop) operated at 10 kV. All specimens were sputter-coated with a thin layer of gold (~20 nm) prior to examination.

4.2.5 Differential Scanning Calorimetry (DSC)

A differential scanning calorimeter (Q20 TA Instruments) was used to study the thermal properties of the nanocomposites. Specimens of 5 to 10 mg were placed in aluminum sample pans and heated from –50 °C to 210 °C at a 10 °C/min heating rate and held for 3 min at 210 °C to erase any prior thermal history before cooling at a rate of 10 °C/min to a temperature of –50 °C. The specimens were then reheated to 210 °C and cooled down to room temperature using the same heating and cooling rates of 10 °C/min. The crystallization temperature (T_c), melting temperature (T_m), and apparent melting enthalpy (ΔH_f) were determined from the DSC curves.

The absolute degree of crystallinity (χ_c) of the PHBV phase was calculated by

$$\chi_c\,(\%) = \frac{\Delta H_f\,(PHBV)}{\Delta H^{\circ}(PHBV)} \times \frac{100}{w} \tag{4.1}$$

where ΔH°(PHBV) is the enthalpy of melting per gram of 100% crystalline (perfect crystal; 109 J/g) and *w* is the weight fraction of PHBV in the nanocomposites [2].

4.2.6 Polarized Optical Microscopy (POM)

Crystallization behavior of the samples was studied by an Leitz SM-Lux POM. Microtomed PHBV/NFC nanocomposite specimens from the injection molded samples were sandwiched between two glass slides and heated to 230 ºC. The specimens were equilibrated for 3 min to eliminate any residual PHBV crystallization seeds and then cooled down slowly to room temperature. Images of PHBV spherulites were taken by an attached digital camera

4.2.7 Gel Permeation Chromatography (GPC)

The number- and weight-average molecular weights (Mn and Mw, respectively) and the polydispersity index (PDI; calculated as the ratio of Mw/Mn) for injection molded PHBV/NFC samples were determined by gel permeation chromatography (GPC). Specimens weighing 7.5 mg were dissolved in 3 mL of HPLC-grade chloroform via continuous stirring in a constant temperature sand bath (60 ºC) for 1 hour. The specimen solution was filtered through a 0.2 mm PTFE membrane filter. With an eluent flow rate of 1.0 mL/min, 100 mL specimens were injected into a Viscotek model VE2001 with Model 302-050 tetra detector array (differential refractive index (RI)). The system was calibrated using polystyrene standards.

4.2.8 Thermogravimetric Analysis (TGA)

Specimens used for thermogravimetric analysis (TGA) were first dried at 90 °C for 2 days prior to testing. TGA was performed using a TGA Q50 (TA Instruments) from 25 to 600 °C at a heating rate of 10 °C/min. Approximately 10 mg of neat PHBV, neat NFC, or nano-composites of various NFC content were used for each test. The weight loss was recorded and normalized against the initial weight.

4.2.9 Dynamic Mechanical Analysis (DMA)

Dynamic mechanical analysis measurements were performed on a DMA Q800 (TA instrument) in single cantilever mode. The dimensions of the rectangular specimen were 17.6 mm by 12.7 mm by 3.2 mm, which were cut from injection molded samples. During the DMA test, the specimens were heated at a rate of 3 K/min from –30 to 120 ºC with a frequency of 1 Hz

and a strain of 0.02%, which was in the linear viscoelastic region as determined by a strain sweep.

4.2.10 Absorption and Desorption Measurements

It is well known that when a low molecular weight compound, such as carbon dioxide (CO_2), comes into contact with a polymer, absorption of the low molecular weight species by the polymer occurs [17]. The main purpose of the absorption and desorption experiments was to establish the amount of CO_2 absorbed in the PHBV and PHBV/NFC nanocomposites (or gas solubility) and the rate of gas diffusivity (or gas diffusivity), which are important factors in the gas foaming process [18,19]. The original weights of these samples were measured using a digital balance readable to 0.0001 g. Absorption of CO_2 was facilitated by placing the specimens in a high-pressure vessel under a CO_2 gas pressure of 5.52 MPa (800 psi) at room temperature. Afterward, the vessel was depressurized and the CO_2-absorbed specimens were removed from the pressure vessel and placed on a balance to record the CO_2 sorption in the pressure chamber (weight gain). The process of depressurization and removing the samples from the pressure chamber and weighing them took around 40 s. As soon as no further weight gain was recorded, the desorption process was carried out immediately to determine the amount of gas lost from the sorption curves. The diffusivities (D) for absorption and the desorption were derived as follows [20,21]:

$$D = \frac{\pi}{16}\left[\frac{d\left(\frac{M_t}{M_\infty}\right)}{d\left(\frac{\sqrt{t}}{l}\right)}\right]^2 \qquad (4.2)$$

where M_t is the amount of gas lost at time t, M_∞ is the mass uptake at infinite time, and l is the thickness of the sample.

4.2.11 Foam Preparation

To produce foamed structures in PHBV and PHBV/NFC nanocomposites, the CO_2-saturated samples were subjected to a rapid pressure drop and a rapid temperature increase that resulted in the nucleation and growth of gas nuclei. This was achieved by taking the samples out of the pressure chamber and heating them in a hot oil bath. The rapid decompression and rapid heating induced a sudden gas solubility drop in the samples [22]. This sudden drop of gas solubility created a thermodynamic instability in the gas/polymer solution, which caused the microcells to nucleate. Once the cells nucleated, they continued to grow until the material solidifies or the gas concentration drops below the solubility level [18].

4.3 Results and Discussions

4.3.1 Freeze Dried Aqueous Suspension of NFC

The SEM images of PHBV powder, freeze-dried NFC, and freeze-dried PHBV + 15% NFC masterbatch are shown in Figures 4.1 (a), (b), and (c), respectively. As shown in Figure 4.1 (a), the individual PHBV powder is smaller than 1 μm. Freeze-dried NFC (Figure 4.1 (b)) shows an interconnected fibrillar skeleton structure with diameters on the order of 1 μm, although some of the nanofibers aggregated to form essentially 2-dimensional extended sheet-like structures. The observed fibrillar diameter after freeze drying was much larger than what was observed (e.g., 5–10 nm) in aqueous gels using transmission electron microscopy (TEM) in a previous study (Figure 4.1 (d)) [6]. This indicates that some aggregation of the nanofibers took place in

the process of freeze drying. Similar behavior in freeze drying results has been reported in another study [15]. For the freeze-dried PHBV + 15% NFC, Figure 4.1 (c) shows that some of the PHBV powder attached to the fibrillar NFC network, while some of it aggregated. This PHBV + 15% NFC was used as the masterbatch in the subsequent melt compounding process.

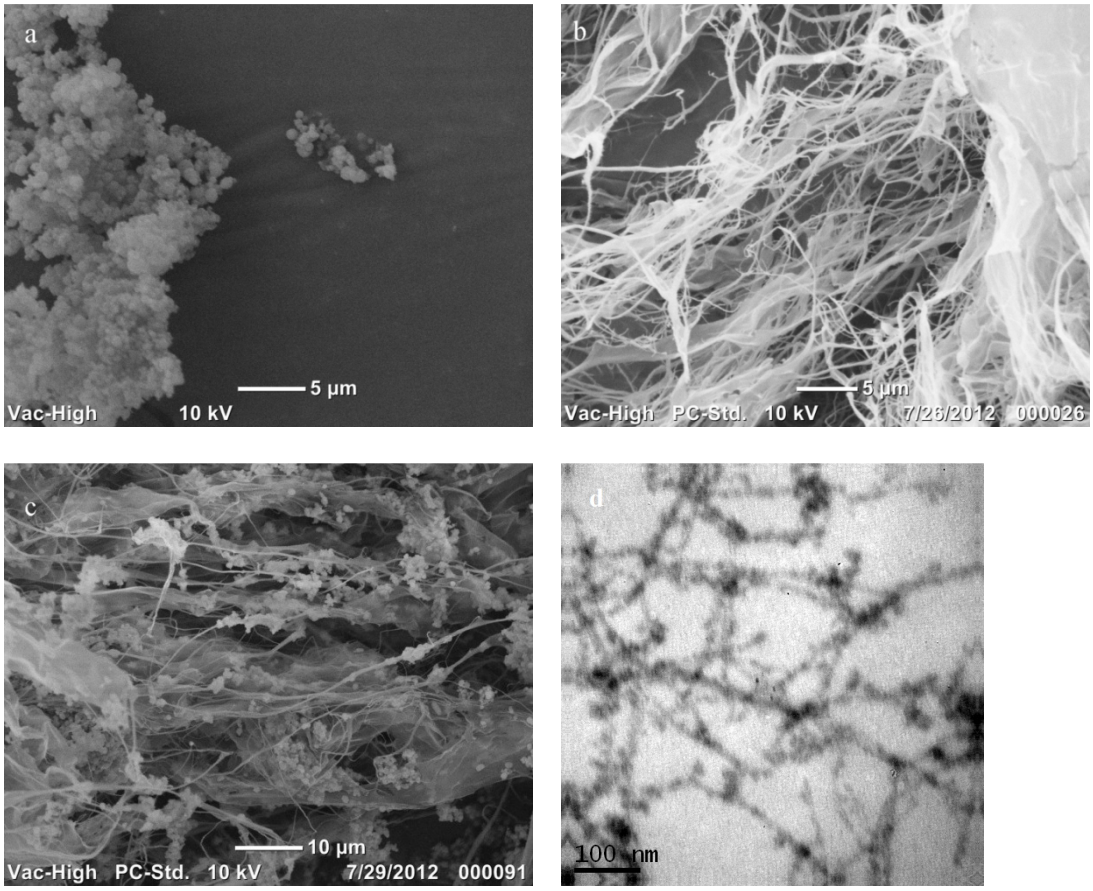

Figure 4.1 SEM images of: (a) PHBV powder, (b) freeze-dried NFC, (c) freeze-dried PHBV + 15% NFC, and (d) TEM image of NFC in aqueous gels in a previous study [6].

4.3.2 Tensile Properties

Tensile tests were performed on the injection molded ASTM D638 Type V specimens of the PHBV/NFC nanocomposites. Representative stress–strain curves are featured in Figure 4.2. Properties such as tensile modulus, tensile strength, and strain-at-break were measured as shown in Table 4.1. The addition of NFC increased the composite Young's modulus significantly. Furthermore, the addition of 2.5, 5, and 10 wt% NFC increased neat PHBV stiffness by 22%, 54%, and 90% respectively.

In general, the tensile strength of filled composites was found to be the same as the virgin polymer. Furthermore, the ultimate strain of neat PHBV decreased with increased fiber loading. Maximum elongation decreased more than one-half, from 8.8% for neat PHBV to 3.9% with the addition of 10 wt% NFC. The slight increase in strength and decrease in elongation in the composites might be attributed to an embrittlement caused by some agglomeration of the NFC and nanocomposite degradation. This degradation, which will be discussed later, was further confirmed by DSC, GPC, and TGA results. The SEM micrograph of tensile fracture surfaces of neat PHBV and PHBV/NFC nanocomposites in Figure 4.3 clearly shows that some NFC agglomerated, even though individual fibers with a diameter on the order of 1 μm (cf. Figure 2.3d) could still be clearly distinguished.

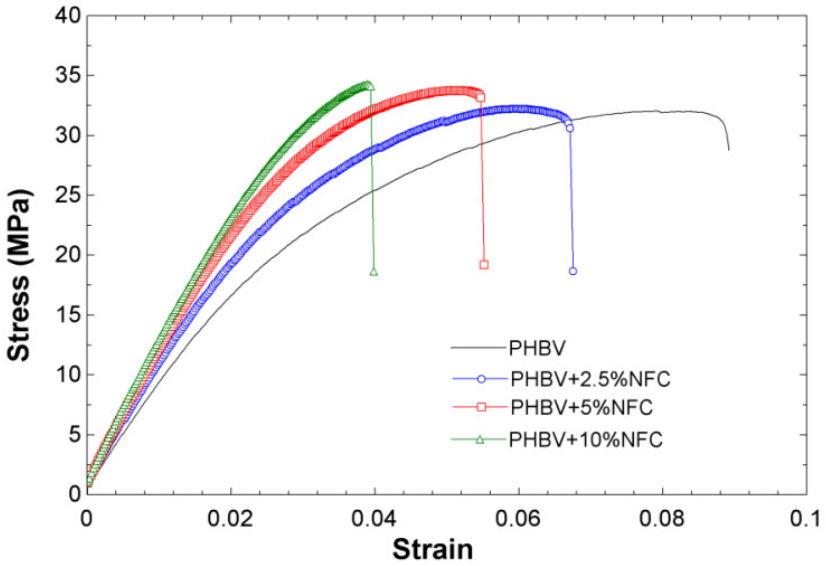

Figure 4.2 Tensile stress versus strain curve for NFC and PHBV nanocomposites.

Table 4.1 Tensile properties of PHBV/NFC nanocomposites.

Sample	**Ultimate Tensile Strength (MPa)**	**Tensile Modulus (MPa)**	**Strain at Break**
PHBV	31.7 ± 0.3	1681.5 ± 36.2	0.088 ± 0.01
PHBV + 2.5% NFC	32.1 ± 1.0	2064.7 ± 142.6	0.067 ± 0.01
PHBV + 5% NFC	34.4 ± 0.3	2601.4 ± 49.1	0.055 ± 0.004
PHBV + 10% NFC	34.3 ± 0.4	3196.4 ± 87.3	0.039 ± 0.002

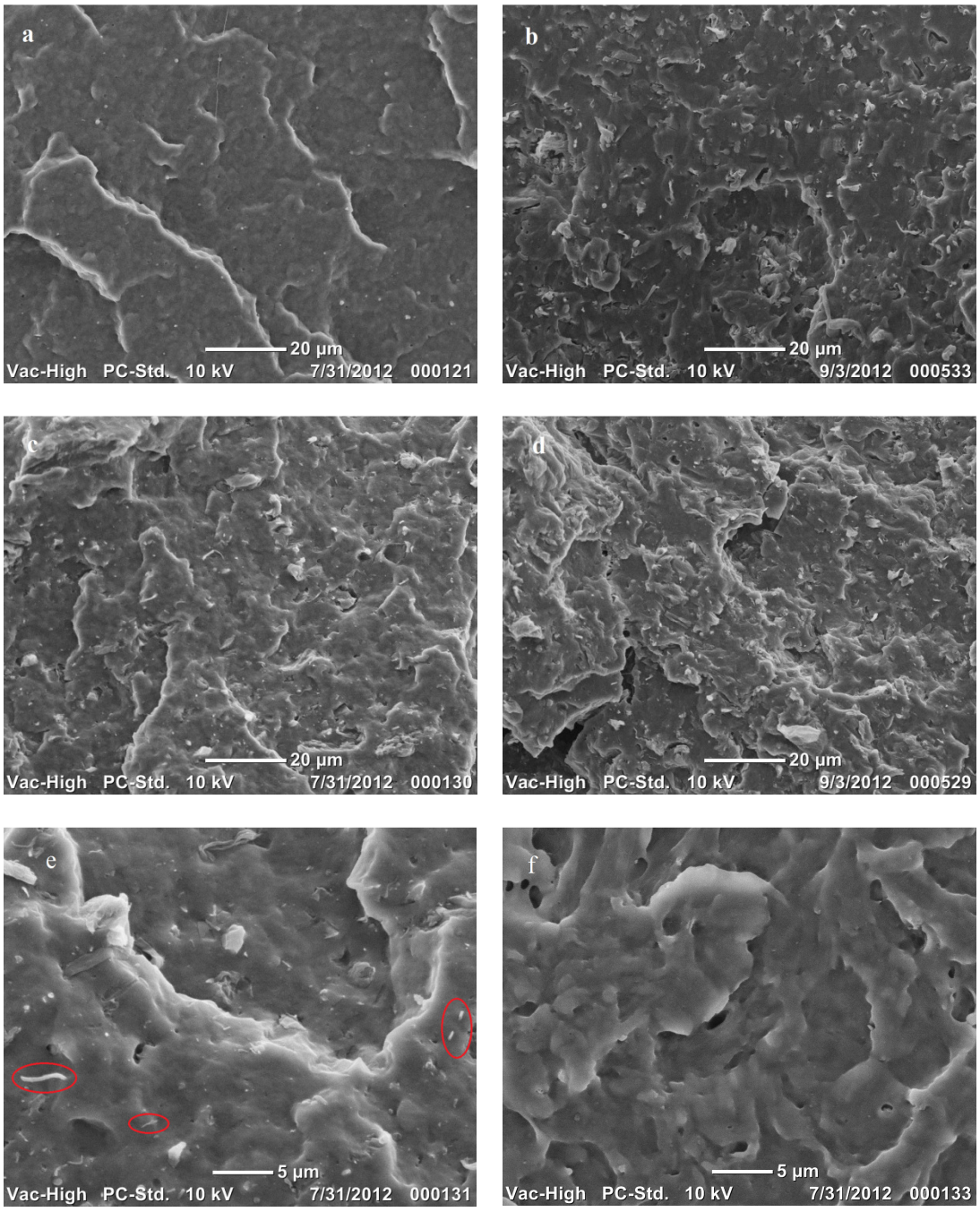

Figure 4.3 Tensile fractured surfaces of (a) PHBV, (b) PHBV + 2.5% NFC, (c) PHBV + 5% NFC, and (d) PHBV + 10% NFC, (e) higher magnification of Figure 3c), and (f) higher magnification of Figure 3a).

4.3.3 Thermal Properties and Calorimetry Results

It is well established that fibers and other reinforcements in composites may act as nucleating sites and thus affect the crystallization kinetics of polymeric matrix resins [22]. Thermal properties of PHBV nanocomposites, including crystallization and melting behaviors, were investigated using DSC. Because PHBV has poor thermal stability and undergoes thermal degradation which can lead to a reduction in molecular weight [23,24], two heating and two cooling cycles were performed so that useful comparisons could be made. The numerical values of temperatures obtained from the first and second heating cycles are plotted in Figure 4.4, with the cooling runs shown in Figure 4.5. The corresponding thermal data are listed in Table 4.2. The data obtained from the first heating cycle include the effect of the prior thermal history of the injection-molded samples which underwent rapid cooling during the molding process, thereby impairing the crystallization process of the samples [25]. Upon slow cooling, the second heating cycle had a higher degree of crystallinity than the first heating cycle. There were two competing effects between nucleation and degradation of NFC on PHBV, as described below.

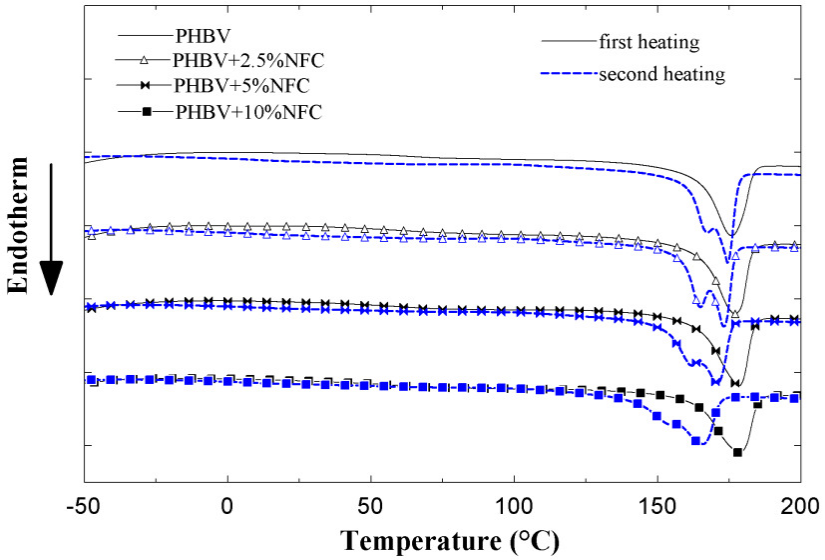

Figure 4.4 Comparison of melting endotherms during the first (solid line) and second (dashed line) heating scans of PHBV and its nanocomposites with NFC.

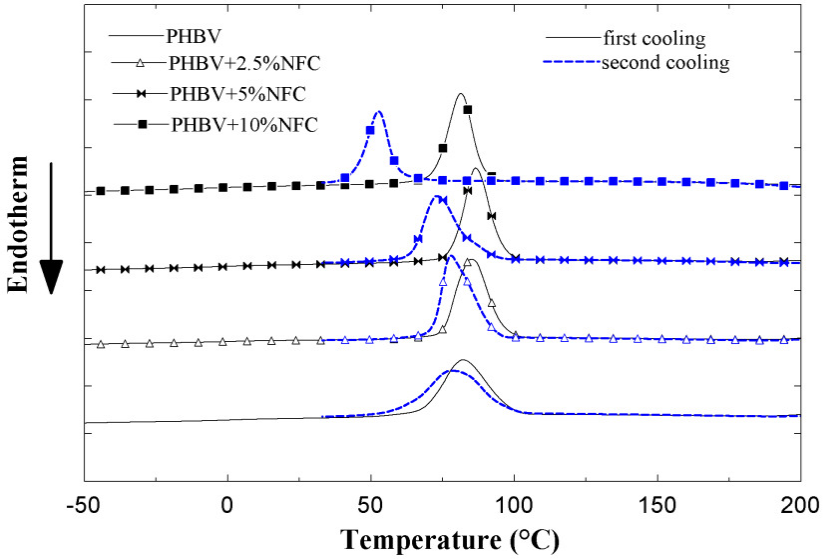

Figure 4.5 Comparison of crystallization exotherms during the first (solid line) and second (dashed line) cooling scans of PHBV and its nanocomposites with NFC.

Table 4.2 Thermal characteristics of PHBV/NFC nanocomposites.

Specimens	Heating			Cooling
	Melting		Degree of Crystallinity	Crystallization Temperature (°C)
	Temperature (°C)	Enthalpy (J/g)	χ_c (%)	
First heating and first cooling				
PHBV	175.80	79.96	73.35	81.78
PHBV + 2.5% NFC	176.91	79.54	74.84	84.87
PHBV + 5% NFC	178.13	77.95	75.27	86.41
PHBV + 10% NFC	178.46	74.59	76.40	81.85
Second heating and second cooling				
PHBV	167.37 174.35	96.74	88.75	77.11
PHBV + 2.5% NFC	164.92 173.03	94.70	89.10	77.81
PHBV + 5% NFC	161.94 170.75	88.55	85.51	72.85
PHBV + 10% NFC	165.55	78.22	79.73	52.55

Nucleating Effect

Table 4.2 and Figure 4.6 provide clear evidence that NFC served as a nucleating agent. As shown in Table 4.2, the crystallization temperature (T_c) during the first cooling cycle was higher with the addition of NFC. With the addition of 2.5, 5%, and 10% NFC, the crystallization peak of PHBV was roughly 3°C, 5 °C, and 0.1 °C higher, respectively. The initial increase and then decrease of crystallization temperatures with increasing NFC content could be the result of two competing factors; namely, enhanced nucleation of crystallization and material degradation

due to residual moisture or some other components such as the hydroxyl group in the NFC. The degree of crystallinity of PHBV slightly increased in the first heating cycle but decreased in the second heating cycle with the addition of NFC (Table 4.2). This increase in crystallinity was possibly due to the nucleating effect of the nanosized NFC fibers. Similar effects by other nanosized materials on crystallization and degradation have been reported previously [6,27].

Figure 4.6 shows the POM photographs of PHBV and PHBV/NFC nanocomposites. For neat PHBV, the number of spherulites was few and their size was relatively large because there was ample space for them to grow before impinging upon one another. For PHBV/NFC nano-composites, the shape of the spherulites was distorted. Furthermore, their size decreased and the number of PHBV spherulites increased significantly (Figure 6(b)-(d)). These results confirmed the nucleating effect of NFC. Similar results were reported for PHBV with cellulose nanowhiskers [28] and nanoclay [29].

Degradation

As shown in Figure 4.4, the endothermic peak, which occurred between 160 ºC and 180 ºC, is referred to as the melting peak of PHBV. An exothermic peak, which occurred between 50 and 100 ºC, was observed in all specimens and corresponded to the crystallization of PHBV (cf. Figure 4.5). In the DSC test, additional thermal scanning cycles caused a decrease in the melting (Figure 4.4) and crystallization (Figure 4.5) temperatures as well as both the melting and crystallization heat suggesting sample degradation. The effect of wood on the thermal degradation of PHBV has been reported [30,31]. The magnitude of the shift increased with increasing NFC concentration, indicating that NFC might cause degradation of the polymer, likely through residual moisture in the NFC, or through some other component in the NFC, or

via the degradation effect of hydroxyl groups on the cellulose from NFC [30,31]. An additional step of drying the NFC masterbatch in an oven at 90 °C for 5 h was found to be ineffective in removing the residual moisture. Further study is needed to remove moisture from the NFC.

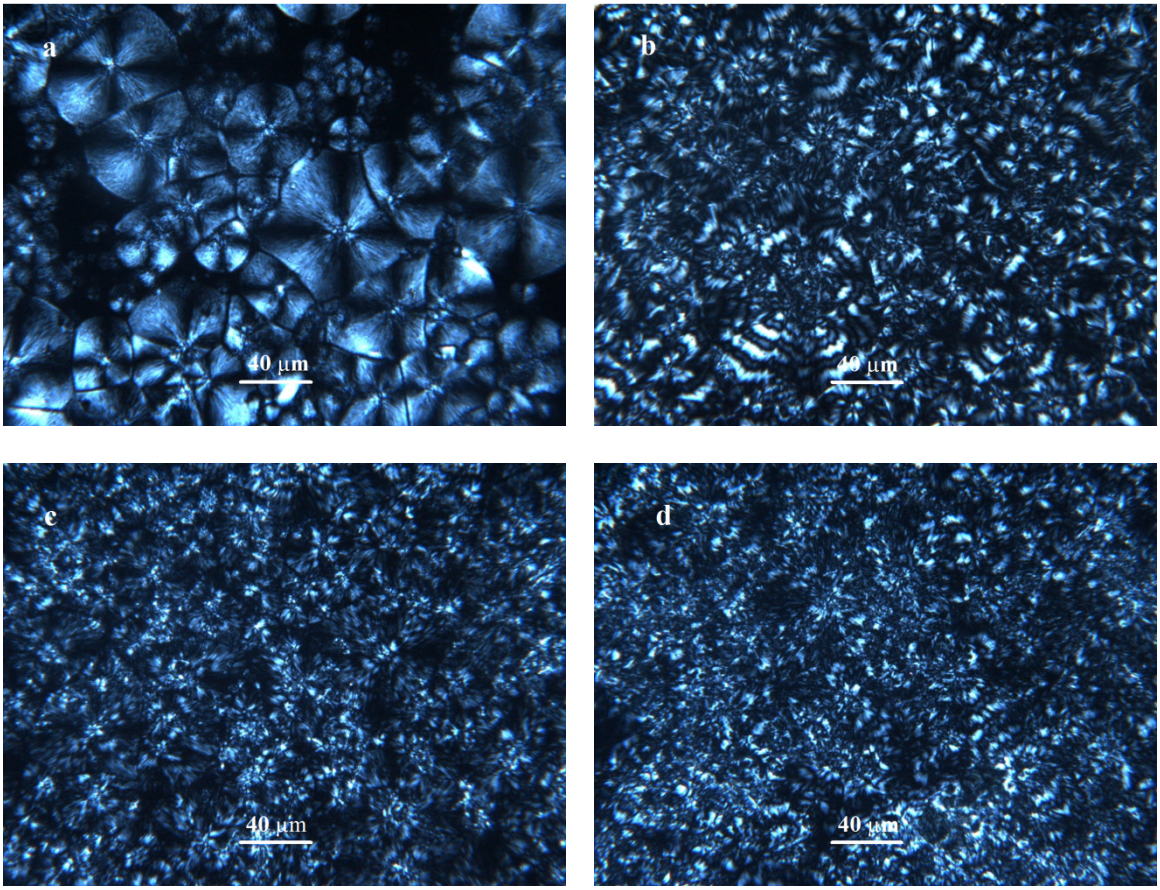

Figure 4.6 Polarized optical microscope photographs of PHBV/NFC nanocomposites: (a) PHBV, (b) PHBV + 2.5% NFC, (c) PHBV + 5% NFC, and (d) PHBV + 10% NFC.

4.3.4 Thermal Stability

The thermal stability of the neat PHBV and PHBV/NFC nanocomposite samples were examined using TGA. TGA results shown in Figure 4.7 confirm that adding NFC leads to

increased degradation. The onset degradation temperature of the PHBV/NFC nanocomposites decreased with the addition of NFC.

For dried NFC, there was an initial and slow weight loss of NFC until around 200 ºC, which might be attributed to both the loss of residual moisture in the NFC as well as the slow degradation of NFC. The most pronounced degradation began at approximately 200 ºC, which was lower than the maximum temperature of 210 ºC used in the heating scans during the DSC analysis. This supports the finding that the material might have degraded at the end of the first DSC heating scan (cf. Figure 4.4). There was an approximate 30% char yield at temperatures above 500 ºC.

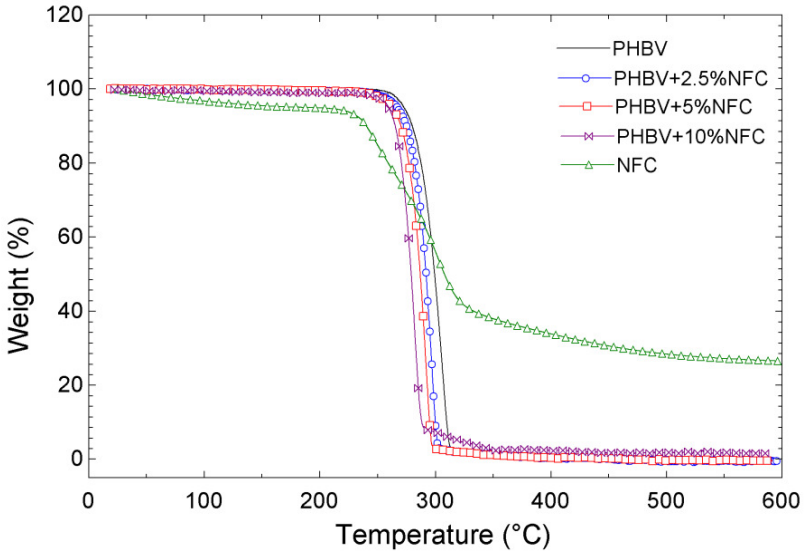

Figure 4.7 TGA curves for the PHBV/NFC nanocomposite samples.

4.3.5 Molecular Weight Measurement

The M_w and PDI values of the neat PHBV and PHBV/NFC nanocomposites were examined using GPC. GPC results shown in Figure 4.8 and Table 4.3 confirm that adding NFC leads to increased degradation. It is likely that there was a small amount of residual moisture and

some hydroxyl group in the NFC that triggered the PHBV molecular degradation through hydrolysis at high processing temperatures [6,30,32]. Furthermore, as can be observed, the M_w of the PHBV powder decreased 21% from 330,000 to 260,000 after the mixing and injection molding processes, indicating that the PHBV was prone to thermal degradation during processing [33,34].

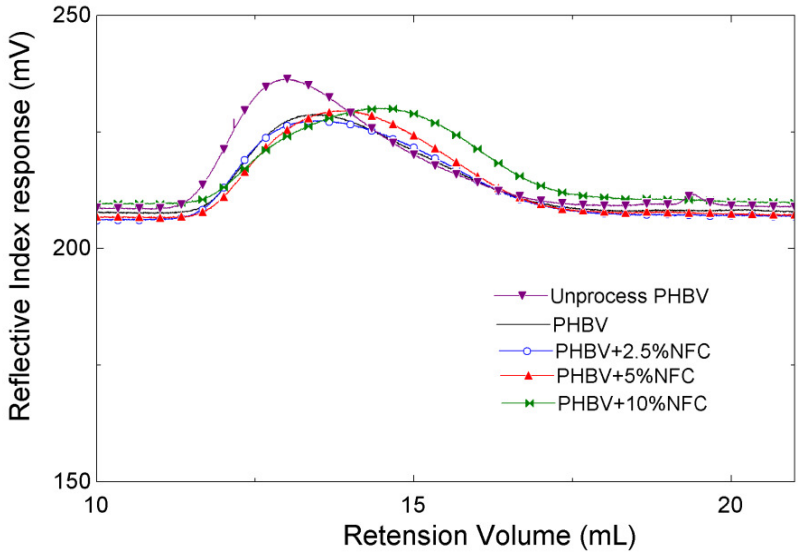

Figure 4.8 GPC chromatograms of PHBV/NFC nanocomposite samples.

Table 4.3 The M_w and PDI of the PHBV powder as received and the four specimens subjected to the mixing and injection molding process.

Samples	Mw	PDI
Unprocessed PHBV	330,000 ± 20,000	2.4
PHBV	260,000 ± 10,000	2.3
PHBV + 2.5% NFC	255,000 ± 10,000	3.4
PHBV + 5% NFC	230,000 ± 9,500	3.6
PHBV + 10% NFC	195,000 ± 8,000	4.4

4.3.6 Dynamic Mechanical Properties (DMA)

The viscoelastic properties of the PHBV and PHBV/NFC nanocomposites were studied using DMA. The resulting storage moduli and glass transition temperatures in terms of tan-δ of all of the specimens are shown in Figure 4.9 and 4.10, respectively. Below the T_g of the polymer matrix, there was a small increase in modulus, but more significantly, there was a large increase in the modulus above the glass transition temperature of the matrix with the addition of NFC. For example, the modulus for 10 wt% NFC reinforced nanocomposite increased 28% compared to neat PHBV at 25 ºC, while the storage modulus increased 137% at a temperature at 100 ºC. Similar results have been reported in other studies which have attributed this to the formation of a percolated system of cellulose held together by hydrogen bonding [35-37].

The glass transition temperature (T_g), which can be obtained from the peaks of the tan-δ curves in Figure 4.10, increased with increasing NFC. It was also found that the magnitude of the relaxation process strongly decreased with increasing NFC content and a slight shift of the peak position was observed upon the addition of NFC, which can be attributed to the limitation of chain mobility within the polymer matrix [6,38].

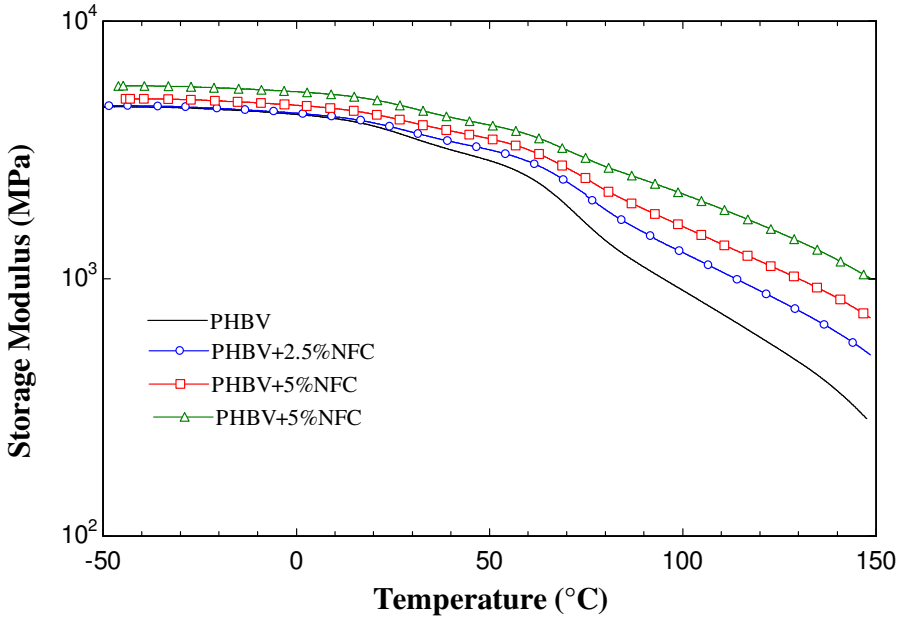

Figure 4.9 Storage moduli of the PHBV and PHBV/NFC nanocomposites as a function of temperature.

.

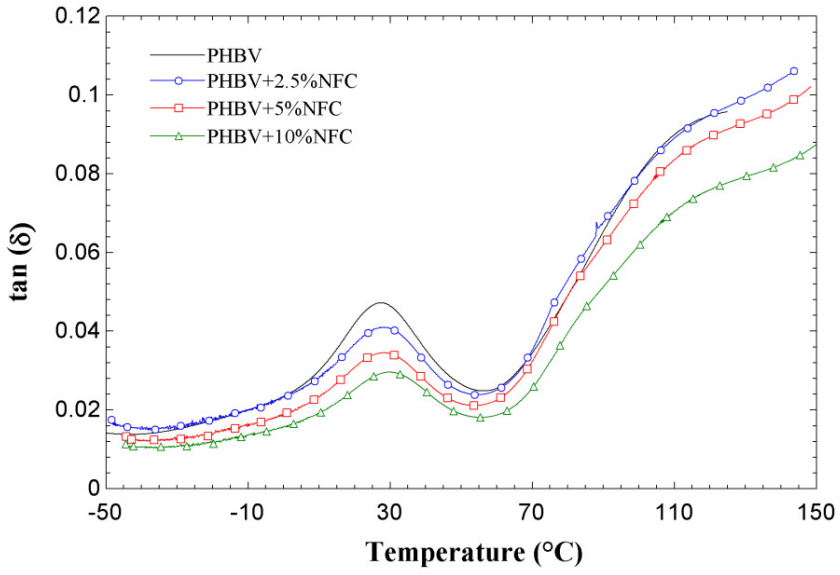

Figure 4.10 Tan δ curves of the PHBV and PHBV/NFC nanocomposites.

4.3.7 Sorption Behavior of CO_2 in PHBV/NFC Nanocomposites

It is known that the foamability of polymers is affected by the sorption of gas in the polymer and that the mechanisms of cell nucleation and cell growth are influenced by the amount of the gas dissolved in the polymer and the rate of gas diffusion [39]. Injection molded PHBV and PHBV/NFC nanocomposite specimens were originally weighed and then placed in a pressure vessel filled with CO_2. After depressurization, they were again placed on the scale to determine the amount of CO_2 absorbed. The weight gain was defined as the ratio between the mass of CO_2 in the sample and the original mass of PHBV. The mass loss described the mass of CO_2 present in the specimen as a function of time after the pressure release. A separate sorption test on NFC fibers alone revealed that the solubility of CO_2 in NFC fibers was negligible. Hence, the absorption and desorption results shown below were adjusted by the weight fraction of PHBV in the nanocomposites.

Figure 4.11 shows the absorption curves where the weight gain is plotted as a function of the square root of time. Regarding NFC content, the weight gain increased as the specimen thickness decreased. Equilibrium was reached after 50 h of exposure for 3.2 mm thick specimens, and only 16 h for 1.2 mm thick specimens. Nevertheless, the relationship between weight gain and $t^{1/2}$ was initially linear as described in Eqn. 4.2. The sorption amount increased with time of exposure until an equilibrium was reached.

At the same sample thickness, the absorption rate and maximum absorption degree was slightly lower as NFC was added. The maximum sorption degree was plotted as a function of NFC content (Figure 4.12). The measured solubility of gas decreased with the addition of NFC in the polymer matrix, perhaps because of the high crystallinity of the fiber as well as a higher

degree of crystallinity of PHBV acting as a CO_2 barrier, as suggested by Matuana and Park et al. [12,19,40]. The results obtained are presented in Table 4.4 and summarize the maximum absorption degree and absorption coefficients estimated from the curve in Figure 4.11 and Eq. (4.2) for the different experiments performed.

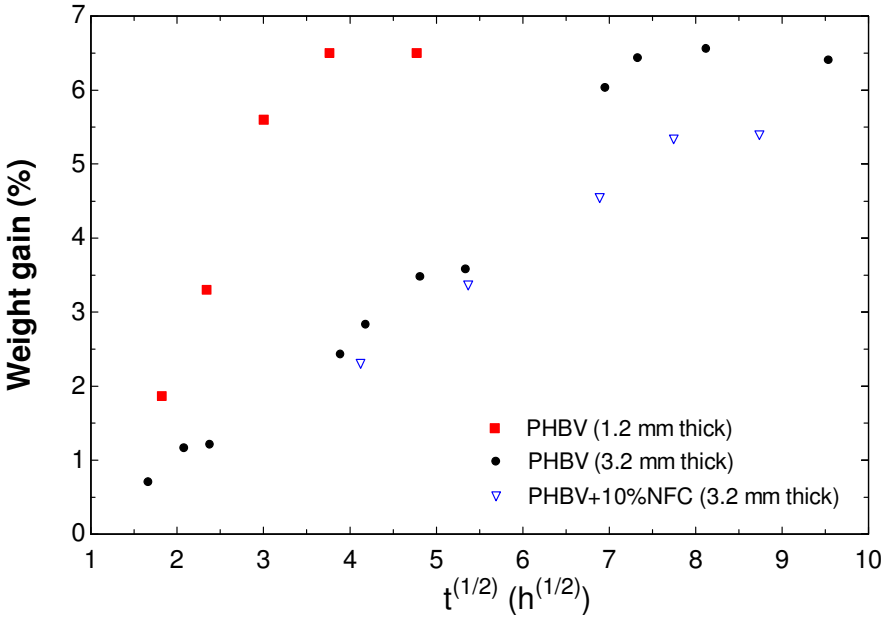

Figure 4.11 Absorption curves for CO_2 in PHBV and PHBV/NFC nanocomposites.

Similar to the absorption behavior, the rate of weight loss increased as sample thickness decreased. However, to compare the influence of NFC on the desorption behavior, 1.2mm thick injection molded specimens were used. The desorption curves for CO_2 in neat PHBV and PHBV/NFC nanocomposite specimens around one to two hours are illustrated in Figure 4.13. The fractional mass loss of CO_2 was approximated by a linear relationship with $t^{1/2}$ and the slope became steeper as the NFC content increased. Hence, the desorption diffusivity also increased as the amount of NFC increased. The increase in desorption diffusivity with an increasing fiber

content might be due to the lower molecular weight (as a result of degradation) in the NFC nanocomposite as well as the interface between fibers and matrix that provide a channel through which gas can quickly escape from the composites as reported in [12,39].

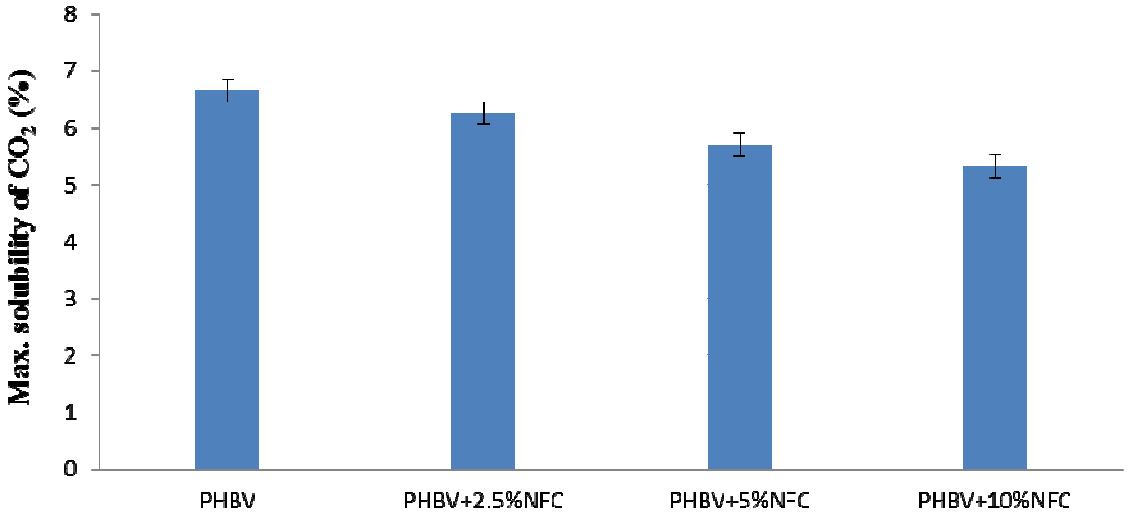

Figure 4.12 Maximum solubility of CO_2 in PHBV and their nanocomposites with 2.5, 5, and 10 wt% NFC.

Table 4.4 Comparison of maximum sorption degree and desorption and sorption coefficients for the different NFC contents.

	PHBV Maximum Sorption Degree (%)	**PHBV Desorption Diffusion Coefficient (cm^2/s)**	**PHBV Sorption Diffusion Coefficient (cm^2/s)**
PHBV	6.66	1.15×10^{-7}	6.44×10^{-8}
PHBV + 2.5% NFC	6.26	1.26×10^{-7}	6.06×10^{-8}
PHBV + 5% NFC	5.70	1.54×10^{-7}	5.12×10^{-8}
PHBV + 10% NFC	5.33	2.72×10^{-7}	4.88×10^{-8}

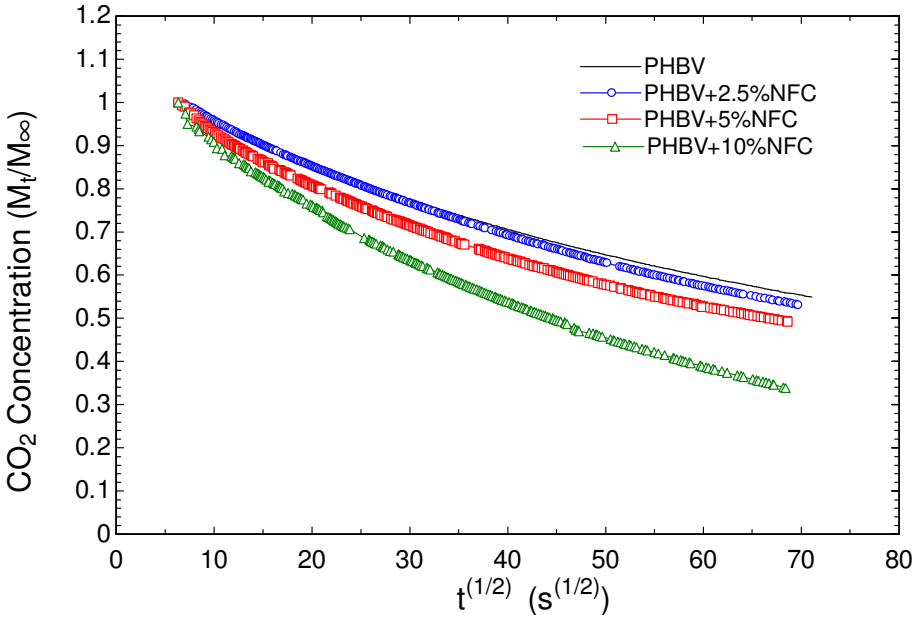

Figure 4.13 Desorption curves for CO_2 in PHBV and PHBV/NFC nanocomposites.

Moreover, as shown in Table 4.4, the experiments led to higher values for the desorption diffusion coefficient than for the sorption diffusion coefficient. It was suggested that the plasticizing effect of CO_2 was responsible for this tendency[11]. Even though sorption took place under higher pressure conditions and desorption proceeded at ambient temperature and pressure, the release of CO_2 from the polymer matrix during desorption was faster due to the higher chain mobility of the polymer substrate, which had been exposed to high pressure and temperature.

4.3.8 Foamed PVOH/NFC Nanocomposites

To investigate their foaming behavior, CO_2-saturated specimens were placed in a hot oil bath at various temperatures for 1 min after removal from the CO_2 pressure vessel. Since thinner specimens had less temperature variations within the specimen, specimens 1.2 mm thick were

used to study the effect of NFC on foaming behavior. When the polymer/gas solution was heated in the hot oil bath, the stiffness of the polymer matrix decreased, the gas diffusion rate increased, and the cells began to grow. The volume of the foaming specimens increased as the cells continued to grow, as driven by the gas molecules diffusing into the nucleated cells from the polymer matrix [19].

No foam structure (hence no cells) was seen at a hot oil bath temperature below 140 ºC. Cellular morphology developed in nanocomposites that foamed at a hot oil bath temperature of 155 and 175 ºC, as illustrated in Figure4.14 and 4.15, respectively. At the end of foaming, the foamed samples were frozen in liquid nitrogen and then quickly fractured. As shown in the figures, increasing the foaming temperature resulted in a significant increase in cell size. Higher temperatures accelerated the rate of gas diffusion and softened the polymer, which favored cell growth [19]. However, the void fraction decreased when NFC was added to the polymer matrix because the addition of NFC decreased the solubility of CO_2, accelerated the gas loss during foaming (cf. Figure 4.13), increased PHBV strength at high temperature (cf. Figure 4.9), and increased the degree of crystallinity (cf. Table 4.2) as suggested by Park et. al [12]. Therefore, development of foam structures and a high porosity were affected by adding the NFC. Similar results have been reported in several other studies on wood fiber-filled polymers [39,41]. More studies are needed to more precisely quantify the effect of NFC on the foaming behavior of PHBV.

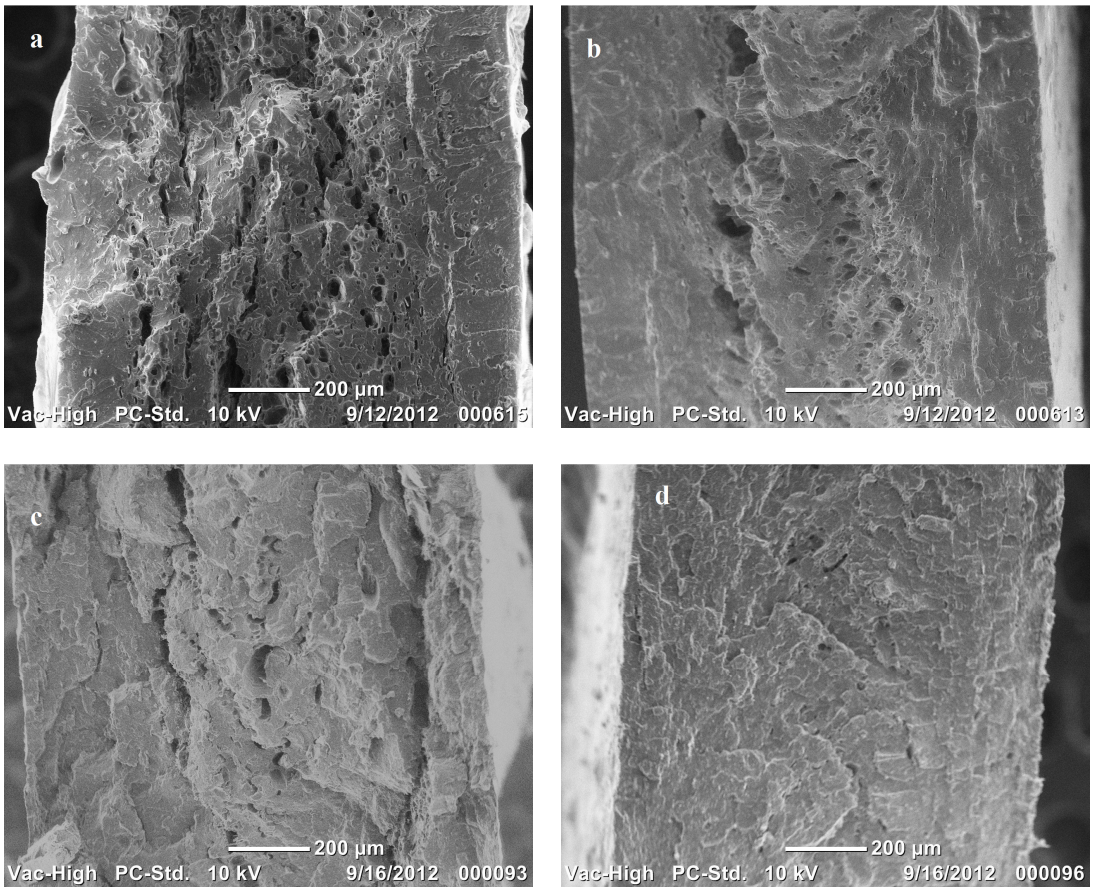

Figure 4.14 SEM images of foamed PHBV and PHBV/NFC nanocomposites at 155 ºC for 1 min: (a) PHBV, (b) PHBV + 2.5% NFC, (c) PHBV + 5% NFC, and (d) PHBV + 10% NFC.

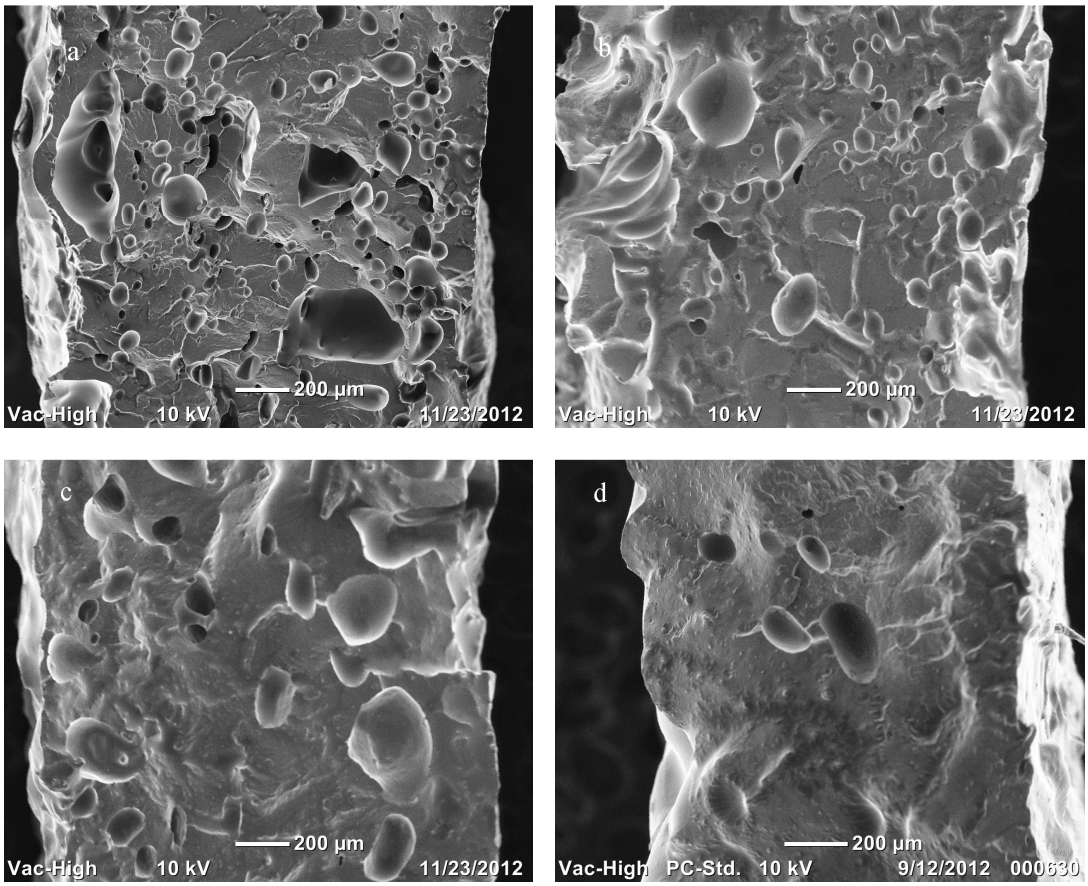

Figure 4.15 SEM images of foamed PHBV and PHBV/NFC nanocomposites at 175 ºC for 1 min: (a) PHBV, (b) PHBV + 2.5% NFC, (c) PHBV + 5% NFC, and (d) PHBV + 10% NFC.

4.4 Conclusions

Cellulose nanocomposite processing via a masterbatch with a high content of NFC in PHBV—a process which is scalable from the laboratory to an industrial setting—was attempted. The NFC and PHBV powders were premixed, freeze dried, and melt compounded to obtain nanocomposites with different fiber compositions. NFC increased the modulus of PHBV, as observed via both DMA and tensile tests. However, toughness decreased as the amount of NFC increased. The addition of NFC to PHBV was shown to increase the crystallization and glass

transition temperatures, but also caused the thermal degradation of PHBV, likely due to residual moisture or other components such as the hydroxyl group in the NFC. The absorption degree of CO_2 in the nanocomposites decreased and the desorption diffusivity increased as more NFC was added. Finally, the addition of NFC inhibited the foaming ability due to less CO_2 sorption, fast CO_2 loss, and a higher degree of crystallinity.

4.5 References

1. Mohanty A, Misra M, Drzal L. Sustainable bio-composites from renewable resources: opportunities and challenges in the green materials world. Journal of Polymers and the Environment.10(1):19-26, 2002.

2. Javadi A, Srithep Y, Lee J, et al. Processing and characterization of solid and microcellular PHBV/PBAT blend and its RWF/nanoclay composites. Composites Part A: Applied Science and Manufacturing.41(8):982-990, 2010.

3. Ten E, Turtle J, Bahr D, Jiang L, Wolcott M. Thermal and mechanical properties of poly (3-hydroxybutyrate-< i> co</i>-3-hydroxyvalerate)/cellulose nanowhiskers composites. Polymer.51(12):2652-2660, 2010.

4. Reinsch VE, Kelley SS. Crystallization of poly (hydroxybutrate co hydroxyvalerate) in wood fiber reinforced composites. Journal of Applied Polymer Science.64(9):1785-1796, 1998.

5. Doi Y, Tamaki A, Kunioka M, Soga K. Production of copolyesters of 3-hydroxybutyrate and 3-hydroxyvalerate by Alcaligenes eutrophus from butyric and pentanoic acids. Applied Microbiology and Biotechnology.28(4):330-334, 1988.

6. Srithep Y, Turng LS, Sabo R, Clemons C. Nanofibrillated cellulose (NFC) reinforced polyvinyl alcohol (PVOH) nanocomposites: properties, solubility of carbon dioxide, and foaming. Cellulose.1-15, 2012.

7. Siqueira G, Bras J, Dufresne A. Cellulosic bionanocomposites: A review of preparation, properties and applications. Polymers.2(4):728-765, 2010.

8. Dufresne A, Cavaille JY, Vignon MR. Mechanical behavior of sheets prepared from sugar beet cellulose microfibrils. Journal of Applied Polymer Science.64(6):1185-1194, 1997.

9. Jonoobi M, Harun J, Mathew AP, Oksman K. Mechanical properties of cellulose nanofiber (CNF) reinforced polylactic acid (PLA) prepared by twin screw extrusion. Composites Science and Technology.70(12):1742-1747, 2010.

10. Oksman K, Mathew A, Bondeson D, Kvien I. Manufacturing process of cellulose whiskers/polylactic acid nanocomposites. Composites Science and Technology.66(15):2776-2784, 2006.

11. Cravo C, Duarte ARC, Duarte CMM. Solubility of carbon dioxide in a natural biodegradable polymer: Determination of diffusion coefficients. The Journal of Supercritical Fluids.40(2):194-199, 2007.

12. Doroudiani S, Park CB, Kortschot MT. Effect of the crystallinity and morphology on the microcellular foam structure of semicrystalline polymers. Polymer Engineering & Science.36(21):2645-2662, 1996.

13. Cheung H, Ho M, Lau K, Cardona F, Hui D. Natural fibre-reinforced composites for bioengineering and environmental engineering applications. Composites Part B: Engineering.40(7):655-663, 2009.

14. Javadi A, Srithep Y, Pilla S, Lee J, Gong S, Turng LS. Processing and characterization of solid and microcellular PHBV/coir fiber composites. Materials Science and Engineering: C.30(5):749-757, 2010.

15. Saito T, Okita Y, Nge T, Sugiyama J, Isogai A. TEMPO-mediated oxidation of native cellulose: Microscopic analysis of fibrous fractions in the oxidized products. Carbohydrate Polymers.65(4):435-440, 2006.

16. Pääkkö M, Vapaavuori J, Silvennoinen R, et al. Long and entangled native cellulose I nanofibers allow flexible aerogels and hierarchically porous templates for functionalities. Soft Matter.4(12):2492-2499, 2008.

17. Standard test method for tensile properties of plastics. *ASTM D638-10*: ASTM International.

18. Matuana L. Solid state microcellular foamed poly (lactic acid): Morphology and property characterization. Bioresource Technology.99(9):3643-3650, 2008.

19. Matuana LM, Park CB, Balatinecz JJ. Processing and cell morphology relationships for microcellular foamed PVC/wood-fiber composites. Polymer Engineering & Science.37(7):1137-1147, 1997.

20. Vieth WR. Diffusion in and through Polymers: Principles and Applications: Hanser Munich; 1991.

21. Crank J. The mathematics of diffusion. 1979.

22. Baldwin DF, Park CB, Suh NP. A microcellular processing study of poly (ethylene terephthalate) in the amorphous and semicrystalline states. Part I: Microcell nucleation. Polymer Engineering & Science.36(11):1437-1445, 2004.

23. Quan H, Li ZM, Yang MB, Huang R. On transcrystallinity in semi-crystalline polymer composites. Composites Science and Technology.65(7):999-1021, 2005.

24. Pilla S. Handbook of Bioplastics and Biocomposites Engineering Applications. Vol 81: Wiley-Scrivener; 2011.

25. Avella M, Martuscelli E, Raimo M. Review Properties of blends and composites based on poly (3-hydroxy) butyrate (PHB) and poly (3-hydroxybutyrate-hydroxyvalerate)(PHBV) copolymers. Journal of Materials Science.35(3):523-545, 2000.

26. Srithep Y, Javadi A, Pilla S, et al. Processing and characterization of recycled poly (ethylene terephthalate) blends with chain extenders, thermoplastic elastomer, and/or poly (butylene adipate-co-terephthalate). Polymer Engineering & Science.51(6):1023-1032, 2011.

27. Probst O, Moore EM, Resasco DE, Grady BP. Nucleation of polyvinyl alcohol crystallization by single-walled carbon nanotubes. Polymer.45(13):4437-4443, 2004.

28. Ten E, Jiang L, Wolcott MP. Crystallization kinetics of poly (3-hydroxybutyrate-co-3-hydroxyvalerate)/cellulose nanowhiskers composites. Carbohydrate Polymers. 2012.

29. Wang S, Song C, Chen G, et al. Characteristics and biodegradation properties of poly (3-hydroxybutyrate- co-3-hydroxyvalerate)/organophilic montmorillonite (PHBV/OMMT) nanocomposite. Polymer Degradation and Stability.87(1):69-76, 2005.

30. Singh S, Mohanty A. Wood fiber reinforced bacterial bioplastic composites: Fabrication and performance evaluation. Composites Science and Technology.67(9):1753-1763, 2007.

31. Fernandes EG, Pietrini M, Chiellini E. Bio-based polymeric composites comprising wood flour as filler. Biomacromolecules.5(4):1200-1205, 2004.

32. Pilla S, Gong S, O'Neill E, Yang L, Rowell RM. Polylactide recycled wood fiber composites. Journal of Applied Polymer Science.111(1):37-47, 2008.

33. Smith R. Biodegradable polymers for industrial applications: CRC; 2005.

34. Lai M, Li J, Yang J, Liu J, Tong X, Cheng H. The morphology and thermal properties of multi-walled carbon nanotube and poly (hydroxybutyrate-co-hydroxyvalerate) composite. Polymer international.53(10):1479-1484, 2004.

35. Dubief D, Samain E, Dufresne A. Polysaccharide microcrystals reinforced amorphous poly (β-hydroxyoctanoate) nanocomposite materials. Macromolecules.32(18):5765-5771, 1999.

36. Favier V, Dendievel R, Canova G, Cavaille J, Gilormini P. Simulation and modeling of three-dimensional percolating structures: case of a latex matrix reinforced by a network of cellulose fibers. Acta Materialia.45(4):1557-1565, 1997.

37. Lu J, Wang T, Drzal LT. Preparation and properties of microfibrillated cellulose polyvinyl alcohol composite materials. Composites Part A: Applied Science and Manufacturing.39(5):738-746, 2008.

38. Srithep Y, Nealey P, Turng LS. Effects of annealing time and temperature on the crystallinity and heat resistance behavior of injection-molded poly (lactic acid). Polymer Engineering & Science. 2012.

39. Rachtanapun P, Selke S, Matuana L. Microcellular foam of polymer blends of HDPE/PP and their composites with wood fiber. Journal of Applied Polymer Science.88(12):2842-2850, 2003.

40. Matuana LM, Park CB, Balatinecz JJ. Cell morphology and property relationships of microcellular foamed pvc/wood fiber composites. Polymer Engineering & Science.38(11):1862-1872, 1998.

41. Matuana LM, Mengeloglu F. Microcellular foaming of impact-modified rigid PVC/wood-flour composites. Journal of Vinyl and Additive Technology.7(2):67-75, 2004.

CHAPTER 5

CONCLUSIONS AND FUTURE WORK

5.1 Conclusions

In this study, efforts have been made to advance the fundamental understanding and processing know-how of sustainable polymers and composites that could potentially reduce negative environmental impacts and broaden their application. Materials studied include post-consumer plastics as well as plastics and composites made from renewable resources.

In particular, Chapter 1 reports the effects of adding chain extenders (CE), thermoplastic elastomers (TPE), and poly(butylene adipate-co-terephthalate) (PBAT) on the properties of recycled poly(ethylene terephthalate) (RPET). The main objective of this study was to process and recycle non-biodegradable polymers with improved mechanical properties such as toughness and strain-at-break. The blends were produced using the injection molding process. The addition of CE, TPE, and toughening PBAT on the processability and material properties—including the mechanical and thermal properties of RPET—was discussed. By adding chain extenders, the molecular weight of RPET increased, as did its viscosity and mechanical properties. Even though adding TPE enhanced moldability, RPET and TPE were immiscible, thus any improvements in mechanical properties were limited.

Chapter 2 discusses the effect of annealing time and temperature on the crystallinity and heat resistance of poly(lactic acid) (PLA), a polymer made from renewable resources. The degree of crystallinity after long annealing times resembled those observed at higher temperatures, suggesting a time–temperature superposition relationship. Crystallinity isotherms in the logarithmic scale were shifted horizontally along the log–time axis, and a master curve was

constructed, which was found to follow the Williams–Landel–Ferry (WLF) and Arrhenius relationships. Moreover, improvements in the mechanical performance and heat resistance of PLA were achieved by increasing the overall crystallinity.

Chapters 3 and 4 discuss the effects of adding natural fiber, namely, nanofibrillated cellulose (NFC), on the properties of hydrophilic polymer polyvinyl alcohol (PVOH) and the hydrophobic polymer, poly (3-hydroxybutyrate-co-3-hydroxyvalerate, PHBV), respectively. The aim of this investigation was to process fully biodegradable nanocomposites and to study the effect of NFC on tensile and dynamic mechanical properties, crystallization behavior, degradation behavior, and the solubility of carbon dioxide (CO_2), as well as the foaming behavior of PVOH and PHBV. PVOH/NFC nanocomposite films were formed by a casting/evaporation technique. For PHBV, the NFC and the PHBV powders were premixed, freeze dried, and melt compounded. NFC had a reinforcing effect on both PVOH and PHBV. The addition of NFC to PHBV not only increased the crystallization and glass transition temperatures, but also caused thermal degradation, possibly due to residual moisture in the NFC. The absorption degree of CO_2 in the nanocomposites decreased and the desorption diffusivity increased as more NFC was added. Finally, the addition of NFC increased cell density and decreased cell size in the moisture-enabled foamed PVOH/NFC nanocomposites. However, NFC inhibited the foaming ability in PHBV due to less gas, gas loss, and a higher degree of crystallinity.

It is hoped that the aforementioned approaches will swiftly facilitate the recycling and reuse of polymers as well as promote an increased adoption of polymers and composites from renewable resources.

5.2 Future Work

It has been shown that some aggregation of the nanofibers taking place in the process of freeze drying might reduce strain-at-break and cause unsatisfactory tensile strength in PHBV/NFC nanocomposites. Therefore, it is necessary to modify the freeze-drying conditions and processes. It was suggested by Pääkkö et al. [1] that if the aqueous suspension of NFC is first quickly frozen using liquid propane (–180 ºC), the aggregation into 2D sheets is prohibited. This would provide better NFC dispersion in PHBV during melt compounding.

Since enhancement of the interfacial bonding between NFC and the hydrophobic polymer could improve both the mechanical performance and moisture resistance of natural fiber composites, further study could be done through the use of compatibilization techniques including fiber modifications such as silanation as well as matrix modifications using maleic anhydride (MA) graft copolymerization.

Finally, the present study employed only the batch foaming process. More efficient and effective foaming methods, such as continuous injection molding, have not been tried due to the small quantity of the NFC acquired. Microcellular injection molding, which uses supercritical fluid (SCF) such as nitrogen or carbon dioxide, could be used to mass produce less expensive nanocomposite components with excellent dimensional stability.

Reference

1. Pääkkö, M., et al., Long and entangled native cellulose I nanofibers allow flexible aerogels and hierarchically porous templates for functionalities. Soft Matter, 2008. 4(12): p. 2492-2499.